

A BAROTROPIC STABILITY STUDY OF FREE AND FORCED PLANETARY WAVES

BY

JOHN FYFE

A thesis submitted to the Faculty of Graduate Studies and Research in partial fulfilment of the requirements for the degree of Doctor of Philosophy.

Department of Meteorology

McGill University

Montréal, Canada

July 1987

© John Fyfe 1987

ABSTRACT

The stability of free and forced planetary waves in a β -channel is investigated with a barotropic model. The forced waves at equilibrium result from a constant mean-zonal wind interacting with a finite-amplitude topography.

The frequencies of all infinitesimal perturbations to the equilibrium flows are determined numerically as a function of the flow parameters. The results are interpreted using a truncated spectral model and related to those of previous studies with infinite β -planes. In contrast to some earlier analytical studies we find that unstable long waves ($L_x > L_y$) exist under superresonant conditions. We also report on the existence of an interesting travelling topographic instability.

The linear instability of a weakly non-zonal flow is investigated numerically and analytically (via WKB theory). The theory reproduces the qualitative nature of the numerically-determined fastest-growing mode.

Nonlinear integrations, involving many degrees of freedom, reveal that initially-infinitesimal disturbances may grow explosively to finite-amplitude. The longer-term integrations are interpreted using a statistical mechanical model.

RÉSUMÉ

La stabilité des ondes planétaires libres et forcées sur un canal β est étudiée avec un modèle barotrope. Les ondes forcées à l'équilibre résultent de l'interaction entre un vent zonal constant et une topographie ayant une amplitude finie.

Les fréquences de toutes les perturbations infinitésimales, des courants en équilibre sont déterminées numériquement en fonction des paramètres de l'écoulement. Les résultats sont interprétés en utilisant un modèle spectral tronqué et ceux-ci sont comparés aux études antérieures, faites dans un canal sur un plan bêta infini. Nous trouvons, par contraste, avec les études analytiques antérieures, que des ondes longues instables ($L_x > L_y$) existent, sous des conditions superrésonantes. Il est intéressant de constater également l'existence d'une instabilité topographique qui se propage dans l'espace.

L'instabilité linéaire d'un écoulement légèrement non-zonal est étudiée numériquement et analytiquement (par la théorie WKB). La théorie reproduit la nature qualitative du mode déterminé numériquement qui croît le plus rapidement.

Les intégrations non-linéaires, impliquant plusieurs degrés de liberté révèlent que les perturbations initiales infinitésimales peuvent croître explosivement à une amplitude finie. Les intégrations à long terme sont interprétées en utilisant un modèle mécanique statistique.

ACKNOWLEDGMENTS

First and foremost, I would like to thank Jacques Derome, my thesis supervisor, for his unfailing support throughout this work. His insightful criticisms and timely encouragements are most gratefully acknowledged. I would also like to acknowledge having the benefit of many useful discussions with Tom Warn and Theodore Shepherd. Further, I would like to express my gratitude to Herschel Mitchell who so kindly provided me with the original computer code and documentation for the nonlinear spectral model.

I would also like to thank Ursula Seidenfuss for her help with the diagrams. Finally, the financial support provided by The Natural Sciences and Engineering Research Council of Canada and the Atmospheric Environment Service of Canada is greatly appreciated.

TABLE OF CONTENTS

| | Page |
|---|------|
| Abstract | i |
| Résumé | ii |
| Acknowledgements | iii |
| Table of Contents | iv |
| List of Figures | vi |
| List of Tables | xii |
| Statement of Originality | xiii |
| | |
| CHAPTER 1 INTRODUCTION | 1 |
| | |
| CHAPTER 2 THE MODEL | 7 |
| 2.1 Basic formulation | 7 |
| 2.2 Steady flow | 8 |
| 2.3 Spectral equations | 11 |
| | |
| CHAPTER 3 LINEAR ANALYSIS | 14 |
| 3.1 Linear stability of free and forced two-dimensional waves | 14 |
| 3.1.1 An overview | 15 |
| 3.1.2 Perturbation equations | 17 |
| 3.1.3 Method of solution | 21 |
| 3.1.4 Parametric analysis | 23 |
| a. Zonal-wavenumber-1 basic wave | 23 |
| b. Zonal-wavenumber-2 basic wave | 37 |
| 3.1.5 Discussion | 43 |
| 3.2 Some effects of truncation on topographic instability | 46 |
| 3.2.1 Perturbation equations revisited | 47 |
| a. ψ' -equation | 48 |
| b. $\bar{\psi}$ -equation | 49 |
| c. ψ'^* -equation | 49 |
| 3.2.2 An analytical solution | 50 |
| 3.2.3 Numerical results | 52 |
| a. Instability close to linear resonance | 54 |
| b. Instability away from linear resonance | 56 |
| 3.2.4 Discussion | 61 |
| 3.3 Local instability of weakly non-parallel flow | 64 |
| 3.3.1 Topographic instability | 66 |
| 3.3.2 Fastest-growing perturbation | 68 |
| a. Structure and energetics | 69 |
| b. WKB analysis | 74 |
| 3.3.3 Discussion | 88 |

| | Page |
|--|------|
| CHAPTER 4 NONLINEAR ANALYSIS | 91 |
| 4.1 Some background | 91 |
| 4.2 Some preliminaries | 95 |
| 4.3 Numerical simulations | 98 |
| 4.3.1 Experiment 1: Initial weak instability | 99 |
| 4.3.2 Experiment 2: Initial strong instability | 110 |
| 4.3.3 Experiment 3: Localized topography | 116 |
| 4.4 Statistical mechanical equilibrium | 119 |
| 4.4.1 Methods of statistical mechanics: a brief review | 120 |
| 4.4.2 Numerical simulation: experiment 4 | 122 |
| 4.4.3 Approach to equilibrium of the numerical simulation | 124 |
| 4.5 Discussion | 126 |
| CHAPTER 5 SUMMARY AND CONCLUSIONS | 129 |
| APPENDIX A DETAILS OF THE DISPERSION RELATIONSHIP | 135 |
| APPENDIX B DECOUPLING OF THE STABILITY MATRIX | 136 |
| APPENDIX C TOPOGRAPHIC INSTABILITY: THE DISPERSION RELATIONSHIP | 137 |
| APPENDIX D DETAILS OF THE TWO AND THREE TERM SYSTEMS | 140 |
| APPENDIX E $\langle u \rangle$ IN THE NUMERICAL MODEL ($h = 0$) | 144 |
| APPENDIX F E AND Z IN THE NUMERICAL MODEL | 147 |
| APPENDIX G E AND Z IN THE STATISTICAL MECHANICAL MODEL | 149 |
| FIGURES | 150 |
| TABLES | 195 |
| BIBLIOGRAPHY | 198 |

LIST OF FIGURES

| Figure | | Page |
|--------|--|------|
| 1 | Super and subresonant flows. (a) Topography in meters: $\alpha = (1,1)$, $2h_\alpha/H = 0.03$; (b) superresonant flow: $u_s = 25$ m/s; (c) subresonant flow: $u_s = 23$ m/s. | 150 |
| 2 | Contours of e-folding time in days for the fastest-growing perturbations to zonal-wavenumber-1 flows. (a) Regions I and II(a); (b) region II(b). | 151 |
| 3 | Unstable superresonant zonal-wavenumber-1 flow (region I). (a) Basic flow: $u_s = 25$ m/s, $2h_\alpha/H = 0.02$; (b) growing perturbation: $\omega = 0.02i$ day ⁻¹ . | 152 |
| 4 | Reynolds stress (dot), form drag (triangle), and total zonal momentum tendency (plus) for the case of Figure 3. | 153 |
| 5 | Unstable subresonant zonal-wavenumber-1 flow [region II(a)]. (a) Basic flow: $u_s = 18$ m/s, $2h_\alpha/H = 0.1$; (b) growing perturbation: $\omega = 0.1i$ day ⁻¹ ; (c) damping perturbation: $\omega = -0.1i$ day ⁻¹ . | 154 |
| 6 | As in Figure 4 but for the case of Figure 5. | 155 |
| 7 | Unstable subresonant zonal-wavenumber-1 flow [region II(b)]. (a) Basic flow: $u_s = 12.5$ m/s, $2h_\alpha/H = 0.2$; (b) growing mode at $t = 0$: $\omega = -0.18 + 0.09i$ day ⁻¹ ; (c) as in (b) but at $t = 9$ days. | 156 |
| 8 | As in Figure 4 but for the case of Figure 7 ($\alpha = 0$). | 157 |

| Figure | | Page |
|--------|--|------|
| 9 | Subresonant zonal-wavenumber-1 topographic instability. (a) Basic flow: $u_s = 16.3$ m/s, $2h_\alpha/H = 0.1$; (b) growing perturbation at $t = 7T/8 \approx 25.8$ days: $\omega = -0.21 + 0.009i$ day ⁻¹ . | 158 |
| 10 | As in Figure 4 but for the case of Figure 9 at various times. The period T of the oscillation is 29.5 days. | 159 |
| 11 | As in Figure 2 but for the severe truncation. | 160 |
| 12 | Unstable zonal-wavenumber-2 free Rossby wave flow. (a) Basic flow: $U = 20$ m/s; (b) growing mode at $t = 0$: $\omega = -0.10 + 0.06i$ day ⁻¹ ; (c) as in (b) but at $t = 16$ days. | 161 |
| 13 | As in Figure 2 but for zonal-wavenumber-2 flows. | 162 |
| 14 | Unstable zonal-wavenumber-2 flow (resonant interaction). (a) Basic flow: $u_s = 15.4$ m/s, $2h_\alpha/H = 0.001$; (b) growing mode ($t = 0$): $\omega = -0.17 + 0.003i$ day ⁻¹ ; (c) as in (b) but at $t = 9$ days. | 163 |
| 15 | Unstable subresonant zonal-wavenumber-2 flow (shear instability). (a) Basic flow: $u_s = 15.4$ m/s, $2h_\alpha/H = 0.05$; (b) growing mode ($t = 0$): $\omega = -0.18 + 0.11i$ day ⁻¹ ; (c) 40-day Hovmöller diagram at $y = D/2$. | 164 |
| 16 | e-folding curves for various eddy truncations, NW . (a) $NZ = 41$ (dashed curve corresponds to $TR = [1,1]$); (b) $NZ = 9$ (dashed curve corresponds to $TR = [9,9]$ with 9 zonal wavenumbers). $2h_\alpha/H = 0.2$. | 165 |
| 17 | Contours of e-folding time in days. (a) $TR = [41,41]$; (b) $TR = [3,3]$ (dashed curve was obtained analytically). | 166 |

| Figure | | Page |
|--------|--|------|
| 18 | Subresonant travelling instability. Basic flow: $u_s = 11.0$ m/s, $2h_\alpha/H = 0.2$; perturbation: $\omega \approx -0.4 + 0.04i$ day ⁻¹ . Reynolds stress (dot), form drag (triangle) and \bar{u}' (plus). $T \approx 16$ days. | 167 |
| 19 | Subresonant travelling instability; high resolution. Basic flow: $u_s = 13.0$ m/s, $2h_\alpha/H = 0.2$; perturbation: $\omega \approx -0.3 + 0.02i$ day ⁻¹ . $T \approx 20$ days. | 168 |
| 20 | Contours of nondimensional growth rate for the topographic mode. Dashed line is the severe truncation neutral curve. | 169 |
| 21 | Topographic instability ($TR = [10, 10]$). (a) Basic flow: $u_s = 13$ m/s, $h_o = 1$ km; (b) slowest-growing perturbation: $\hat{\omega}_i \approx 2.33$, $\hat{\omega}_r = 0$. | 170 |
| 22 | Non-topographic instability ($TR = [10, 10]$). (a) Basic flow: $u_s = 17$ m/s, $h_o = 1$ km; (b) basic flow zonal component, \bar{u} (in units of m s ⁻¹); (c) fastest-growing perturbation: $\hat{\omega}_i \approx 3.6t$, $\hat{\omega}_r = 0$. | 171 |
| 23 | Zonal and meridional energy spectra, $E'(m)$ and $E'(\eta)$, respectively, corresponding to the mode in Figure 22c. | 172 |
| 24 | Fastest-growing mode to basic flow of Figure 22a when $TR = [5, 3]$. Structure at $t = 0$. $\hat{\omega}_i \approx 2.78$, $\hat{\omega}_r \approx 0.82$. | 173 |
| 25 | Local energy contributions from the fastest-growing mode. (a) Local contribution to $Cx + Cy$ energy conversion. (b) Local contribution to Cxy energy conversion. | 174 |
| 26 | Stability curves obtained using the two-term system. (a) Most-unstable zonal wavenumber, $m_M = (2\pi\delta)^{-1} \cdot k_M$, and growth rate, $\hat{\omega}_i$; (b) phase speeds evaluated at m_M . | 175 |

27. As in Figure 26 but for the three-term system. 176
28. Mapping of $\omega(k)$ in the complex $m = (2\pi\delta)^{-1} \cdot k$ plane. 177
Full lines correspond to constant $\hat{\omega}_r$ lines. Dashed lines correspond to constant $\hat{\omega}_i$ lines.
29. Complex wavenumber, m , versus zonal flow, $u_W(X)$, for two 178
branches of the dispersion relationship. The two branches are denoted m^+ and m^- . Dashed line with circles, m_r^+ ; solid line with circles, m_i^+ ; dashed line with crosses, m_r^- ; solid line with crosses, m_i^- .
30. As in Figure 29 but for the two-term system. 179
31. Experiment 1: Steady flow and disturbance. 180
(CINT = contour interval)
- (a) Steady flow streamfunction (CINT = 0.1);
(b) FGLD structure at $t = 0$. (Amplitude is arbitrary in linear theory so the contours are left unlabeled.);
(c) positive contours of $-(u'^2 - v'^2)\partial_x \bar{u}$. (CINT = -0.15).
32. Experiment 1: Small scale structure in the FGLD. 181
- (a) Zonal and meridional energy spectra, $E'(m)$ and $E'(n)$, respectively;
(b) disturbance vorticity, $\Delta\Psi_r$, with the β and ϵ waves excluded.
33. Experiment 1 Energy terms. 182
- (a) Total and mean zonal energy, E and \bar{E} , respectively;
(b) basic wave and disturbance energy, E^b and E^d , respectively. (Note that the plot of E^b has been terminated early so that it would not obscure E^d) The dashed curve is the contribution to E^d from the β and ϵ waves alone
34. Experiment 1: Basic wave trajectory and the channel 183
averaged flow.
- (a) ψ^b for $0 \leq t \leq 240$ days (dots at every 40 days);
(b) $\langle u \rangle$ for $0 \leq t \leq 240$ days;
(c) ψ^b for $240 \leq t \leq 400$ days;
(d) $\langle u \rangle$ for $240 \leq t \leq 400$ days;

| Figure | | Page |
|--------|--|------|
| 35 | Experiment 1: Behaviour of the primary waves in the disturbance. | 184 |
| | (a) Amplitude of the primary waves and the basic wave: A_β , A_ϵ and A_α , respectively. ($\delta = 0.02$); | |
| | (b) phase of the β -wave: $\theta_\beta = \tan^{-1}(\psi_\beta/\psi_\beta)$; | |
| | (c) phase sum: $\Sigma\theta_a = \theta_\beta + \theta_\epsilon + \theta_\alpha$. | |
| 36 | Experiment 1 Streamfunction of the total flow, ψ , and the disturbance vorticity, ζ^d , at specified times | 185 |
| | (a) ψ ($t = 100$); (b) ψ ($t = 200$); (c) ψ ($t = 300$ days); | |
| | (d) ζ^d ($t = 100$); (e) ζ^d ($t = 200$); (f) ζ^d ($t = 300$ days). | |
| | [In (a), (b) and (c) CINT = 0.1; in (d) CINT = 0.2; in (e) and (f) CINT = 1.] | |
| 37 | Experiment 2 | 186 |
| | (a) Steady flow streamfunction (CINT = 0.2); | |
| | (b) FGLD structure at $t = 0$; | |
| | (c) total, E , and mean zonal energy, \bar{E} $\delta = \sqrt{0.02}$ | |
| 38 | Experiment 2 | 187 |
| | (a) Channel-averaged flow, $\langle u \rangle$. $\delta = \sqrt{0.02}$. The dashed line corresponds to the $\delta = 2\sqrt{0.02}$ simulation; | |
| | (b) basic wave trajectory. Dots at every 10 days. | |
| 39 | Experiment 2. ($\delta = \sqrt{0.02}$). | 188 |
| | (a) Total streamfunction, ψ , at $t = 25$ days (CINT = 0.2); | |
| | (b) mean zonal flow, $\bar{u}(y, t)$, at $t = 25$ days; | |
| | (c) total streamfunction, ψ , at $t = 60$ days (CINT = 0.2); | |
| | (d) mean zonal flow, $\bar{u}(y, t)$ at $t = 60$ days; | |
| | (e) energy spectra at $t = 60$ days. Basic wave excluded. | |
| 40 | Experiment 2. Total, Z , and mean zonal potential enstrophy, \bar{Z} . $\delta = 2\sqrt{0.02}$. | 189 |
| 41 | Behaviour of initial easterly and westerly zonal flow. | 190 |
| | (a) $\langle u \rangle$; (b) ψ^b . $u_s = \mp 16$ m/s in dimensional units. | |

- 42 Experiment 3: Localized topography. 191
- (a) Topography: $r = D/2$ and $h_0/H = 0.1$;
 - (b) steady flow eddy streamfunction;
 - (c) FGLD at $t = 0$ days. ()^{*} indicates that the mean zonal component has been removed.
- 43 Experiment 3: $\delta = 2\sqrt{0.02}$. 192
- (a) Total and mean zonal energy, E and \bar{E} , respectively;
 - (b) zonal wavenumber one, $E(m=1)$, and two energy, $E(m=2)$;
 - (c) eddy streamfunction and mean zonal flow: $t = 100$ days;
 - (d) eddy streamfunction and mean zonal flow: $t = 400$ days.
- In (c), $CINT = 0.15$ and in (d), $CINT = 0.05$.
- 44 Experiment 4: $\delta = 2\sqrt{0.02}$. 193
- (a) Total streamfunction at $t = 0$ days ($CINT = 0.2$),
 - (b) potential vorticity versus streamfunction at $t = 0$ days;
 - (c) $\langle u \rangle$; (d) ψ^b .
- 45 Simulation at $t = 100$ days versus statistical equilibrium. 194
- (a) Simulation streamfunction ($CINT = 0.1$);
 - (b) equilibrium streamfunction ($CINT = 0.1$);
 - (c) energy spectra for the simulation and the statistical equilibrium (the latter are shown as continuous curves).

LIST OF TABLES

| Table | | Page |
|-------|---|------|
| 1 | Growth rate of the topographic mode as a function of truncation: $M = N$ and NL is the total number of degrees of freedom. | 195 |
| 2 | Growth rate and frequency of the fastest-growing mode corresponding to Figure 22 as a function of truncation. | 195 |
| 3 | Experiments 1 and 2: Effect of resolution on e-folding time, τ , and period, T , for the fastest-growing linear disturbance. $M = N$, where M and N are the number of zonal and meridional wavenumbers, respectively. | 196 |
| 4 | Experiment 2. Simulation sensitivity to resolution, M , and timestep, Δt , at $t = 60$ days. $\delta = \sqrt{0.02}$. | 196 |
| 5 | Experiment 4: Simulation at $t = 100$ days versus statistical equilibrium. The values in parenthesis are for $t = 0$ days. Note that values for equilibrium at $\delta = \sqrt{0.02}$ are also provided. | 197 |

STATEMENT OF ORIGINALITY

The original work contained in this study includes:

- 1) a parametric analysis of the linear stability of free and forced barotropic waves where approximate analytic and accurate numerical solutions are obtained (see Section 3.1):
- 2) a demonstration of the dependence of topographic instability on the meridional structure of the perturbation and the discovery of a travelling topographic instability (see Section 3.2):
- 3) a study of the linear instability properties of a weakly non-zonal forced flow where the severe truncation assumption often made in such studies is relaxed and where the fastest-growing mode is analyzed using local instability theory (see Section 3.3).
- 4) an examination of the nonlinear instability properties of a number of equilibrium flows using a time-dependent spectral model which incorporates many degrees of freedom (see Chapter 4).

It should be known that the results of (1), (2) and (3) also appear, in a slightly modified form, in Fyfe and Derome 1986 (*J. Atmos. Sci.*, 43: 2162-2182), Fyfe and Derome 1987a (*Atmos. and Oceans*, 25: 159-176) and Fyfe and Derome 1987b (*Geophys. Astrophys. Fluid Dyn.*, in press), respectively. The second author in each of these publications

is the candidate's thesis advisor. With regards to the question of authorship responsibilities, the second author, besides giving ordinary thesis supervision and advice, provided: (i) subsection 3.1.1 and 3.1.5, which form the Introduction and Conclusion, respectively, of Fyfe and Derome (1986); (ii) Appendix B, which is Appendix A in Fyfe and Derome (1987a). In addition, in all of these works the second author, in an editorial capacity, ensured that the standard of English, and of the presentation of mathematics, figures and tables was sufficiently high for the purposes of publication.

CHAPTER 1

INTRODUCTION

One of the primary goals of dynamic meteorology is to explain the existence and variability of planetary scale waves in the atmosphere. These waves, which exist as large-scale deviations from the predominately westerly flow found in the mid-troposphere, can be seen quite clearly on daily weather maps. Moreover, due to the quasi-stationary and persistent nature of these motions they often also appear on time-averaged maps, where the atmosphere has been averaged for a period of, say, one month or more. Interestingly, the zonal asymmetries observed on mean monthly or seasonal maps tend to occur at approximately the same location year after year. Several plausible mechanisms have been invoked to explain this fact, including topographic forcing (Charney and Eliassen, 1949), local thermal forcing (Smagorinsky, 1953), or both (Derome and Wiin-Nielsen, 1971). Although the earth's orography and thermal effects resulting from the continents and the oceans are probably the major factors in the generation of planetary waves, the mechanisms involved are still not fully understood. In this study we will focus our attention on some of the theoretical aspects of flow over and around a large-scale topography.

Early theoretical attempts to explain the existence of planetary scale motions include Rossby's (1939) theory of free barotropic planetary waves and Charney and Eliassen's (1949) theory of waves forced by the diversion of a mean zonal flow by the earth's large-scale topography. Although these classical theories have been useful in interpreting the seasonal average of observed planetary scale motions

they are not generally applicable to transient shorter time scale phenomena, such as, atmospheric blocking in the troposphere and sudden warming in the stratosphere. Atmospheric blocking is a phenomenon wherein a large-scale quasi-stationary flow pattern is observed to amplify, occasionally to anomalously large amplitude, and to persist for up to several weeks. The drought in the United Kingdom which persisted from the spring of 1975 to the summer of 1976 and the severe winter experienced in the United States in 1977 both involved this sort of circulation. Sudden warming, on the other hand, is a stratospheric phenomenon, occurring during the winter in high latitude regions. During these events the mean temperature of the stratosphere is dramatically increased and the circumpolar jet stream destroyed or even reversed. It should be mentioned that tropospheric blocking and stratospheric sudden warming often occur simultaneously.

One way to study the variability (i.e., transient behaviour) of planetary waves is to undertake a linear stability analysis of one, or more, of the theoretically postulated wave types, e.g., free Rossby waves or topographically forced waves. In such a study the basic flow, which alone is steady (i.e., time-independent), is subjected to infinitesimal perturbations. If the perturbations grow without bound then the basic flow is deemed unstable; otherwise it is stable. Lorenz (1972), Gill (1974), Coaker (1977) and Meid (1978), for example, have studied the linear stability of a free Rossby wave. On the other hand, Charney and Devore (1979), Charney and Flierl (1981) and Vallis (1985) have studied the linear stability of a topographically forced wave. All of the above studies share the common assumption that the large-scale flow is barotropic (i.e., the density depends only on

pressure). This assumption is supported by observations which indicate that large-scale waves in the winter are nearly equivalent barotropic in structure (Blackmon et al., 1979; Wallace, 1983). Under this assumption any instability which is encountered derives its energy solely from the kinetic energy of the basic flow (assuming no external forcing or internal dissipation). In order to reduce our own study of the stability of free and forced waves to tractable proportions we will also assume barotropic flow.

After formulating the mathematical model in Chapter 2, in Section 3.1 we will present our own findings regarding the linear stability of free and topographically forced planetary waves. Besides presenting accurate growth rate curves (obtained using more degrees of freedom than has usually been the case) over a wide range of parameter values we will also employ suitably simplified models to help analyze the various instabilities encountered. This section appears, with only slight modifications, in Fyfe and Derome (1986). In addition, the main results have been presented at the Stanstead Seminar, July 1984, and appear in extended abstract form in Derome and Fyfe (1985).

In Section 3.2 we consider more closely one of the important instabilities obtained in the previous section, namely form drag instability (sometimes referred to as topographic instability). This instability mechanism was discovered by Charney and Devore (1979) and since then numerous researchers have used simplified models (i.e., low-order spectral truncations) in an attempt to describe its essential characteristics (e.g., Hart, 1979; Charney and Flierl, 1981; Pedlosky, 1981; Rambaldi et al., 1985). In our numerical study we will check the extent to which these earlier analytical studies correctly

treated form drag instability. The results of Section 3.2 appear in published form in Fyfe and Derome (1987a).

One of the more interesting features of the large-scale atmospheric flow is the presence of preferred geographical regions of development of transient cyclone disturbances. For instance, if one considers the observed wintertime circulation in the northern hemisphere two distinct maxima in the variance of all variables at all levels in the troposphere can be distinguished: one in the western Atlantic ocean and another in the western to central Pacific ocean (see Blackmon, 1976; Blackmon et al., 1977; Lau, 1978). To help understand how the large-scale planetary waves in the atmosphere determine the preferred regions of cyclogenesis (as well as the onset of blocking for that matter) a number of researchers have employed linear instability theory (e.g., Frederiksen, 1979a,b, 1980, 1982, 1983; and Niehaus, 1980, 1981). In these studies the linear stability of idealized wavy basic states was analyzed numerically, using either two-layer models or multi-level models. Although this approach has met with considerable success in predicting, say, the geographical distribution of synoptic scale eddy heat flux in the atmosphere there remained a number of theoretical questions regarding the stability calculations. A lengthy discussion regarding these matters can be found in Pierrehumbert (1984, hereafter referred to as PH).

In an attempt to address some of the questions regarding the connection between instability theory and regional cyclogenesis, PH invoked the concept of absolute instability (in the sense of Merkin, 1977). Within the framework of a two-layer β -plane model PH used this concept along with a WKB analysis to differentiate "local" unstable

modes from "global" unstable modes. Local modes have peak amplitude downstream of the point of maximum baroclinicity, decay to zero exponentially away from the peak and do not depend on zonal periodicity for their existence. Global modes, on the other hand, require periodic boundary conditions and have growth rates which depend on the average baroclinicity of the basic flow. It was argued by PH that the latter of these modes are nonphysical and as such should not, by themselves, be used as prototypes for regional cyclogenesis. More generally, it was suggested that the locally determined absolute growth rate is a useful diagnostic for assessing the instability properties of wavy basic flows.

In Section 3.3 of this study the local (linear) instability properties of topographically forced barotropic flow on a β -channel are investigated numerically using the spectral method and analytically via WKB theory. The WKB theory which is employed relies on some of the techniques developed by PH in connection with his baroclinic instability problem. By comparing the numerically-determined fastest-growing mode with that obtained theoretically we hope to delineate some of the factors governing the local growth of linear disturbances. The results of this study appear in Fyfe and Derome (1987b).

One of the shortcomings of linear instability theory is that it precludes investigation of the dynamics underlying interactions between the basic state, such as a topographically forced stationary wave, and the superimposed disturbance with respect to which it is unstable. In an observational study of this particular interaction, Holopainen (1978) has shown that the horizontal convergence of momentum flux, associated with the small and large scale eddies, is important to the stationary waves' long-time average vorticity balance. In an attempt to understand

the interaction between the standing waves and the transient eddies in the atmosphere we will study, in Chapter 4, the *nonlinear* evolution of finite-amplitude disturbances superimposed on stationary topographically forced waves. Unlike some previous theoretical investigations along these lines (i.e., Deininger, 1981; Nathan and Loesch, 1987) we will mostly use a *fully* nonlinear spectral model which employs *many* degrees of freedom. In addition, to help interpret the long-term behaviour of our numerical simulations we will use the methods of statistical mechanics.

The plan of the remainder of this thesis is as follows. In Chapter 2 we formulate the mathematical model while in Chapter 3 and Chapter 4 we present our linear and nonlinear results, respectively. Finally, in Chapter 5 we summarize our results and state our conclusions.

CHAPTER 2

THE MODEL

The model which we will use is probably the simplest one devisable which still retains the basic physical mechanisms responsible for the instability of free and topographically forced planetary waves. In Section 2.1 we will introduce the model, while in Section 2.2 we will derive, and then describe, a particular class of steady-state solutions to the model equation. It is the stability of these finite-amplitude steady-state flows which will mostly interest us in this study. In Section 2.3 we will formulate a set of truncated spectral equations which will enable us to examine certain aspects of the stability of planetary waves which cannot be studied analytically.

2.1 Basic formulation

For these investigations we will use the quasi-geostrophic barotropic vorticity equation which for inviscid flow on a midlatitude β -plane may be written

$$\partial_t \Delta \psi + J(\psi, Q) = 0, \quad Q = \Delta \psi + \beta y + f_0 h/H \quad (1)$$

where Δ and J are the Laplacian and Jacobian operators, respectively, ψ is the streamfunction, β the latitudinal derivative of the Coriolis parameter, f_0 a midlatitude value of the Coriolis parameter, H the mean depth of the barotropic atmosphere and h the topographic height. In what follows we take the domain to be periodic in the zonal direction (x) with a fundamental length, L . We also assume that the flow is confined to a β -plane channel bounded by rigid walls at $y = 0$ and $y = D$ implying that

$$v = \partial_x \psi = 0 \quad \text{at } y = 0 \quad \text{and } y = D. \quad (2)$$

Further to this it can be demonstrated by applying (2) that no mean circulation may develop on the walls if it does not exist at $t = 0$, i.e.

$$\partial_t \bar{u} = - \partial_t (\partial_y \bar{\psi}) = 0 \quad \text{at } y = 0 \quad \text{and } y = D, \quad (3)$$

where the overbar denotes a zonal average over the fundamental length L . As we will see these boundary conditions can represent rather strong constraints on the flow.

2.2 Steady flow

The steady solutions (denoted with a tilde) to (1) are very easily obtained by setting the time-derivative to zero and then noting that this implies \bar{Q} must be functionally related to $\bar{\psi}$, i.e. $\bar{Q} = G(\bar{\psi})$. However, in this inviscid setting this functional relationship is indeterminate and can only be rigorously determined by considering the inviscid limit of some appropriate viscous configuration. By way of avoiding the many technical difficulties associated with this approach we will do as many others have (e.g., Charney and Flierl, 1981; Vallis, 1985; Rambaldi et al., 1985; Mukougawa and Hirota, 1986a, b) and specify it, a priori, to be linear, i.e.

$$\bar{Q} = -K_s^2 \bar{\psi}, \quad (4)$$

where K_s is a constant. The right-hand side of (4) may be interpreted as the leading order term in the Taylor series expansion for $G(\bar{\psi})$. A further discussion on the subject of this simplifying assumption can be found in Derome (1984).

Equation (4) is a partial differential equation which is relatively easily solved once the parameters of the problem and topographic form is specified. In this study we will mostly consider a topography which can be described by a single Fourier component, i.e.,

$$h(x,y) = h_{\alpha} \cdot 2\sin(2\pi m_{\alpha} x/L) \sin(\pi n_{\alpha} y/D), \quad h_{\alpha} \geq 0. \quad (5)$$

Here α denotes the integer pair (m_{α}, n_{α}) where m_{α} and n_{α} are the zonal and meridional wavenumbers, respectively [the reason for the factor of 2 in (5) will become apparent shortly]. With this topography the steady flow streamfunction arising from (4) can be written as

$$\bar{\psi}(x,y) = -u_s \cdot y + \bar{\psi}_{\alpha} \cdot 2\sin(2\pi m_{\alpha} x/L) \sin(\pi n_{\alpha} y/D) \quad (6a)$$

$$\text{where } \bar{\psi}_{\alpha} = f_0 (h_{\alpha}/H) / (K_{\alpha}^2 - K_s^2), \quad (6b)$$

$$K_{\alpha}^2 = (2\pi m_{\alpha}/L)^2 + (\pi n_{\alpha}/D)^2, \quad \text{and} \quad K_s^2 = \beta/u_s. \quad (6c)$$

It should be noted that an addition to (6a) of a zonal shear component of the form $\bar{\psi} \cos(L_s y)$, where $\bar{\psi}$ is arbitrary, is permissible as long as $L_s = K_s$ (Derome, 1984).

If one interprets (6a) as representing a deviation, $\bar{\psi}^*$, from a basic mean-zonal flow, $-u_s \cdot y$, then it can easily be shown that $\bar{\psi}^*$ is a solution of the linearized version of (1) (where the linearization is about $-u_s \cdot y$). More significantly, it is also an exact finite-amplitude solution and for this reason alone should merit further study. Admittedly, the presence of a small amount of friction may modify this finite-amplitude solution, as discussed by Hart (1977). Notwithstanding this fact, we believe that the inviscid limit is a justifiable starting point.

To gain a physical understanding of (6) we follow Smith (1979) and, in Eq. (7a-c), consider three separate cases corresponding to when the denominator of $\tilde{\psi}_\alpha$ in (6b) is positive (i.e., superresonant), negative (subresonant) or zero (resonant)

$$(a) \quad K_\alpha^2 - K_s^2 > 0 \quad (7a)$$

Here the amplitude of the wave is positive and the streamlines are displaced northward over mountains ($h > 0$) and southward over valleys ($h < 0$). As the potential vorticity conserving particles approach the mountain, the increase in h must be compensated by a decrease in absolute vorticity, $\Delta\tilde{\psi} + \beta y$. In this superresonant flow the latter is effected by a relatively large decrease in $\Delta\tilde{\psi}$ as the particles move northward, increasing βy . Naturally the reverse argument can be presented for the flow over a valley. This type of flow is depicted in Fig. 1b, for the topography of Fig. 1a. In this and subsequent figures the basic flow plots are for the geopotential height in decameters, solid lines are positive contours and dashed lines are negative contours.

$$(b) \quad K_\alpha^2 - K_s^2 < 0 \quad (7b)$$

In this case the response is reversed with a southward displacement of the streamlines over mountains and a northward displacement over valleys (see Fig. 1c). Again the absolute vorticity is reduced (increased) over high (low) ground but as the flow has a very large scale and hence low relative vorticity, this is accomplished by a different mechanism involving southward (northward) flow into regions of

smaller (larger) planetary vorticity, βy . Flows of this variety, which are commonly referred to as subresonant, are characterized by a dominance of the planetary vorticity advection over that of relative vorticity.

$$(c) \quad K_{\alpha}^2 - K_S^2 = 0 \quad (7c)$$

Here the advection of relative and planetary vorticity cancel resulting in an infinite, or in other words *resonant*, response to the topographic forcing. This singularity is associated with the fact that there exists an unforced (or free) solution to (4) representing a standing Rossby wave whose westward directed phase speed exactly balances the eastward advection of relative vorticity by the mean zonal wind, u_S . In what follows we often consider flows for which (7c) is identically true and in these situations it should be understood that we are referring to the free Rossby wave solution (6a) for which $h_{\alpha} = 0$, $u_S = \beta/K_{\alpha}^2$ and $\tilde{\psi}_{\alpha}$ is arbitrary.

2.3 Spectral equations

As a first step towards solving the model equation, under general conditions, it will be necessary to spatially discretize our system. With this objective in mind we express the total streamfunction as the sum of a (time-independent) linear term and an infinite Fourier series, i.e.,

$$\psi(x, y, t) = u_S y + \sum_{\alpha} \psi_{\alpha}(t) F_{\alpha}(x, y) \quad (8)$$

where $F_\alpha(x,y)$ is a member of following orthonormal basis

$$\left\{ \begin{array}{l} \sqrt{2} \cos(\pi n_\alpha y/D), \quad 2 \sin(2\pi m_\alpha x/L) \sin(\pi n_\alpha y/D), \\ 2 \cos(2\pi m_\alpha x/L) \sin(\pi n_\alpha y/D) \end{array} \right\} \quad (9)$$

The subscript α corresponds to the pair of wavenumbers (m_α, n_α) connected with that basis function and a summation over α implies a summation over all modes. Note that the inclusion of the linear term in y in (8) will allow us to specify a constant zonal flow on the walls.

The set of basis functions (9) can be shown to satisfy the following conditions.

$$\partial_x F_\alpha = 0 \quad \text{at } y = 0 \quad \text{and } y = D, \quad (10a)$$

$$\langle F_\alpha F_\beta \rangle = \delta_{\alpha\beta} = \begin{cases} 1 & \text{if } \alpha = \beta \\ 0 & \text{if } \alpha \neq \beta \end{cases} \quad (10b)$$

where $\langle () \rangle$ denotes the horizontal average.

$$\langle () \rangle = \frac{1}{LD} \int_0^D \int_0^L () dx dy$$

and

$$\Delta F_\alpha = -K_\alpha^2 F_\alpha \quad (10c)$$

From here it can be readily seen that this choice of basis functions ensures that the boundary conditions (2) and (3) are satisfied for all time.

Substituting (8) into (1) and applying a Galerkin procedure leads to the following set of equations governing the behaviour of the set of real spectral coefficients, $(\psi_\alpha(t))$

$$\begin{aligned}
K_\alpha^2 \cdot \partial_t \psi_\alpha + \sum_{\beta \epsilon} \psi_\beta K_\epsilon^2 \psi_\epsilon c_{\beta \epsilon \alpha} + u_s \sum_{\beta} K_\beta^2 \psi_\beta b_{\beta \alpha} - \beta \sum_{\beta} \psi_\beta b_{\beta \alpha} \\
= u_s \sum_{\beta} (f_o h_\beta / H) b_{\beta \alpha} + \sum_{\beta \epsilon} \psi_\beta (f_o h_\epsilon / H) c_{\beta \epsilon \alpha}
\end{aligned}
\tag{11}$$

where $c_{\beta \epsilon \alpha} = \langle F_\beta^J(F_\epsilon, F_\alpha) \rangle$ and $b_{\beta \alpha} = \langle F_\beta \partial_x F_\alpha \rangle$

In (11), $c_{\beta \epsilon \alpha}$ and $b_{\beta \alpha}$ are the interaction coefficients, K_α is the two-dimensional wavenumber and (h_α) is the set of spectral coefficients corresponding to $h(x,y)$. The evaluation of $c_{\beta \epsilon \alpha}$ and $b_{\beta \alpha}$ is straightforward but cumbersome and is omitted here [the reader is referred to Appendix A of Mitchell (1982) for the details].

So far we have simply replaced the difficult, if not impossible, to solve nonlinear partial differential equation (1) by an equally intractable infinite set of nonlinear differential equations. Further progress will require that we truncate the spectral series given by (8). It follows that if one includes all those basis functions for which $m_\alpha \leq M$ and $n_\alpha \leq N$, then (11) represents a system of $N + 2MN$ nonlinear differential equations. [We note that this truncated set of spectral equations has been used by many other researchers, including Boville (1981) and Mukougawa and Hirota (1986b).] In Chapter 3 we will consider a linearized version of this finite system of equations, while in Chapter 4 we will employ the nonlinear equations themselves.

CHAPTER 3
LINEAR ANALYSIS

This chapter consists of three sections, each of which deals with a different theoretical aspect of the *linear* stability of the finite-amplitude steady-state flows derived in Section 2.2. The first section is essentially a parametric study of the linear stability of the equilibrium flows. More specifically, the frequency of all possible small-amplitude perturbations are calculated as a function of the strength of the mean zonal wind, u_s , and the amplitude of the topography, h_α . In this section a particular effort is made to characterize the various instability mechanisms. Following this, in Section 3.2, one of these instability mechanisms, namely form-drag instability, is considered in more detail. In this study the effect of the Reynolds stresses, which were absent in many earlier studies [e.g., Charney and Devore, 1979; Hart, 1979; Charney and Flierl, 1981; Rambaldi et al., 1985], on form-drag instability is emphasized. Finally, in Section 3.3 the stability of a particular *weakly* non-parallel equilibrium flow is studied numerically, as in the previous sections, and analytically, using WKB theory. In this section, part of the intention is to clarify the factors governing the regional nature of some of the instabilities found in the earlier sections.

3.1 LINEAR STABILITY OF FREE AND FORCED TWO-DIMENSIONAL WAVES

A large part of the initial motivation for the present study arose from the earlier work of Mitchell and Derome (1983). The latter have shown that rather realistic blocking-like flow patterns could be

generated as solutions of the quasi-geostrophic potential vorticity equation. The stability of these steady state flows was tested by means of numerical experiments in which a time-dependent version of the model equation was integrated forward in time using as initial conditions each of the equilibrium flows plus perturbations of various amplitudes. It was shown that a number of the flows were stable to small-amplitude disturbances while others were not, but because of the complexity of the equilibrium solutions, no general statement could be made about the stability of the solutions as a function of the parameters of the problem.

In the present study we are concerned with the linear stability of finite-amplitude wavy flows generated as in Mitchell and Derome, but for the simpler barotropic model described in Chapter 2. As discussed in Section 2.2 our idealized equilibrium flows are composed of a constant zonal wind plus a single planetary wave and are, therefore, too simple to be associated with blocking patterns. In this study we deal not only with free planetary waves as in Lorenz (1972) and Gill (1974) but also with topographically forced flows as in Charney and DeVore (1979). We show here that topographic, shear (Rayleigh) and resonant instabilities are possible, each having preferred regions in parameter space.

3.1.1- An overview

Most of the instability mechanisms to be described here have been studied before, but the present model makes it possible to present them in a unified fashion which, it is hoped, will be found helpful. In addition, it reveals the existence of an instability mechanism which, to the author's knowledge, has not been encountered before. Furthermore,

the model employed to obtain the growth rates uses many more degrees of freedom to define the structure of the perturbations than in the above studies, so that more accurate results are presented. The accuracy is gained at the expense of having to obtain the eigenvalues of relatively large matrices, and in that sense our approach is like that used by, for example, Frederiksen (1979) and Simmons et al. (1983); one important difference is that we allow the perturbations to interact with the bottom orography, hence permitting topographic instability. The growth rates of the disturbances are presented as functions of the amplitude of the single harmonic orography and of the speed of the mean zonal wind speed. The physics of the instability mechanisms in various parts of parameter space is illuminated by analyzing suitably simplified (truncated) models.

We show, in particular, that when the equilibrium flow is composed of a constant zonal wind u_s plus the gravest possible wave, the following is obtained: (a) the free Rossby wave is stable, whatever its amplitude; (b) for the topographically forced wave, three major instability regions are found in parameter space, two of which have stationary growing perturbations. One region corresponds to topographic instability (u_s somewhat superresonant), and the others being associated with shear or resonant triad instability (u_s subresonant). When the zonal wavelength of the equilibrium wave is halved, the free Rossby wave becomes unstable when its amplitude is sufficiently large. The topographically forced wave has two major regions of instability, roughly speaking, one on each side of the resonant u_s . Again the superresonant u_s domain contains topographic instability while the subresonant one contains either shear or resonant triad instability.

While the classical shear and resonant instability mechanisms are well understood, topographic instability appears to be less so, presumably because of its more recent history. To avoid confusion later in the discussion, we will now provide a definition of topographic instability (or form drag instability as it is often referred to). For our purposes, the phrase topographic instability is meant to describe a mechanism whereby a growing wave perturbation on the same scale as the forcing produces a substantial mean zonal flow with a nonzero meridional average through its interaction with the topography via form drag. In fact, such a zonal flow can only be generated by form drag in a barotropic model.

In subsection 3.1.2 we derive the linearized version of the model equation while in subsection 3.1.3 we describe the method of solution used to obtain the growth rates and the perturbation structures. In subsection 3.1.4 we present the numerical results and their analysis in terms of severely truncated models while in subsection 3.1.5 we summarize the main results.

3.1.2 Perturbation equations

It is our goal here to study the stability of the steady flow $\bar{\psi}$ as a function of m_α , n_α , μ_s and h_α/H . To this end we obtain the linear equation governing the evolution of a small amplitude perturbation ψ' to $\bar{\psi}$, i.e.,

$$\psi(x, y, t) = \bar{\psi}(x, y) + \psi'(x, y, t), \quad |\nabla\psi'| \ll |\nabla\bar{\psi}| \quad (12)$$

Substituting (12) into (1) and neglecting products of perturbations yields

$$\partial_t \Delta \psi' + J(\bar{\psi}, \Delta \psi') + J(\psi', \Delta \bar{\psi} + \beta y) + J(\psi', f_0 h/H) = 0. \quad (13)$$

Physically, speaking, the second term in (13) represents the advection of perturbation vorticity by the basic flow, while the third and fourth involve the generation of vorticity by perturbation flow across lines of constant basic-state potential vorticity. The possibility of interaction between the perturbation and the topography implied by the fourth term distinguishes this study from those involving the stability of a free Rossby wave [e.g., Lorenz (1972) and Gill (1974)].

To see more clearly the effect of the topography on the perturbation, it is instructive to consider the zonally averaged perturbation momentum equation. If we let

$$\psi(x, y, t) = \bar{\psi}(y, t) + \psi^*(x, y, t) \quad (14)$$

where the overbar represents a mean zonal average and an asterisk a deviation from it, then it can easily be shown that the integration of (13) with respect to y , with the use of the boundary condition $v(y=0) = 0$, yields

$$\partial_t \bar{u}' = - \partial_y \overline{(\bar{u}' v'^* + u' \bar{v}'^*)} + \overline{v'^* f_0 h/H} \quad (15)$$

This equation shows that the mean zonal perturbation velocity can be altered by two distinct processes. The first is seen to be due to the convergence of the Reynolds stress, resulting from an interaction between the perturbation and the equilibrium flow, while the second is associated with form drag, that is, to the interaction between the perturbation and the topography.

If we now integrate (15) from $y = 0$ to $y = D$ we obtain

$$d_t \int_0^D \overline{u'} dy = \frac{f_0}{H} \int_0^D \overline{v'^* h} dy \quad (16)$$

so that if a perturbation has a u' component with a nonzero area average, the latter must be the result of an interaction with the topography, that is, of the form drag mechanism. We will return to a discussion of (15) and (16) in the interpretation of our results.

Assuming solutions of the form

$$\psi' = e^{-i\omega t} \hat{\psi}(x, y) \quad (17)$$

and using (4) allows us to rewrite (13) as

$$-i\omega \Delta \hat{\psi} + \mathcal{J}(\bar{\psi}, \Delta \hat{\psi} + K_S^2 \hat{\psi}) = 0 \quad (18)$$

(Ultimately, of course, we will be interested in the real part of ψ' only.) Now we need only solve (18) for $\omega(m_\alpha, n_\alpha, u_s, h_\alpha/H)$ in order to establish the parametric domain of instability.

It should be noted that β in this study is considered constant, but even if it were a free parameter it could be removed from the problem by an appropriate nondimensionalization. It may be worthwhile to digress to outline one such procedure, since the nondimensional parameters which arise frequently occur in the literature. By introducing the nondimensional variables $(x^*, y^*) = K_S(x, y)$, $t^* = (\beta/K_S)t$ and $\hat{\psi}^* = (K_S/U)\hat{\psi}$, where U is the velocity amplitude of the basic wave, the $\omega(m_\alpha, n_\alpha, u_s, h_\alpha/H, \beta)$ problem can be replaced by a $\omega^*(m_\alpha, n_\alpha, UK_S^2/\beta, K_S/K_\alpha)$ problem. The nondimensional frequency ω^* is related to ω by $\omega^* = (K_S/\beta)\omega$.

When $\mu = K_S/K_\alpha = 1$ the ω^* problem then reduces to that of a free Rossby-wave stability analysis, which have been performed by Lorenz (1972) and Gill (1974) on an infinite β -plane. In agreement with Lorenz, Gill found that such flows will be unstable if the wave amplitude or wavenumber are sufficiently high. Moreover, Gill observed that for vanishingly small basic-wave amplitude [i.e., $M = UK_S^2/\beta \ll O(1)$, in his notation], the instability is actually of a resonant wave interaction nature while for large amplitude [i.e., $M = O(1)$] the instability is caused by the shearing motion of the wave itself. [Note that M here is different from that of Section 2.3.] Both of these authors used severely truncated Fourier expansions and as such were unable to specify accurate curves of marginal stability in the parameter space. Coaker (1977), using a numerical technique based on a third-order Floquet system, went a step further and actually obtained curves of marginal stability. A review of papers dealing with the stability of free waves can be found in Grötjahn (1984).

In the forced case (i.e., $\mu \neq 1$) it has been found that the topography may be destabilizing either because the topographic wave is unstable to a resonant or a shear mechanism or because the topography itself interacts favourably with the perturbation via form drag. This latter instability, which will be described in detail shortly was first discovered by Charney and DeVore (1979) and was later connected with the shear and resonant mechanisms by Charney and Flierl (1981). Both of these works relied on severely truncated systems and neither presented actual curves of stability. It is part of our purpose here to obtain such curves and, in addition, to relate our findings to those arising from a severely truncated model.

- Returning to the dimensional perturbation equation we will now outline the method of solution.

3.1.3 Method of solution.

To solve the perturbation equation (18) we expand $\hat{\psi}$ using the basis defined in (9), i.e.

$$\hat{\psi}(x,y) = \sum_{\beta} \hat{\psi}_{\beta} F_{\beta}(x,y) \quad (19)$$

which after applying the Galerkin procedure to (18) leads to the following set of algebraic equations for the coefficients $\hat{\psi}_{\beta}$

$$i\omega \cdot K_{\beta}^2 \hat{\psi}_{\beta} + \sum_{\epsilon} \Delta_{\epsilon} c_{\beta\alpha\epsilon} \tilde{\psi}_{\alpha} \hat{\psi}_{\epsilon} + u_s \sum_{\epsilon} \Delta_{\epsilon} b_{\beta\epsilon} \hat{\psi}_{\epsilon} = 0 \quad (20)$$

where $\Delta_{\epsilon} = K_{\beta}^2 - K_{\epsilon}^2$ and α refers to the basic-state wave. Alternatively, we could have obtained (20) by linearizing the spectral equations given in (11).

To this point we have transformed the perturbation equation (18) into an infinite-order matrix eigenvalue problem of the form

$$(A - i\omega I) \cdot X = 0 \quad (21)$$

where A is a real, and in general, nonsymmetric coefficient matrix depending on the basic state, I is the identity matrix, X is the eigenvector containing the components $\hat{\psi}_{\beta}$, and ω the eigenvalue. We may obtain approximate solutions by truncating the spectral series in (19) for β at $m_{\beta} = M$ and $n_{\beta} = N$. With this truncation A is a $(N + 2NM) \times (N + 2NM)$ matrix yielding $N + 2NM$ eigenvalues and $N + 2NM$

corresponding eigenvectors, which we calculated numerically using a series of EISPACK routines (Garbow, 1974). It was found, a posteriori, that a $[M,N] = [8,4]$ truncation (leading to a 68×68 matrix eigenvalue problem) satisfactorily resolved the dominant instabilities over the chosen range of parameters.

The fixed parameters in this analysis, D , f_0 , H , L and β , have the following assignments :

$$\begin{aligned}
 D &= 4 \times 10^6 \text{ m} \\
 f_0 &= 2\Omega \sin(\theta_0) \\
 H &= 1 \times 10^4 \text{ m} \\
 L &= 2\pi R \cos(\theta_0) \\
 \beta &= 2\Omega \cos(\theta_0)/R
 \end{aligned} \tag{22}$$

where the rotational rate of the earth, Ω , the radius of the earth, R , and the mid-channel latitude, θ_0 , are $7.292 \times 10^{-5} \text{ s}^{-1}$, $6.37 \times 10^6 \text{ m}$ and 45°N , respectively. Also, by way of reducing the parameter space and hence the amount of calculation, we consider topographies which have only either a zonal-wavenumber-1 or -2 structure and half an oscillation in the meridional direction, i.e.,

$$m_\alpha = 1 \text{ or } 2 \text{ and } n_\alpha = 1 \tag{23}$$

This selection is to some extent justified by the fact that these two components contain the bulk of the amplitude of the earth's topographic spectrum.

In the next subsection we present an overall picture of the stability of zonal-wavenumber-1 and -2 basic flows. In both cases we follow the same format, by first analyzing the stability characteristics

of the Rossby wave and then the topographically forced wave from the point of view of instability curves and instability mechanisms (e.g., form drag, resonant interaction or shear instability). Guided by the numerical results, we also use a severely truncated model to help distinguish the various instabilities and to obtain instability criteria.

3.1.4 Parametric analysis

Here we present a stability analysis of free and topographically forced zonal-wavenumber-1 and -2 basic waves

a. Zonal-wavenumber-1 basic wave

1) FREE ROSSBY WAVE

Since permitting a free Rossby wave to assume a nonzero phase speed has the sole effect, from the point of view of stability, of doppler shifting the phase speed of its perturbation it is sufficient to take it to be stationary. Given the channel parameters used here, the actual mean zonal wind required to balance the meridional advection of planetary vorticity and fix the Rossby wave in space is approximately 24.30 m s^{-1} . We found this zonal-wavenumber-1, stationary, free Rossby wave to be unconditionally stable. We will now argue that the stability of this wave is a consequence of the conservation of various quantities in the system (i.e., energy, enstrophy and zonal momentum) and the inclusion of lateral boundaries.

Fjortoft (1953) showed that if both the kinetic energy and enstrophy (i.e., mean square vorticity) are to be conserved, energy must

be transferred simultaneously to both shorter and longer wavelengths. This dynamic constraint, together with the fact that the geometry of our model fixes a lower bound on the set of possible wavenumbers, requires the basic wave to interact with a mean zonal flow. Specifically, this (1,1) free Rossby wave must interact with a (0,1) perturbation component for instability to occur since it is the only mode with a smaller wavenumber. Since, however, the (0,1) mode is constrained to remain constant in order to maintain the conservation of zonal momentum [see (16) with $h = 0$], stability of the basic wave is guaranteed regardless of its amplitude. This is essentially the same reason why Baines (1976) found that Rossby-Haurwitz waves with a total wavenumber less than 3 are unconditionally stable.

2) TOPOGRAPHICALLY FORCED WAVE

In contrast to the free Rossby wave, the topographic wave may or may not be stable, depending on the actual wave amplitude and the mean zonal wind. Despite the complex relationship that exists between instability and these parameters, at least two general comments can be made. First, all the major instabilities encountered here contain at least some mean zonal kinetic energy (in contradistinction to purely zonal basic-state instabilities, which contain no mean zonal kinetic energy). Second, they are all on roughly the same scale as the basic wave (making their resolution a relatively easy task).

We begin the analysis by presenting e-folding curves (see Fig. 2), for the fastest-growing perturbations, as a function of topographic amplitude and mean zonal wind. Following this we consider representative eigenfunctions from the various regions of instability

and propose an instability mechanism in each case. Finally, motivated by the numerical results, we recommend a simple theoretical model useful in analyzing these instabilities

(i) *Eigenvalues* From Fig. 2a we first observe that mean zonal winds exceeding approximately 26 m s^{-1} lead to unconditionally stable flows. This is a direct consequence of the conservation of a unique linear combination of horizontally integrated perturbation energy and enstrophy (see Charney and Flierl, 1981, p. 537). The exact mean zonal-wind cutoff, so determined, depends only on the β -parameter and the channel width, i.e.,

$$u_s \geq \beta / \left(\frac{\pi}{D}\right)^2 \approx 26.24 \text{ m s}^{-1} \quad (24)$$

The stabilizing influence of the lateral boundaries is evident in (24), which shows, that for a fixed u_s , stability is ensured provided the boundaries are sufficiently close together. McIntyre and Shepherd (1986) present a nice physical interpretation of this result and aptly stress the fact that it applies more generally to finite amplitude disturbances, as first demonstrated by Arnold (1966).

On the near superresonant side and contiguous to the resonant wind line (located at $u_s \approx 24.30 \text{ m s}^{-1}$) is a major region of instability (denoted region I). This instability is characterized by resonantly amplified perturbations that are fixed in space. These features suggest that this instability may result from a form drag mechanism, and indeed, after considering a representative eigenfunction in subsection II there should be no doubt that this is truly the case. It should be noted that due to the near resonant nature of this instability, the basic wave

amplitudes can be exceedingly large and the quasi-geostrophic assumption underlying the entire theory often violated.

On the subresonant side of the resonant wind line are indicated two distinct regions of instability [denoted II(a,b)]. Between region I and region II(a) lies an area for which no growing perturbations whatsoever were found, while to the left of region II(b) some very limited areas of instability were discovered. The growth rates in these regions are relatively small, however, and for this reason have not been shown.

Growing perturbations from region II(b) are characterized by non-zero phase speeds whereas those from region II(a) are fixed in space. In general, regions II(a,b) both involve structures dominated by the same three components, leading us to believe that they arise from the same mechanism. We will see in subsection ii that this instability arises from shear instability inherent in the topographic wave itself rather than through any direct interaction between the perturbation and the topography as in the case of form drag instability.

(ii) *Eigenfunctions* Now we consider a representative eigenfunction from each of the three regions of instability described previously.

(a) Superresonant¹ instability. The typical growing perturbation from region I has a wavy part corresponding to, yet out of phase with, the topography. In addition to a dominant (1,1) component, the perturbation has also a strong (0,1) component. For example, consider Fig. 3b, which is the growing perturbation to the basic flow shown in

¹Superresonant with respect to this particular wavenumber.

Fig. 3a. Since the perturbation amplitude is undetermined in this linear theory, the contours are left unlabeled.

The physical mechanism responsible for this exponential growth involves the interaction between the perturbation and both the topography and the equilibrium wave. Referring again to Fig. 3b we see that the perturbation high east of the mountain induces southerlies over the mountain and northerlies over the valley, leading to vortex shrinking in the southern half of the channel and vortex stretching in the northern half. This implies a generation of anticyclonic and cyclonic vorticity in the south and north, respectively, leading to an increase in the zonally averaged midchannel wind. The strengthened westerly zonal flow, in turn, advects the basic wave ridge in such a way as to reinforce the perturbation high, thereby ensuring a positive feedback of the perturbation onto itself.

To see more clearly the role of form drag in this instability we present Fig. 4, which shows the distribution of the Reynolds stress and form drag for this representative case. Form drag clearly dominates the overall zonal momentum tendency and, as expected, is the sole source of the large (0,1) component. The Reynolds stress, on the other hand, is much weaker but its (0,3) structure does moderate to some extent the effect of the form drag. Note that an analysis based on severe truncation, such as Charney and DeVore's (1979), would miss altogether the effect of the Reynolds stress.

(b) Subresonant instability. We reiterate that, in general, the unstable subresonant structures from regions II(a,b) are dominated by the same three components, namely the zonal (0,2) and the wavy (1,2) and

(2,1) modes. The various structures themselves differ only, in that the amplitudes of the three dominant modes have different ratios. All the mean zonal components in these perturbations [not only the dominant (0,2) one] have an even meridional wavenumber, and for this reason their growth is clearly not the consequence of a form-drag mechanism [see (16)]. We now present a representative eigenfunction from each of II(a,b) and also a description of a weak subresonant topographic instability lying outside regions II(a,b).

Region II(a). Growing perturbations found in region II(a) have a small, but nonzero, mean zonal part and a dominant zonal-wavenumber-2 structure. Specifically, in increasing order of importance, the (0,2), (1,2) and (2,1) components dominate these structures. To illustrate this, we present Figs. 5b, c, which show the growing and damped perturbations, respectively, to the basic flow of Fig. 5a. Recall that these perturbations have zero phase speeds so that the structures shown here will not change outside an overall exponential amplitude growth or decay.

It is apparent that this instability is not a response to a form-drag mechanism, but, rather arises from a tilted ridge/trough mechanism (acting upon shears inherent in the topographic wave) involving the wavy (1,2) and (2,1) components. In simple terms, the tilted phase lines seen in Figs. 5b, c allow the disturbance to carry momentum away from (to) the jets in the basic flow, causing the latter to weaken (strengthen) and, in turn, the disturbance to grow (dampen). It should be mentioned that unlike classical barotropic instability on a purely zonal basic flow, the disturbances to the two-dimensional flows considered in this study invariably exhibit some modulation of the wave

structure along the zonal direction. As would be expected, Figs. 5b, c show that the modulation is on the scale of the equilibrium flow, namely, zonal wavenumber one.

To assess their respective roles in this instability, we present the Reynolds-stress and form-drag distributions in Fig. 6. Notice that the weak form drag works against the Reynolds stress in forcing the (0,2) component.

Region II(b) As already mentioned, the region II(b) structures are dominated by the same components as in region II(a) and likely arise from a similar if not identical mechanism. Unlike the region II(b) structures, however, these structures all undergo an amplitude modulation in time (other than exponential growth) due to the presence of a nonzero phase speed. Figs. 7b, c show a growing perturbation at 0 days and 9 days, respectively, to the basic flow depicted in Fig. 7a. Throughout its period of oscillation, this perturbation has a pronounced zonal-wavenumber-2 structure similar to the typical region II(a) perturbation shown in Fig. 5b.

The Reynolds-stress and form-drag profiles for the perturbation at $t = 0$ are shown in Fig. 8. Notice that the form drag has a greater relative importance than in the region II(a) example. This might be expected since the basic flow, which is further from linear resonance, results in a reduced Reynolds stress contribution.

At this point we would like to report that wedged between (and occasionally overlapping) the two major subresonant instability regions are some small pockets of what appears to be travelling form-drag instabilities (albeit weak). To the author's knowledge all previous studies of topographic instability have yielded stationary disturbances.

We will now present an example of a travelling, subresonant topographic instability.

Consider, for instance, the travelling perturbation in Fig. 9b to the weakly unstable, subresonant basic flow of Fig. 9a. The Reynolds-stress and form-drag profiles for the perturbation at this and various other times are shown in Fig. 10. The profiles at $t = 0, T/8, T/4$ and $3T/8$ are simply the mirror images of those at $t = T/2, 5T/8, 3T/4$ and $7T/8$, respectively.

The inspection of figures corresponding to Fig. 9b but at other times (not shown), as well as consideration of the frequency, reveals the presence of a dominant westward-travelling (1,1) wave, with phase speed of approximately 10.9 m s^{-1} . This wave interacts with the topography to produce either a westward or eastward (0,1) zonal flow, depending on its precise location in the channel (Fig. 10). It is interesting that at $t = 3T/4$, when the effect of form drag is almost at the maximum over the entire oscillation of 29.5 days, the profiles of Reynolds stress and form drag are nearly identical to those of the superresonant case of Fig. 4. To check that this instability is not merely an artifact of the truncation, we increased the resolution to $[M,N] = [15,15]$ and found that it remained, with now an e-folding time of 35 days (the additional components having increased the growth rate). In any case, we should keep in mind that this subresonant topographic instability is still rather weak.

Pedlosky (1981), recognizing the limitations of severe truncation, found in his analytical model that subresonant topographic instability was possible if the zonal wavelength of the topography was long enough (in particular if $k_\alpha < \pi/\sqrt{3D} \approx 0.58\pi/D$ in our notation). Our (1,1)

topography certainly satisfies this condition since $k_\alpha \approx 0.28\pi/D$. The subresonant instability encountered here, however, should not be confused with that discussed by Pedlosky. The instability here is not stationary nor is the basic state weakly forced and nearly resonant as required under the assumptions of his model. As pertains the instability discussed by Pedlosky we will show in Section 3.2 that it is in fact an artifact of severe truncation.

(iii) *Severely truncated model.* Inspired by the numerical results, we now consider the stability of a basic wave, denoted by α (which is arbitrary at this point), to a perturbation made up of two other waves and a zonal component, i.e.,

$$\begin{aligned} \psi' = e^{-i\omega t} & \left\{ \hat{\psi}_\gamma \sqrt{2} \cos\left(\frac{\pi n_\gamma y}{D}\right) \right. \\ & + \hat{\psi}_\beta 2 \sin\left(\frac{2\pi m_\beta x}{L_\beta}\right) \sin\left(\frac{\pi n_\beta y}{D}\right) + \hat{\psi}_\beta 2 \cos\left(\frac{2\pi m_\beta x}{L_\beta}\right) \sin\left(\frac{\pi n_\beta y}{D}\right) \\ & \left. + \hat{\psi}_\epsilon 2 \sin\left(\frac{2\pi m_\epsilon x}{L_\epsilon}\right) \sin\left(\frac{\pi n_\epsilon y}{D}\right) + \hat{\psi}_\epsilon 2 \cos\left(\frac{2\pi m_\epsilon x}{L_\epsilon}\right) \sin\left(\frac{\pi n_\epsilon y}{D}\right) \right\} \end{aligned} \quad (25)$$

With no loss of generality, we assume that the various wavenumbers are such that the interacting triads are (γ, α, β) and $(\beta, \alpha, \epsilon)$. The frequency equation arising from this configuration is given by the fifth-order equation

$$\omega^5 - b\omega^3 + c\omega = 0 \quad \text{where} \quad (26a)$$

$$b = \omega_\beta^2 + \omega_\epsilon^2 + 2A_{\beta\epsilon} + A_{\gamma\bar{\beta}} \quad (26b)$$

$$c = (\omega_\beta\omega_\epsilon \pm A_{\beta\epsilon})^2 + (\omega_\epsilon^2 + A_{\beta\epsilon})A_{\gamma\bar{\beta}} \quad (26c)$$

In (26c) the positive sign is taken if $m_\alpha = m_\beta + m_\epsilon$ and the negative sign if otherwise. Also, ω_β and ω_ϵ are just the linear Rossby wave frequencies for the β and ϵ components, while $A_{\beta\epsilon}$ and $A_{\gamma\bar{\beta}}$ measure the interaction effect of the β component with the ϵ component and the γ component with the $\bar{\beta}$ component, respectively. [see Appendix A for definitions of the various terms in (26).]

We now treat several special cases of (26) in order to permit a simple analytic analysis of the various instabilities to these zonal-wavenumber-1 basic states [$\alpha = (1,1)$].

(a) Superresonant instability. Since the numerical results reveal that growing perturbations in the superresonant regime are dominated by the $(0,1)$, and $(1,1)$ components, we set $\gamma = (0,1)$, $\beta = (1,1)$ and $\epsilon = (0,0)$. The nontrivial frequencies so obtained, after putting $\omega_\epsilon = 0$ and $A_{\beta\epsilon} = 0$ in (26), are

$$\omega = \pm i \left[-\omega_\beta^2 - A_{\gamma\bar{\beta}} \right]^{1/2} \quad (27)$$

In this case the necessary conditions for instability are obviously

$$\omega_{\beta}^2 < -A_{\gamma\bar{\beta}} \quad (28a)$$

$$A_{\gamma\bar{\beta}} < 0. \quad (28b)$$

Referring to Appendix A, we see that the second inequality fixes the range of potentially unstable mean zonal winds, i.e., $\beta/K_{\beta}^2 < u_s < \beta/K_{\gamma}^2$ (specifically, $24.30 \text{ m s}^{-1} < u_s < 26.24 \text{ m s}^{-1}$). This is the β -plane channel analog of a result obtained for an infinite β -plane by Charney and Flierl (1981). Because β is positive and $u_s = \beta/K_s^2$, we can write our result as $K_{\gamma}^2 < K_s^2 < K_{\beta}^2$, which is the analog of Fjortoft's (1953) result regarding the scales of three modes involved in an energy exchange. Note that here, the result applies to a topographically forced model and that the intermediate wavenumber is not that of the equilibrium streamfunction but that of the resonant scale associated with the mean zonal wind u_s . In short, then, the conclusion is that the growing disturbance must possess at least two scales, one larger and one smaller than the resonant scale. In a bounded domain such as ours, the perturbation scale K_{γ} is bounded from below and therefore so is K_s , implying an upperbound on u_s for instability. The first inequality, on the other hand, determines the minimum basic wave amplitude required for instability to occur. This condition can be physically interpreted as demanding that the dispersive effects of β (embodied in ω_{β}) are overcome by those of wave interaction (measured by $A_{\gamma\bar{\beta}}$).

Many of the essential features of region I instability (e.g., resonant amplification and zero phase speed) are reflected in (27), and

indeed, even quantitatively this expression serves remarkably well. This last point can be justified by comparing the superresonant e-folding curves of Fig. 2a and Fig. 11a, the former being obtained with the full numerical model and the latter using (27). It is interesting to note that (27) consistently overestimates the instability. A discussion on the topic of form-drag instability, using a simple system similar to this, can be found in Buzzi et al. (1984) (see also Revell and Hoskins, 1984).

The subresonant curves seen in Figs. 11a, b were obtained using a simple three component model, which we now describe.

(b) Subresonant instability. The numerical evidence suggests that we should select a perturbation composed of $\gamma = (0,2)$, $\beta = (1,2)$ and $\xi = (2,1)$ in order to model the two dominant subresonant instabilities encountered here. For this truncated system the conserved energy/enstrophy integral discussed earlier is useful (the reader is again referred to Charney and Flierl, 1981), since it implies that the potentially unstable mean zonal winds lie between, and only between, β/K_β^2 and β/K_ϵ^2 , in other words between approximately 6.43 m s^{-1} and 19.89 m s^{-1} . Returning to (26) we will argue that with this severely truncated system each of regions II(a,b) may be adequately reproduced and distinguished on the basis of the respective signs of b , c and $b^2 - 4c$. To aid us in this endeavour we recall that region II(a) instabilities are stationary whereas those from region II(b) are travelling.

Upon inspecting the frequency equation (26) it becomes apparent that perturbations of this sort to basic flows for which

$$b^2 - 4c < 0 \quad (29)$$

are *unstable* and *travelling*. The neutral curve associated with these perturbations is obtained by making (29) an equality, i.e.,

$$\begin{aligned} A_{\gamma\beta}^2 + 2(\omega_\beta + \omega_\epsilon)[2(\omega_\beta + \omega_\epsilon)A_{\beta\epsilon} + (\omega_\beta - \omega_\epsilon)A_{\gamma\beta}] \\ + (\omega_\beta + \omega_\epsilon)^2(\omega_\beta - \omega_\epsilon)^2 = 0. \end{aligned} \quad (30)$$

This, in turn, yields a simple relationship between the critical topographic amplitude and the constant mean zonal wind speed. Figure 11b shows the neutral curve, so determined, as well as a few e-folding curves within the region. From a comparison of Figs. 2b and 11b we conclude that this low-order system resolves extremely well the region II(b) instability discussed earlier.

The fact that the curves in Fig. 2b (and 11b) are slanted towards the u_s axis at approximately 15.4 m s^{-1} may be understood with the aid of (30). When the constant mean zonal wind speed is such that

$$\omega_\beta + \omega_\epsilon = 0 \quad (31)$$

(which occurs when $u_s \approx 15.4 \text{ m s}^{-1}$) then (30) will only be satisfied for a vanishing topographic amplitude. It follows that the slope of the e-folding curves is connected to a resonant triad interaction between the (1,2) and (2,1) components of the perturbation and the (1,1) component of the basic state, at a constant mean wind speed of approximately 15.4 m s^{-1} .

To obtain an explicit (albeit approximate) necessary condition for region II(a) instability, we note that if the basic flow is unstable and

$$b_1^2 - 4c \geq 0 \quad (32)$$

then the growing perturbations will be stationary. Whether a particular flow satisfying (32) is actually unstable or not will depend on the signs of b and c . For example, if $c < 0$, i.e.,

$$(\omega_\beta \omega_\epsilon - A_{\beta\epsilon})^2 < -(\omega_\epsilon^2 + A_{\beta\epsilon}) A_{\gamma\beta} \quad \text{and hence} \quad (33a)$$

$$(\omega_\epsilon^2 + A_{\beta\epsilon}) A_{\gamma\beta} < 0 \quad (33b)$$

the flow will be unstable, and since (32) is automatically satisfied the growing perturbations will be stationary. In this case the second inequality in (33) presents two possibilities, either

$$A_{\gamma\beta} > 0 \quad \text{and} \quad \omega_\epsilon^2 + A_{\beta\epsilon} < 0 \quad (34a)$$

or

$$A_{\gamma\beta} < 0 \quad \text{and} \quad \omega_\epsilon^2 + A_{\beta\epsilon} > 0. \quad (34b)$$

From the definition of $A_{\beta\epsilon}$ and $A_{\gamma\beta}$, it can be seen that (34a) demands $\beta/K_\beta^2 < u_s < \beta/K_\gamma^2$ for instability to appear (i.e., $6.43 \text{ m s}^{-1} < u_s < 6.56 \text{ m s}^{-1}$). This, therefore, is not a candidate as a necessary condition for region II(a) instability, since region II(a) instability occurs at mean zonal winds exceeding 6.56 m s^{-1} . This range of unstable mean zonal winds corresponds, rather, to a very narrow region of weak instability discovered with the higher resolution model and ignored here because of the negligible growth rates involved. The second pair of inequalities [i.e., (34b)] on the other hand, imply that $\beta/K_\gamma^2 < u_s < \beta/K_\epsilon^2$ ($6.56 \text{ m s}^{-1} < u_s < 19.89 \text{ m s}^{-1}$) for unstable flow. The neutral curve corresponding to this region is shown in Fig. 11a, again

with a few e-folding curves indicated. A comparison of Figs 2a and 11a should leave no doubt that (33a) and (34b) are necessary conditions related to region II(a) instability.

The only other candidate for instability, within this severely truncated setting, occurs when $b^2 - 4c > 0$ with $b < 0$ and $c > 0$. It happens however, that $b > 0$ for $2h_\alpha/H < 0.2$ and $6.43 \text{ m s}^{-1} < u_s < 19.89 \text{ m s}^{-1}$, so that in the range of parameters considered here this is not a viable possibility. The reason that $b > 0$ in this parameter range is due to the fact that the interaction effects embodied in the last two terms of b are small when compared with the dispersive effects of β as felt through the first two terms of b for these relatively weakly forced and linearly nonresonant flows.

Although this truncated system may have given us little physical insight into the subresonant zonal-wavenumber-1 instabilities, it could yield useful information upon further study, especially in connection with the relationship between the growth rates of perturbations and their periods.

Now we turn to a stability analysis of zonal-wavenumber-2 basic waves.

b. Zonal-wavenumber-2 basic wave

1) FREE ROSSBY WAVE

In contrast to the zonal-wavenumber-1 case, we found that the zonal-wavenumber-2 free Rossby wave will be unstable if the wave amplitude is large enough. Specifically, if the rms wind speed generated by the basic wave exceeds approximately 13.5 m s^{-1} the flow

will be unstable. On the other hand if the rms wind speed is too large, say greater than approximately 75.0 m s^{-1} , the instability mechanism cuts off and stability ensues. Also, no instability with an e-folding time less than 10.0 days was found. All of the above observations are based on a $[M,N] = [10,10]$ truncation. Interestingly, the $[M,N] = [8,4]$ truncation consistently overestimated the instability

The fastest-growing perturbation to the free Rossby wave flow of Fig 12a is shown in Fig 12b (here the rms wind speed in $\bar{\psi}$ is 20.0 m s^{-1}). In this case the $[M,N] = [8,4]$ truncation was found to adequately resolve the instability. This travelling disturbance is purely wavelike (i.e., it contains absolutely no nonzero mean zonal components), and the (1,2), (3,1) and (1,1) components dominate the structure (in ascending order of importance). Figure 12c shows the same disturbance after 16 days (or, approximately one-quarter of its total period of oscillation), with the exponential growth suppressed.

The stability of the free Rossby wave at small amplitude is connected to boundedness of the domain. If this wave were unbounded in the meridional direction, then when $M \ll 1$ (i.e., when the nonlinear effects are weak) it would be unstable via a second-order resonant interaction (as demonstrated by Gill, 1974). Plumb (1977) has shown, however, that a very long wave (specifically, if its longitudinal wavenumber k_α is less than $0.681\pi/D$) in a meridionally bounded domain will be stable in this small amplitude limit. In short, we conclude that this long Rossby wave (for which $k_\alpha \approx 0.565\pi/D$) is stable in this limit because of the boundedness of the domain.

2) TOPOGRAPHICALLY FORCED WAVE

Here we follow the same format as before, by considering the various instabilities in detail, beginning with eigenvalues, then eigenfunctions, and finally, with a severely truncated system.

(i) *Eigenvalues* In Fig. 13 there are two major and distinct regions of instability separated by the resonant wind line located at approximately 19.89 m s^{-1} . On the near superresonant side is a region (region III) of form drag instability, which as before, is characterized by perturbations which are resonantly amplified and fixed in space. Since this instability arises from the same mechanism and has the same essential features as that from region I, which we have already described in detail, we will dispense with it and consider the subresonant instability (region IV) only.

In general, the real part of the frequencies of the growing perturbations from region IV are nonzero, and hence the perturbations have the appearance of propagating waves. The fact that this region is contiguous to the resonant wind line suggests that it may be in some way connected to the free Rossby-wave instability encountered earlier. This conjecture will be strengthened when we consider some typical unstable eigenfunctions in subsection ii. Unlike the free Rossby-wave case, however, a resonant wave interaction is also possible, leading to nonzero growth rates even for vanishingly small basic wave amplitudes. (This occurs in the limit as $h_\alpha \rightarrow 0$ and $u_s \rightarrow 15.37 \text{ m s}^{-1}$.) A severely truncated system formulated in subsection iii will help us understand the form this particular resonant interaction takes.

As in the case of zonal-wavenumber-1 basic flows, there are other subresonant instabilities, which because of the very small growth rates involved we have chosen to ignore. Now we will consider two eigenfunctions from region IV, corresponding to small and large basic wave amplitude, respectively.

(ii) *Eigenfunctions*. As in the case of the growing perturbations to the free Rossby wave, the growing perturbations to the forced wave in region IV have no mean zonal part whatsoever. Obviously, then, form drag is not operative here, leaving shear and resonant interaction mechanisms as the only instability candidates. Let us consider the latter first. True resonant interaction instability involving a free Rossby wave exists only in the limit as the basic wave amplitude tends to zero (see Coaker, 1977). Moreover, the wavenumbers of the triad involved in the resonant interaction must be such that a particular dispersion relationship is satisfied, a fact which in a bounded domain severely restricts the set of waves in the perturbation capable of undergoing a resonant interaction leading to instability. On the other hand, in the case of a topographically forced basic state, the fact that the mean zonal wind, u_s , is a free parameter makes it significantly easier for this same dispersion relationship to be satisfied for a given set of waves. A case in point is this particular zonal-wavenumber-2, topographically forced basic state, in which, for a vanishingly small forcing, the (1,1) and (1,2) components in the perturbation resonantly interact with the (2,1) component of the basic state at $u_s \approx 15.37 \text{ m s}^{-1}$ (as evidenced by the zero located at 15.37 m s^{-1} in Fig. 13).

We have chosen the topographically forced basic flow of Fig. 14a to illustrate the resonant-wave interaction mechanism encountered here. (The value of M for this basic flow is approximately 0.03) The growing perturbation to this basic flow is clearly dominated by the (1,1) and (1,2) components. (See Fig. 14b.) Like instability on a purely zonal basic state this perturbation appears as a simple sinusoidal travelling wave (in this case moving westward at the rate of approximately 8.9 m s^{-1}) undergoing an overall exponential amplification (of approximately 0.3% per day in this case). Under closer examination, however, it is seen that the wave also exhibits some slight meridional propagation as well as changes in its tilt as it moves through the channel, due to the nonzonality of the basic state (See Fig. 14c.)

As in the free Rossby wave problem described by Gill (1974), as the amplitude of the topographically forced wave is increased (by, either increasing the topographic height or moving nearer linear resonance) the number of waves in the perturbation able to abstract energy from the basic flow significantly increases. With this comes a shift from a resonant interaction mechanism to a shear-type instability (more characteristic of purely zonal basic flows). In the case at hand, the first nonresonant interaction component to appear, as the basic wave amplitude is increased, is the (3,1) mode. Recalling the earlier free Rossby-wave analysis, these components [i.e., (1,1), (1,2) and (3,1)] are the same dominant modes in the growing structures encountered there. This, then, gives us reason to believe that region IV instability (for moderately forced basic states) may in some sense simply be an extension of the free Rossby-wave instability.

Consider the growing perturbation shown in Fig. 15b to the basic flow of Fig. 15a (now, $M \approx 1.0$). The perturbation is quite localized in space with its maximum amplitude occurring between the basic-state ridge and trough lines (indicated with R's and T's, respectively). To illustrate the time evolution of this structure (with the exponential growth suppressed) a 40-day Hovmöller diagram, through the center of the channel, is shown in Fig. 15c. The perturbation seems to represent a series of highs and lows all simultaneously undergoing a 35-day oscillation. The regions of maximum intensification lie directly between the basic-state ridge and trough lines, where, in fact, the largest shears are to be found. This is consistent with Frederiksen (1979), who related regions of maximum perturbation growth to features in the basic flow. (Frederiksen considered a baroclinic model without topography which is, of course, quite different from ours.) We mention that in Section 3.3 we will attempt to delineate the factors responsible for the local growth of linear disturbances such as this one.

Now we will use a severely truncated model to help elucidate the resonant interaction mechanism responsible for the instability of the small-amplitude region IV basic flows.

(iii) *Severely truncated model.* The dominant modes in the unstable resonant interaction structures are (1,1) and (1,2), so in (26) we set $\beta = (1,1)$, $\epsilon = (1,2)$ and ignore the zonal component. With $A_{\gamma\beta} = 0$ we get that

$$\omega = \frac{1}{2} \left\{ (\omega_\beta - \omega_\epsilon) \pm i \left[-(\omega_\beta + \omega_\epsilon)^2 - 4A_{\beta\epsilon} \right]^{1/2} \right\} \quad (35)$$

from which the following necessary conditions for instability result:

$$(\omega_{\beta} + \omega_{\epsilon})^2 < -4A_{\beta\epsilon} \quad \text{and hence,} \quad (36a)$$

$$A_{\beta\epsilon} < 0. \quad (36b)$$

As for perturbations in region II(b), a growing perturbation here has a nonzero phase speed since

$$\omega_r = \text{Re}(\omega) = (\omega_{\beta} - \omega_{\epsilon})/2. \quad (37)$$

Similarly, there is the possibility of instability even for vanishingly small basic-wave amplitude. This can be seen by setting

$$\omega_{\beta} + \omega_{\epsilon} = 0 \quad (38)$$

in (36a). Now if (38) can be met for some u_s (which in this case occurs at the now familiar value of $u_s \approx 15.37 \text{ m s}^{-1}$) then (36) is automatically satisfied and the flow will be unstable for any nonzero forcing. This is precisely the dispersion relationship to which we alluded in subsection ii.

3.1.5 Discussion

A quasi-geostrophic β -plane channel model has been used to investigate the linear stability of free and forced barotropic planetary waves. By expanding the perturbation-wave structure in terms of orthonormal basis functions, the problem was cast in the form of a standard matrix eigenvalue problem. The calculations were made with sufficient resolution to ensure the accuracy of the frequencies (eigenvalues) and of the wave structures (eigenfunctions), but extensive

use was made of severely truncated models in the interpretation of the results. Calculations were made for an equilibrium flow composed of a constant zonal flow and one wave having either a zonal-wavenumber-1 or -2 structure; in both cases the wave had the gravest possible meridional scale permitted by the channel.

The free Rossby wave with zonal wavenumber 1 was found to be stable, whatever its amplitude. The stability of this wave was seen to be directly linked to the boundedness of the domain. The topographically forced zonal wavenumber 1, on the other hand, was found to be stable or unstable, depending on the amplitude of the topography and the strength of the constant mean zonal flow u_s . Three major and distinct regions of instability were found. One region, as expected from Charney and DeVore (1979), contained orographically unstable flows and occurred for u_s somewhat superresonant. Two major unstable regimes were found when u_s was subresonant, but only one having appreciable growth rates. Interestingly, the growing perturbations were found to be stationary for two of the three unstable domains of instability for this wave. No satisfactory explanation for this result can be offered at this time. We also reported on the existence of a weak, subresonant and travelling topographic instability.

As for zonal wavenumber 2, the free Rossby mode was found to be unstable when its amplitude was neither too small nor too large, but the e-folding times obtained were always greater than ten days. The forced wavenumber 2 showed two contiguous regions of instability, one on either side of the resonant u_s . Naturally, the somewhat superresonant u_s was associated with orographic instability. In the subresonant region, the instability mechanism was shown to be associated with a

resonant-triad interaction when the wave amplitude was small and to transform into shear (Rayleigh) instability as the wave amplitude was increased. The latter type of instability was shown to be associated with somewhat more localized perturbations which change shape over a well-defined period as they move through the equilibrium wave. Being more localized, these perturbations require more modes for their description and hence are less well represented by severely truncated models than the other main instabilities reported upon in this paper.

The model used in this study has, admittedly, a rather crude geometry but it has nevertheless been a useful tool in demonstrating the strong constraints that the finiteness of the domain can impose on the flow, which Gill (1974) referred to in his work with the infinite β -plane. The model's simplicity has also made it possible to obtain a reasonably coherent picture of the stability properties of both free and forced planetary waves and to delimit in parameter space the regions of instability. Finally, the investigation revealed the existence of travelling topographically unstable waves, which do not seem to have been noticed before.

In the next section we will discuss the form-drag instability in considerably more detail. We will, in particular, describe the structure the perturbation must have (in both the mean zonal and eddy parts) in order to describe properly this instability.

3.2 Some effects of truncation on topographic instability

The fact that zonal flows, which are otherwise stable, may be unstable in the presence of a sinusoidal topography was demonstrated by Charney and DeVore (1979) in their pioneering paper on multiple equilibria. They found topographic instability to be a stationary phenomenon associated exclusively with their near-superresonant equilibrium solution. Hart (1979) arrived at the same characterization of topographic instability without, however, the constraint of severe truncation. Hart's description of topographic instability is still less than general though, because of his assumption of a meridionally infinite topography

Recognizing the limitations of Charney and DeVore's severe truncation, and Hart's highly anisotropic orography, Pedlosky (1981) performed a multiple scaling analysis which indicated, among other things, a sensitivity to the meridional scale of the topography not evident in the earlier studies. For instance, subresonant topographic instability was found to exist when the ratio of the cross-stream wavenumber to the downstream wavenumber was large enough. Using a somewhat more descriptive approach, and without Pedlosky's stringent scaling assumptions, Rambaldi et al. (1985) derived essentially the same instability criterion.

All of the studies described above are identical in at least one respect: they all describe a disturbance to the forced equilibrium flow consisting of a single free wave, with the same zonal and meridional wavenumber as the forcing, and a mean zonal flow. Aside from the benefit of analytic tractability, this assumption ensures that any instability that arises is the direct consequence of the presence of topography, rather than a shear (or resonant) mechanism connected to the

equilibrium wave itself. With such a disturbance the only way the mean zonal flow can change (say exponentially) is through the interaction of the free wave with the topography via form drag, since the Reynolds stresses are absent.

In this study, besides the on-scale free wave we include many other waves in the perturbation, all having the same zonal wavenumber as the topography but different meridional wavenumbers. This necessarily entails a numerical approach to the stability analysis. Following from the previous section, our philosophy here is to resolve a given instability as well as possible and then by systematic simplification (i.e., successive truncations) determine the minimum system required for its reasonably true description. To circumvent the problem of disentangling one instability mechanism from another we will exploit certain symmetries inherent in the resultant matrix eigenvalue problem.

In subsection 3.2.1 we will rewrite the perturbation equations in a manner better suited to this particular analysis, while in subsection 3.2.2, we will rederive the instability criterion mentioned earlier so that the pitfalls of some severe truncations are made apparent. In subsection 3.2.3 we present our numerical results and in subsection 3.2.4 summarize our findings.

3.2.1 Perturbation equations revisited

To see more clearly some of the effects of truncation on topographic instability it is essential that we rederive the equation for the total perturbation, ψ' , as well as separate equations governing its mean zonal and eddy parts, $\bar{\psi}'$ and ψ'^* , respectively.

a. ψ' -equation

Using (4)-(6) in (13) we immediately arrive at

$$\begin{aligned} \partial_t \Delta \psi' + u_s (\Delta + K_s^2) \partial_x \psi' \\ + J[\bar{\psi}_s, (\Delta + K_\alpha^2) \psi'] + J[\psi', (F_o/H) h_s] = 0 \end{aligned} \quad (39)$$

where $\bar{\psi}_s$ and h_s are the wavy parts of $\bar{\psi}$ and h , respectively, i.e.

$$(\bar{\psi}_s, h_s) = (\bar{\psi}_\alpha, h_\alpha) \cdot 2 \sin(2\pi\mu x/L) \sin(\pi\eta y/D) \quad (40)$$

with $\mu = m_\alpha$ and $\eta = n_\alpha$. The third and fourth terms in (39) represent the interaction of the perturbation with the equilibrium wave and the topography, respectively.

In preparation for what is to follow, we partition the wavy part of the disturbance into a component on the same scale as the topography (denoted by $\psi'_s + \psi'_c$) and a part with the same zonal but different (and arbitrary) meridional structure (denoted by $R'_s + R'_c$), i.e.,

$$\psi'^* = (\psi'_s + \psi'_c) + (R'_s + R'_c) \quad \text{where} \quad (41)$$

$$\psi'_s = \psi'_s{}^\eta \cdot F_s^\eta \quad , \quad \psi'_c = \psi'_c{}^\eta \cdot F_c^\eta \quad , \quad R'_s = \sum_{n \neq \eta} \psi_s^n \cdot F_s^n \quad , \quad R'_c = \sum_{n \neq \eta} \psi_c^n \cdot F_c^n$$

$$\text{with} \quad F_s^\eta = 2 \sin(kx) \sin(l_\eta y) \quad , \quad F_c^\eta = 2 \cos(kx) \sin(l_\eta y)$$

$k = 2\pi\mu/L$ and $l_\eta = \pi\eta/D$. It is important to understand that we are ignoring all components in the perturbation with a zonal wavenumber other than that of the topographic forcing. Qualitatively speaking, the major conclusions contained in this study are independent of this assumption (as will be demonstrated).

b. $\bar{\psi}'$ -equation

Using (40)-(41) in (15) leads to the following equation which governs $\bar{u}' = -\partial_y \bar{\psi}'$,

$$\begin{aligned} \partial_t \bar{u}' = & -\partial_y (\bar{u}_s \partial_x R'_c - \bar{v}_s \partial_y R'_c) \\ & + (f_0/H) \cdot \overline{h \partial_x \psi'_c} + (f_0/H) \cdot \overline{h \partial_x R'_c} \end{aligned} \quad (42)$$

where $(\bar{u}_s, \bar{v}_s) = (-\partial_y \bar{\psi}_s, \partial_x \bar{\psi}_s)$. Integrating (42) meridionally yields

$$d_t \langle u' \rangle = (f_0/H) \cdot \langle h \partial_x \psi'_c \rangle \quad (43)$$

The first term on the right-hand side of (42), involving R'_c only, represents the interaction between the equilibrium flow and the disturbance, through the convergence of Reynolds stresses. The last two terms involve the interaction between the topography and the perturbation, via form drag. Note that both the on-scale (ψ'_c) and off-scale (R'_c) parts of the perturbation are operative here. From (43) it can be seen that only the perturbation component on the scale of, and 90° out of phase with, the forcing affects the tendency of the channel-averaged disturbance zonal momentum.

c. ψ'^x -equation

Substituting (41) in (39), multiplying by F_s^η and integrating over the channel yields an equation for $\partial_t \psi'_s$.

$$K_\eta^2 \langle F_s^\eta \partial_t \psi'_s \rangle = u_s (K_s^2 - K_\eta^2) \langle F_s^\eta \partial_x \psi'_c \rangle \quad (44)$$

where $K_\eta^2 = k^2 + l_\eta^2$ is the two-dimensional wavenumber of the topography. A similar procedure gives an evolution equation for $\partial_t \psi'_c$.

$$\begin{aligned}
K_{\eta}^2 \langle F_c^{\eta} \cdot \partial_t \psi' \rangle &= u_s (K_s^2 - K_{\eta}^2) \langle F_c^{\eta} \cdot \partial_x \psi' \rangle \\
&- \langle F_c^{\eta} \cdot \bar{v}_s (\partial_{yy}^2 + K_{\eta}^2) \bar{u}' \rangle + (f_o/H) \langle F_c^{\eta} \cdot \bar{u}' \partial_x h_s \rangle
\end{aligned}
\tag{45}$$

Finally, to close the system we need equations for $\partial_t R'_s$ and $\partial_t R'_c$. These are acquired by substituting (41) into (39), multiplying by F_s^{η} and F_c^{η} , respectively, and channel-averaging, with the result that, $\forall n \neq \eta$,

$$K_n^2 \langle F_s^n \cdot \partial_t R'_s \rangle = u_s (K_s^2 - K_n^2) \langle F_s^n \cdot \partial_x R'_s \rangle
\tag{46a}$$

and

$$\begin{aligned}
K_n^2 \langle F_c^n \cdot \partial_t R'_c \rangle &= u_s (K_s^2 - K_n^2) \langle F_c^n \cdot \partial_x R'_c \rangle \\
&- \langle F_c^n \cdot \bar{v}_s (\partial_{yy}^2 + K_n^2) \bar{u}' \rangle + (f_o/H) \langle F_c^n \cdot \bar{u}' \partial_x h_s \rangle
\end{aligned}
\tag{46b}$$

3.2.2 An analytical solution

To proceed analytically we need to make some simplifying assumption. An ad hoc assumption, often used in the past, is to neglect all but the on-scale component in the disturbance wavy structure. This facilitates analytical progress but by ignoring modes (e.g. R'_s and R'_c) which, a priori, are not known to be unimportant leads to a rather weak set of conclusions. Nevertheless we will continue here with this assumption, for the time being, in order to derive explicitly the analytic results which we compare to our numerical ones in subsection 3.2.3. Mathematically speaking, this ad hoc assumption allows us to ignore (46) and the first term on the right-hand side of (42). From the latter we then get,

$$\overline{u'}(y, t) = \hat{u}(t) \cdot 2 \sin^2(l_\eta y) \quad (47)$$

where $d_t \hat{u} = - (f_0 h_\alpha / H) k \cdot \psi_c^\eta$

Differentiating (45) with respect to time and then substituting (44) and (47) gives an equation for the out-of-phase spectral coefficient by itself

$$\left[d_{tt}^2 + f \right] \cdot \psi_c^\eta = 0 \quad \text{with } f = \kappa^2 + \bar{I}$$

where $\kappa = k \cdot (u_s - \beta / K_\eta^2)$ (48)

and $\bar{I} = \frac{k^2}{2K_\eta^2} \left[(3K_s^2 - 4l_\eta^2)(K_s^2 - K_\eta^2) \right] \cdot \bar{\psi}^2$

Assuming solutions proportional to $\exp(-i\omega t)$ it follows that exponentially growing perturbations [i.e., $\omega_I = \text{Im}(\omega) > 0$] are only possible if \bar{I} is negative. This instability criterion presents two possibilities. If the flow is superresonant ($K_s < K_\eta$), instability is possible only if $l_\eta < \sqrt{3}k$. On the other hand, if the flow is subresonant ($K_s > K_\eta$), growing perturbations exist only if $l_\eta > \sqrt{3}k$. In other words, in this model unstable wide waves exist only in a superresonant regime while unstable narrow waves exist in subresonant regimes. Note also that growing perturbations are necessarily stationary [i.e., $\omega_R = \text{Re}(\omega) = 0$].

These instability conditions for form drag instability have previously been obtained by Rambaldi et al (1985). Also, in his study on nearly resonant topographic waves Pedlosky (1981) derived these conditions under the assumption of weak forcing.

The problem with this approach is that there is no proper rationale for neglecting the components we did. Substituting (47) into (46b) shows that the second and third terms on the right-hand side of the latter are non-zero if $n = 3\eta$, and as such force the eddy component which has a meridional wavenumber of 3η . This mode, which has been ignored in the analysis up till now, has a non-zero projection on $\partial_z \bar{u}'$ [see (42)], implying that \bar{u}' defined by (47) should be corrected before we embrace wholeheartedly the conclusions of the previous paragraphs. For this, and other reasons, we now turn to a numerical approach which treats the case for which R'_C (and R'_S) are in general non-zero

3 2 3 Numerical results

To begin we will briefly outline the numerical techniques we have employed to solve the disturbance equations. Consider expanding \bar{u}' in an infinite sine-series, i.e.

$$\bar{u}'(y, t) = \sum_{n=1}^{\infty} u'_z{}^n F_z^n \quad \text{where} \quad F_z^n = \sqrt{2} \sin(l_n y) \quad (49)$$

Equations for the (time-dependent) spectral coefficients in (49) can be obtained by multiplying (42) by F_z^n , and then averaging with respect to y . On the other hand, the spectral equations for the eddy coefficients are given by (44)-(46), after direct substitution of the various spectral series

Assuming solutions proportional to $\exp(-i\omega t)$ the problem becomes one of solving an infinite-order matrix eigenvalue system for which we may obtain approximate solutions by truncating the spectral series. In

this connection we need to define two new truncation numbers, NZ and NW , both of which will be considered variable. These are the number of mean zonal and wavy components kept in (49) and (41), respectively. This truncation leads to $NZ + 2NW$ eigenvalues and $NZ + 2NW$ corresponding eigenvectors, which we calculated numerically as before.

In this particular study we choose $(\mu, \eta) = (1, 1)$ so that the topography has one oscillation in the zonal direction and half an oscillation in the meridional direction. Recall that, parametrically speaking, the stability of the steady flow associated with this forcing was studied in detail in subsection 3.1.4a. For the channel parameters considered here we have that $l_\eta \approx 3.5k (> \sqrt{3}k)$, which according to the analytic solution suggests that only subresonant unstable perturbations exist. Our numerical analysis will make it possible to check this analytical result.

One minor complication that the addition of the off-scale components in the perturbation structures entails is that instabilities may exist which are non-topographic, in the sense that they do not crucially depend on a form drag mechanism. This is not to say that the topography does not interact with the perturbation, it simply means that it does not force, through the action of form drag, a perturbation zonal flow with a non-zero channel average [see (43)]. These instabilities, which are not of interest here, will only serve to clutter the analysis. Conveniently, though, the stability matrix A can be split into two independent matrices, denoted A_R and A_T , which can be associated with non-topographic and topographic perturbations, respectively. To see this we note that in this channel model an interaction between the basic state wave, (μ, η) , a perturbation mean zonal component, $(0, p)$, and a

3

perturbation eddy component, (μ, q) , is only possible if $\eta + p + q$ is odd. [Where (m, n) denotes the zonal and meridional wavenumbers, m and n , respectively.] This implies, since $\eta = 1$, that the stability matrix A decouples into two submatrices, A_T and A_R : the first involving perturbations with mean zonal and eddy components that are both odd [i.e., $(0, n)$ and (μ, n) , with n odd for both], and the second involves perturbations with mean zonal and eddy components that are both even (n even in both). This decoupling of the matrix A into two submatrices can also be deduced from a consideration of the y -symmetries contained in the perturbation equations, as done in Appendix B. Since the structures related to A_T have, in general, a mean zonal part with a non-zero meridional average [i.e., since they have mean zonal components, $(0, n)$, with n odd] their existence is crucially dependent on form drag. In contrast, the perturbation structures associated with A_R do not depend on a form drag mechanism (i.e., since they have no mean zonal components with n odd) but can arise, rather, from the convergence of Reynolds stresses. Hereafter we will be concerned with A_T only.

We will now present a numerical analysis wherein we emphasize the effects of truncation on topographic instability. We will consider separately the instabilities residing near and far away, in parameter space, from linear resonance

a. Instability close to linear resonance

All the growing near-resonant perturbations encountered here were stationary. In addition, one and only one unstable mode was ever found for any given parameter setting. In Fig. 16, the e -folding time is plotted against the mean zonal wind for various combinations of trun-

cation numbers NZ and NW (from here on, we will use the notation $TR = [NZ, NW]$ to indicate the truncation). The topographic amplitude is fixed at a value of $2h_\alpha/H = 0.2$. Note also that linear resonance occurs when $u_s \approx 24.3 \text{ m s}^{-1}$.

In Fig. 16a, NZ is fixed at a value of 41 and NW is allowed to vary from 1 to 41. The left-most curve ($TR = [41, 1]$) is that which would be obtained if one used the analytic solution from subsection 3.2.2. In this case, as expected, instability is confined to the *subresonant* side of the resonant wind line. However, as the number of meridional wavenumbers in the eddy expansion is increased the instability moves to the *superresonant* side. Curves corresponding to $NW > 41$ have not been drafted since they are virtually coincident with the $NW = 41$ curve. These results indicate that the components ignored in the analytical model are crucial, at least from the point of view of determining where topographic instability lies in parameter space.

Using the right-most curve in Fig. 16a ($TR = [41, 41]$) as our control curve we would like to determine the least number of modes (mean zonal and eddy) required to accurately reproduce it. In Fig. 16b, NZ is set to a value of 9 and, as before, NW is allowed to vary. Again the e-folding curves move to the superresonant side as NW is increased (interestingly, when $TR = [9, 7]$ the instability disappears altogether). Further, when $TR = [9, 9]$ there is no appreciable difference from the control curve. In fact, when $TR = [1, 1]$ the control curve is still extremely well represented, as can be seen by comparing the latter and the dashed curve adjacent to it in Fig 16a. We conclude, in short, that to get a reasonably true picture of this near-resonant topographic instability we need only include the (0,1) and (1,1) components in the

perturbation structure. In addition, if more waves are included care should be taken to include as many meridional wavenumbers in the eddy expansion as in the mean zonal one (i.e., $NW = NZ$).

To conclude this subsection we bring to the attention of the reader the dashed curve in Fig. 16b. This curve was obtained using perturbations composed of 9 meridional wavenumbers in the mean zonal and eddy expansions (i.e. $TR = [9,9]$) and 9 zonal wavenumbers. The additional zonal wavenumbers are seen to have a slight stabilizing effect on the instability, which becomes more pronounced away from linear resonance.

b Instability away from linear resonance

In addition to the instabilities described above the numerical analysis revealed growing perturbations to basic flows far removed from linear resonance. Unlike the previous instabilities these, in general, require more components to be resolved and have smaller growth rates. Moreover, they are travelling (i.e., $\omega_r \neq 0$) rather than stationary. We will see that these growing disturbances have the interesting property of drawing energy from the basic state through the form drag mechanism and/or the convergence of Reynolds stresses, depending on their phase relationship with the equilibrium wave.

Fig. 17a presents e -folding curves as a function of the orographic amplitude and constant mean zonal wind for $TR = [41,41]$. On the super-resonant side we find the region of stationary near-resonant instability discussed earlier. New here are the two adjacent regions of instability lying between approximately 10 m s^{-1} and 14 m s^{-1} . The growing perturbations in these regions are dominated by the (0,1) and (0,3) mean zonal components and the (1,1) and (1,3) eddy modes. Motiv-

ated by this fact we now consider a truncated system involving these modes alone.

Fig. 17b shows the e-folding curves when $TR = [3,3]$. Notice that the superresonant curves are virtually identical to the corresponding ones of Fig. 17a. On the other hand, the subresonant curves of Fig. 17a are less well represented in this low-order system. In particular, the two subresonant regions have been replaced by a single smaller one. Nevertheless, the agreement is close enough to warrant further investigation with this severely truncated model.

1) THE FREQUENCY

For this low-order system it is a relatively simple matter to obtain an explicit expression for the frequency ω . Denoting the components of the system as $\theta = (0,1)$, $\phi = (0,3)$, $\beta = (1,1)$ and $\epsilon = (1,3)$, the frequency equation can be written

$$\omega^4 - b \cdot \omega^2 + c = 0 \quad (50)$$

$$\text{where } b = \omega_\beta^2 + \omega_\epsilon^2 + \frac{\Delta_\theta \Delta_\beta}{K_\theta^2 K_\beta^2} C_{\theta\beta}^2 + \frac{\Delta_\theta \Delta_\epsilon}{K_\theta^2 K_\epsilon^2} C_{\theta\epsilon}^2 + \frac{\Delta_\phi \Delta_\beta}{K_\phi^2 K_\beta^2} C_{\phi\beta}^2 + \frac{\Delta_\phi \Delta_\epsilon}{K_\phi^2 K_\epsilon^2} C_{\phi\epsilon}^2$$

$$\text{and } c = \omega_\beta^2 \omega_\epsilon^2 + \frac{\Delta_\theta \Delta_\beta}{K_\theta^2 K_\beta^2} C_{\theta\beta}^2 \omega_\epsilon^2 + \frac{\Delta_\theta \Delta_\epsilon}{K_\theta^2 K_\epsilon^2} C_{\theta\epsilon}^2 \omega_\beta^2 + \frac{\Delta_\phi \Delta_\beta}{K_\phi^2 K_\beta^2} C_{\phi\beta}^2 \omega_\epsilon^2 + \frac{\Delta_\phi \Delta_\epsilon}{K_\phi^2 K_\epsilon^2} C_{\phi\epsilon}^2 \omega_\beta^2$$

$$+ \frac{\Delta_\theta \Delta_\phi \Delta_\beta \Delta_\epsilon}{K_\theta^2 K_\phi^2 K_\beta^2 K_\epsilon^2} (C_{\theta\beta} C_{\phi\epsilon} - C_{\theta\epsilon} C_{\phi\beta})^2$$

Given $p = (m_p, n_p)$ and $q = (m_q, n_q)$ the various quantities in (50) are defined as follows:

$$K_p^2 = \left(\frac{2\pi m_p}{L}\right)^2 + \left(\frac{\pi n_p}{D}\right)^2, \quad \Delta_p = K_s^2 - K_p^2, \quad (51)$$

$$\omega_p = \left(\frac{2\pi m_p}{L}\right) \frac{\beta \cdot \Delta_p}{K_s^2 K_p^2} \quad \text{and} \quad C_{pq} = \hat{C}_{pq} \cdot \tilde{\psi}_\alpha = - \hat{C}_{pq} \cdot (F_0 h_\alpha / H) / \Delta_\beta$$

where \hat{C}_{pq} is the interaction coefficient associated with the p and q components (see Appendix C) and $\tilde{\psi}_\alpha$ is the amplitude of the basic-wave.

Before discussing the subresonant instability we will consider the behaviour of ω near linear resonance. Under near resonant conditions: $\Delta_\beta \approx 0$, $\Delta_\theta > 0$, $\Delta_\phi < 0$ and $\Delta_\epsilon < 0$. If the flow is subresonant, $\Delta_\beta > 0$, and if it is superresonant, $\Delta_\beta < 0$. It is shown in Appendix C that under these conditions the frequency can be approximated by

$$\omega^2 \approx \frac{\Delta_\theta \Delta_\beta}{K_\theta^2 K_\beta^2} (C_{\theta\beta} C_{\phi\epsilon} - C_{\theta\epsilon} C_{\phi\beta})^2 / C_{\phi\epsilon}^2 \quad (52)$$

which, in turn, can be written more simply as

$$\omega^2 \approx (128/135)^2 \frac{\Delta_\theta \Delta_\beta}{K_\theta^2 K_\beta^2} C_{\theta\beta}^2 \quad (53)$$

As expected we find that the near resonant instability is dominated by the $\theta = (0,1)$ and $\beta = (1,1)$ components, and is exclusively superresonant (since $\Delta_\theta \Delta_\beta < 0$ in that case). The $\phi = (0,3)$ and $\epsilon = (1,3)$ components are found to have a slight stabilizing effect [as measured by the numerical factor in (53)]:

It is useful to compare (53) with the equation one obtains by ignoring the ϵ component altogether (as in Rambaldi et al., 1985). Returning to (50) and setting $\omega_\epsilon = C_{\theta\epsilon} = C_{\phi\epsilon} = 0$ we find that under near resonant conditions

$$\omega^2 \approx \frac{\Delta_\beta}{K_\beta^2} \left[\frac{\Delta_\theta}{K_\theta^2} \cdot C_{\theta\beta}^2 + \frac{\Delta_\phi}{K_\phi^2} \cdot C_{\phi\beta}^2 \right] \quad (54)$$

In Appendix C it is shown that $|\Delta_\phi| C_{\phi\beta}^2 K_\phi^{-2} \gg |\Delta_\theta| C_{\theta\beta}^2 K_\theta^{-2}$ (see C.10) so that (54) can be further simplified, i.e.

$$\omega^2 \approx \frac{\Delta_\phi \Delta_\beta}{K_\phi^2 K_\beta^2} \cdot C_{\phi\beta}^2 \quad (55)$$

In this case we get the erroneous results that near resonant instability is dominated by the $\phi = (0,3)$ and $\beta = (1,1)$ components, and that it is exclusively subresonant (i.e. $\Delta_\phi \Delta_\beta < 0$).

Returning to the subresonant instability we will now use (50) to obtain an expression for the neutral curve, valid at low basic-wave amplitude. To begin, we observe that the curve defined by $b^2 - 4c = 0$ separates, in parameter space, unstable travelling perturbations from growing-stationary or neutral-travelling perturbations. In the small amplitude limit (i.e., $\tilde{\psi}_\alpha \rightarrow 0$) this curve can be approximated by

$$(\omega_\beta^2 - \omega_\epsilon^2) + 2 \cdot \left[\frac{\Delta_\theta \Delta_\beta}{K_\theta^2 K_\beta^2} \cdot \hat{C}_{\theta\beta}^2 + \frac{\Delta_\phi \Delta_\beta}{K_\phi^2 K_\beta^2} \cdot \hat{C}_{\phi\beta}^2 - \frac{\Delta_\theta \Delta_\epsilon}{K_\theta^2 K_\epsilon^2} \cdot \hat{C}_{\theta\epsilon}^2 - \frac{\Delta_\phi \Delta_\epsilon}{K_\phi^2 K_\epsilon^2} \cdot \hat{C}_{\phi\epsilon}^2 \right] \cdot \tilde{\psi}_\alpha^2 \approx 0 \quad (56)$$

This equation was used to obtain the dashed curve shown in Fig. 17b. Notice, in particular, that the neutral curve intersects the u_s axis when

$$\omega_\beta + \omega_\epsilon = 0 \quad (57)$$

which in the case at hand occurs at $u_s \approx 13.6 \text{ m s}^{-1}$.

Before describing, more precisely, the nature of this subresonant instability we refer the reader to Vallis (1985) for a very complete analysis of a truncated system similar to this, but defined on a doubly periodic domain.

2) THE STRUCTURE

To help understand the nature of the mechanism(s) underlying the subresonant instability we present a typical structure in Fig. 18. The four panels show the structure at various times during its period of oscillation (the exponential growth has been suppressed and the dashed lines indicate negative values). The arrow at the bottom of each perturbation structure indicates the location of the basic state trough (which also corresponds to the position of the topographic peak). Also shown are the profiles of form drag, Reynolds stress and mean zonal momentum at each of the presentation times [the first two quantities are defined in (42)].

This sequence can be interpreted as representing a wave on the scale of the forcing [i.e., (1,1)] which is travelling westward and, due to the presence of a weak (1,3) mode, meandering meridionally. In Fig. 18b the (1,1) wave is nearly 90° out of phase with the topography. At this particular time we would expect a form drag mechanism to be largely responsible for the exponential growth of the structure. (Notice that the form drag profile is at a maximum over the sequence.) In contrast, in Fig. 18d this wave is almost in phase with the topography implying that the form drag mechanism is no longer operative (the form drag profile on the right verifies this). At this time the (1,3) component dominates the tendency of the mean zonal flow through the con-

vergence of Reynolds stresses. (Notice the significant phase line tilt in Fig. 18d.) It is apparent that the growth of this disturbance is dependent not only on form drag but also on the Reynolds stresses, which help maintain the exponential growth despite the travelling nature of the perturbation.

The perturbation just described arose out of a truncated system. When more wavenumbers, in both the meridional and zonal directions, are used to define the structure this instability remains but is stabilized somewhat by the presence of higher harmonics. Consider Fig. 19 which shows the perturbation when 13 zonal wavenumbers and 13 meridional wavenumbers are used to define the structure (for a total of 351 components). Comparing Fig. 18 and Fig. 19 we conclude that although the latter contains more detail it is qualitatively very similar to the structure obtained using the severely truncated system.

3.2.4 Discussion

A quasi-geostrophic β -plane channel model with sinusoidal topography has been used to investigate topographic instability. The equilibrium flow was composed of a constant zonal flow plus one forced wave having the gravest possible zonal and meridional scales permitted by the channel [i.e. $(\mu, \eta) = (1, 1)$, where μ and η are the zonal and meridional wavenumbers, respectively]. Linear perturbations to the equilibrium flow were chosen having a single zonal wavenumber, that of the forcing but many harmonics in y , including that of the topography. The mean zonal part of the perturbation structure contained as many components as the wavy part. A numerical stability analysis, involving the solution of a standard matrix eigenvalue problem, was then performed.

It was found that topographically unstable flows reside in parameter space both near and far from linear resonance. In the former region the flows were superresonant and the instability was stationary. In contrast, the flows far from linear resonance were subresonant and the instability was travelling. The travelling instability was found to depend crucially on the combined effects of form drag and Reynolds stresses. The stationary instability, on the other hand, persisted without the presence of Reynolds stresses.

One of the objectives of this investigation was to study the effects of truncation on topographic instability. In particular, we were interested in obtaining the minimum systems (i.e., the least number of components in the disturbance expansions) required to reasonably resolve the various instabilities. In this connection it was discovered that the near-superresonant instability could be resolved adequately with only two components in the perturbation structure. Specifically, only the mean zonal (0,1) and eddy (1,1) modes were required. The subresonant instability needed the (0,3) and (1,3) modes, in addition to, the (0,1) and (1,1) components to be resolved. Finally, it was also found, in both cases, that when more components were used to define the disturbance structure that care had to be taken to allow as much meridional structure in the mean zonal part as in the wavy part.

As a complete departure from the present discussion we now turn to the next section wherein we consider the local instability of a particular weakly non-parallel equilibrium flow. To help put the upcoming discussion into some context we return to Fig. 15. The disturbance illustrated in this figure was interpreted in Section 3.1 as representing a westward propagating structure which undergoes periods of

enhanced growth as it passes through favourable regions associated with the basic flow. A similiar, but much more complex sort of behaviour has been described and analyzed by Frederiksen, who in a series of papers (see Frederiksen, 1983 and references therein) has attempted to shed some light on the problem of regional cyclogenesis in the atmosphere. Although our model is much too simple to explain the geographical distribution of cyclone occurrence in the atmosphere (i.e., storm tracks) it may be useful in helping to resolve some of the theoretical issues one encounters when trying to understand the results of stability calculations such as those described in Frederiksen (1983).

3.3 Local instability of weakly non-parallel flow

To date there have been several papers published dealing with the barotropic instability of weakly non-parallel atmospheric flow. Tupaz et al. (1978), for instance, used the barotropic vorticity equation with Rayleigh friction and forcing to examine the effects of the downstream variation of a slowly varying Bickley jet on its instability properties. The linear instability characteristics of the jet were obtained through long-term integrations on an open β -plane channel.

More recently, Merkin and Balgovic (1983) used the barotropic vorticity equation with a localized vorticity source and Rayleigh friction to study the linear instability of a weakly non-parallel zonal flow. The basic flow was obtained analytically assuming weak localized forcing, weak frictional effects and that certain resonance conditions were met. Numerical integrations, performed on an infinite β -plane channel, revealed the existence of unstable localized wavepackets whose characteristics depend on the maximum shear and the zonal length-scale of the basic flow.

In the present study we will utilize our simpler model (than the aforementioned) to address the question of the local growth of linear perturbations. As discussed in Chapter 2 our basic flow represents an exact finite-amplitude solution to the barotropic vorticity equation without dissipation or inhomogeneous forcing. In what follows the numerically determined fastest-growing eigenmode to a slowly varying basic flow, of this sort, is analyzed and then compared with the corresponding approximate solution acquired using the WKB approximation. In this way we hope to shed some light on certain aspects of the local instability of two-dimensional flow.

By way of review we recall that in Section 3.1 a detailed stability analysis was performed on $\bar{\psi}$ [see (6)] for two different cases, denoted E11 and E21. [These cases correspond to $(m_\alpha, n_\alpha) = (1,1)$ and $(2,1)$, respectively.] In both cases, $\bar{\psi}$ was stable or unstable depending on the particular values of h_α and μ_s . When $\bar{\psi}$ was unstable then either a resonant interaction, shear or topographic mechanism, was responsible. For example, in a region of parameter space near superresonance $\bar{\psi}$ was found to be unstable to perturbations of the topographic variety. In this case the disturbances were stationary and resonantly amplified. The structures themselves had a large eddy component on the scale of the topography and a substantial mean zonal component, generated through an interaction between the free-wave and the topography via form drag.

Mukougawa and Hirota (1986a) (hereinafter referred to as MH) considered the cases E11, E31 and E12. By comparing the three cases they concluded that the instability properties of topographically forced waves are completely different according to whether the meridional wavenumber (n_α) of the topography is even or odd. In particular, they came to the conclusion that when n_α is even topographic instability does not exist. In the next subsection we will demonstrate, by considering all the growing modes, not just the fastest-growing ones as in MH, that topographic instability does indeed exist when the meridional wavenumber is even. Following this brief discussion we will consider in detail the behaviour of a strongly modulated growing eigenmode with the aim of contributing to our understanding of the local instability characteristics of inhomogeneous flow.

3.3.1 Topographic instability

In this and the following subsection we will consider the linear stability of the steady-state, $\bar{\psi}$, when $(m_\alpha, n_\alpha) = (1, 2)$ (i.e. E12). In this case the topography, and hence the forced steady wave, has one complete oscillation in both the zonal and meridional directions. The fixed parameters in this study are as before except that $D = 5.56 \times 10^6$ m and $H = 8.43 \times 10^3$ m (corresponding to MH). For these channel dimensions the ratio of the basic-state x and y wavelengths (i.e. $L_x = L/m_\alpha$ and $L_y = 2D/n_\alpha$, respectively) is

$$\delta = L_y/L_x \approx 0.2. \quad (58)$$

The smallness of this parameter will enable us to develop, in subsection 3.3.2, a locally-parallel model with which to interpret some of our results.

In MH, curves of constant growth rate as a function of u_s and h_α (in our notation) for the fastest-growing perturbations to $\bar{\psi}$ are presented. The curves were obtained using 820 degrees of freedom ($TR = [M, N] = [20, 20]$) and as such can be regarded as being very reliable. Their numerical results, together with a discussion based on a severely truncated model, led MH to conclude that topographic instability does not exist when the meridional wavenumber of the topography is even. However, by considering all the growing modes, not just the fastest-growing ones as in MH, we have found that topographic instability does in fact exist in this case.

Consider Fig. 20 which is a plot of the growth rate curves for the slowest growing perturbation to $\bar{\psi}$ as a function of u_s and $h_o = 2 \cdot h_\alpha$. The growth rates in Fig. 20 have been nondimensionalized as in MH, specifically,

$$\hat{\omega}_i = (100/f_0) \cdot \omega_i \quad (59)$$

In this case a nondimensional growth rate (given by $\hat{\omega}_i$) of 1.0 corresponds to an e-folding time of 11.2 days. For the sake of economy a lower truncation (i.e. $TR = [10,10]$) than in MH was used to obtain these curves [We will consider the effects of truncation shortly.] By considering the frequencies and structures of these modes we have found that: (1) they are stationary (i.e. $\omega_r = \text{Re}(\omega) = 0$) and occur only for near superresonant basic flow and (2) the u' component of the structures have a non-zero channel average. As discussed earlier, the latter can only be the result of an interaction with the topography, that is, of a form drag mechanism.

The equilibrium flow and the growing perturbation associated with the point $u_s = 13 \text{ m s}^{-1}$ and $h_0 = 0.5 \text{ km}$ in Fig 20 are shown in Figs 21a, b, respectively. This structure is characteristic of all the other unstable structures connected with Fig. 20. Notice that the eddy part of the structure is on the scale of, and out of phase with, the topography and that there is a substantial mean zonal component. From these, and previous considerations we conclude that these modes depend crucially on a form drag mechanism and, as such, represent topographic instability. More to the point, we have found topographic instability to exist even though the meridional wavenumber of the topography is even.

To convince the reader that this instability is not an artifact of the truncation we present Table 1. This table shows the growth rate of the mode just described as a function of truncation, ($N = M$ and $NL = N + 2 \cdot N \cdot M$, is the number of degrees of freedom). As can be seen

the instability persists despite the stabilizing influence of the additional components. Admittedly, it is not clear from Table 1 that convergence in the frequency has been achieved but unfortunately further tests at higher resolutions were not possible because of computer memory constraints. It is somewhat consoling, however, that at these truncations the eigenfunctions were found to be well resolved. Note that the dashed curve in Fig. 20 is the neutral curve obtained using a severe truncation involving the (0,1) and (1,2) components alone. The accuracy at this truncation is of course poor, but the results are qualitatively correct.

It should be understood that the topographically unstable modes to this basic-state are in fact the least unstable of a number of unstable modes. For instance, the topographic mode to the basic-state of Fig. 21a has an e-folding time of approximately 4.8 days while the fastest-growing mode (which is non-topographic in origin) has an e-folding time of approximately 0.7 days. In the next subsection we will consider in detail one of these fastest-growing modes.

3.3.2 The fastest-growing perturbation

In the previous subsection it was demonstrated that an equilibrium flow resulting from flow over a meridionally *asymmetric* topography could be topographically unstable. As expected this instability resides in a region of parameter space near linear resonance where a strong feedback to the zonal flow is obtained. However, unlike the topographic instabilities previously discussed, involving a meridionally *symmetric* topography, it happens to be, for a given parameter setting, just one of several growing modes, most of which have much larger growth rates.

These other growing modes are non-topographic in origin, have relatively large growth rates and cover an extensive area of parameter space (see Fig. 12 of MH). For obvious reasons, then, an inspection of at least one of these other growing modes is in order. In part (a) we consider a representative growing mode of this type, both from a synoptic and an energetics point of view. In part (b) we use an analytical technique, based on WKB theory, to help interpret our results.

a. *Structure and energetics*

1) STRUCTURE

In MH the fastest-growing mode to a basic flow generated by a zonal wind of 17 m s^{-1} over a topography with an amplitude of 2 km is presented (Fig. 13a of MH). This mode has an e-folding time of approximately 1.5 days and, although it is not stated in MH, is stationary. In this study we will consider the fastest-growing mode when $u_s = 17 \text{ m s}^{-1}$ and $h_0 = 1 \text{ km}$ since the wind speeds associated with the equilibrium wave are more realistic. The basic-state streamfunction and zonal flow, in this case, are shown in Figs. 22a, b. The fastest-growing mode has a e-folding time of approximately 3.6 days, is stationary and has a structure as shown in Fig. 22c. We should mention that due to the symmetry of the basic flow the structure of the mode consists only of those zonal components, $(0, n)$, where n is even, and eddy components, (m, n) , where n is odd. We see that this mode has a very simple meridional structure, with most of its amplitude centered about $x = L/2$, with a bias towards the downstream side (i.e. eastward).

As can be seen, the fastest-growing perturbation on this non-zonal basic-state exhibits a structure whose amplitude is strongly modulated in the zonal direction. This is in contrast to the situation involving a zonally-uniform basic-state whose growing perturbations take the form of a single harmonic wave in x (multiplying some structure in y). Returning to Fig. 22c we note the presence of a zonal-wavenumber-1 modulation pattern which is roughly in phase with the \bar{u} field (see Fig. 22b). The peak in the envelope, near $x = L/2$, appears to be associated with the weak basic-state easterly jet situated at the center of the channel. As we will shortly see the instability mechanism responsible for the overall exponential growth of this mode is especially efficient around this easterly jet.

The zonal and meridional energy spectra, $E'(m)$ and $E'(n)$, respectively, corresponding to this growing mode are shown in Fig. 23. These normalized energy spectra are defined as follows

$$E'(m) = \sum_{n=1}^N K_{\beta}^2 \hat{\psi}_{\beta}^2 \quad \text{and} \quad E'(n) = \sum_{m=0}^M K_{\beta}^2 \hat{\psi}_{\beta}^2 \quad (60)$$

where $K_{\beta}^2 = (2\pi m/L)^2 + (\pi n/D)^2$

As before the subscript β is a shorthand notation for the ordered pair $\beta = (m, n)$. We note that the zonal energy spectrum peaks at $m = 3$. For zonal wavenumbers greater than three $E'(m)$ falls off rapidly indicating that the mode is well resolved, at least in the zonal direction. The meridional energy spectrum is a maximum at $n = 1$ and falls off significantly for meridional wavenumbers greater than five.

A total of 210 components (i.e. $TR = [10,10]$) were used to define the structure presented in Fig. 22c. The perturbation can, however, be accurately represented with a much smaller number of components. Consider, for example, Table 2 which shows the growth rate and frequency of this mode as a function of truncation. Table 2 reveals that: (1) the instability is very accurately resolved (at least in terms of $\hat{\omega}$) when $M \geq 3$ and $N \geq 5$, and (2) when $M \geq 3$ and $N = 3$ the real part of $\hat{\omega}$ is non-zero (albeit very small) and the growth rate is reduced (by about 25%). The only growing mode when $TR = (5,3)$ is shown in Fig. 24 (at $t = 0$).

We have seen, throughout this discussion, that the active region associated with this instability, is located near and somewhat downstream of $x = L/2$. In the next part we will attempt to identify the instability mechanism(s) responsible for this region of preferred growth.

2) ENERGETICS

The energy source for this exponentially growing disturbance is of course the basic-state. To see explicitly the conversion mechanism(s) behind the instability we need to obtain the perturbation energy equation. In a manner similar to Simmons et al. (1983) we will write the perturbation energy equation for this system in the form

$$d_t E' = d_t \left\langle \frac{|\nabla \psi'|^2}{2} \right\rangle = C_x + C_y + C_{xy}$$

$$\text{where } C_x = - \langle u'v' \cdot \partial_x \bar{v} \rangle, \quad C_y = - \langle u'v' \cdot \partial_y \bar{u} \rangle \quad (61)$$

$$\text{and } C_{xy} = - \langle (u'^2 - v'^2) \cdot \partial_x \bar{u} \rangle.$$

Here E' is the horizontally-integrated perturbation kinetic energy and C_x , C_y and C_{xy} are distinctively different conversion terms.

Written in this fashion (61) can be readily interpreted as a generalized form of the energy equation for a unidimensional basic-state. For unidimensional unstable flow, $C_{xy} = 0$ and either: (1) $C_x = 0$ if the basic flow is zonally-uniform or (2) $C_y = 0$ if it is meridionally-uniform. In either of these cases, perturbation energy growth is implied when the eddy momentum flux, $u'v'$, is on average in a direction opposite to the gradient of the basic-state velocity. When the basic flow is two-dimensional there is an additional, and less familiar conversion mechanism, expressed by C_{xy} . This term implies that there will be perturbation energy growth when the disturbance is mainly zonal ($u'^2 > v'^2$) in regions of diffluence ($\partial_x \bar{u} < 0$), and mainly meridional ($u'^2 < v'^2$) in regions of confluence ($\partial_x \bar{u} > 0$).

By considering the local contributions to each of the conversion terms a good idea of the mechanism(s) behind the local growth of a particular perturbation can be obtained. This sort of analysis was performed, for example, by Simmons et al. (1983) in their consideration of the linear stability of the 300 mb climatological mean January flow. In the following discussion the structure of the basic-state (see Figs. 22a, b) should be kept in mind.

In the top and bottom panels of Fig. 25 we have plotted the local contributions to $C_x + C_y$ and C_{xy} , respectively. With regards to C_x we point out that since the basic flow is nearly zonal (i.e., $|\partial_y \bar{u}| \gg |\partial_x \bar{v}|$) this conversion is relatively unimportant and can be ignored. Notice, first, that the local contribution to $C_x + C_y$ is a maximum near $x = L/2$. This reflects the fact that the large negative perturbation center near $x = L/2$ is tilted in a manner which will lead to a weakening of the basic-state easterly jet and so, by energy conservation, encourage its own growth.

The local contribution to C_{xy} is a maximum further downstream from $x = L/2$. The three positive areas centered along $y = D/2$ arise from meridional perturbation flow where the basic-state is confluent. On the other hand, those near the walls are connected with the zonal perturbation flow where the basic-state is diffluent. Comparing the two conversion fields we find that the $C_x + C_y$ field has a larger maximum but since this field is also more confined in space, its integrated value, at this time, is actually smaller than C_{xy} [i.e. $(C_x + C_y)/C_{xy} \approx 0.8$].

Figures 25a, b demonstrate that the $C_x + C_y$ conversion, principally involving the transfer of basic-state zonal momentum (since $|C_x| \ll |C_y|$), is correlated with the perturbation amplitude maximum centered at $x = L/2$ (see Fig. 22c). The C_{xy} conversion, on the other hand, is associated with the considerable perturbation amplitude found downstream from $x = L/2$. As we have seen, this conversion depends crucially on the existence of regions of confluence and diffuence in the basic-state.

In this subsection we have considered, in a somewhat descriptive manner, the structure and energetics of the fastest-growing linear per-

turbation to a large amplitude, nearly-zonal steady state. We found, in particular, that the instability was in a large part maintained by the transfer of zonal momentum into an easterly jet, through the action of Reynolds stresses (i.e. $u'v'$). Downstream from the location where this transfer is largest the disturbance is found to undergo further enhancement of its local growth due the transfer of energy out of regions where the basic-state is either confluent or diffluent.

The fastest-growing mode to the basic flow of Fig. 22a was obtained numerically by solving a matrix eigenvalue problem. In the next part we will use WKB theory to obtain an approximate analytic solution which we compare with the numerical one. This method is based on the assumptions that the basic-state is slowly varying in x (i.e. $\delta' \ll 1$) and that there exists a spatial scale separation between the basic-state and the perturbation. Although neither of these conditions are very strongly satisfied in this case (recall that $\delta \approx 0.2$) we will show that it is still possible to get qualitative agreement between the analytical and numerical solutions.

b. WKB analysis

In this part we will exploit the fact that the basic flow is nearly zonal (i.e., $\delta = L_y/L_x \approx 0.2$) to find an approximate analytic representation for its fastest-growing perturbation. In (1) we use WKB theory to derive a simplified perturbation equation for our system. In (2) we solve this equation after making some suitable simplifying assumptions. In this analysis we make extensive use of some techniques developed by Pierrehumbert (1984) to study the stability of slowly varying flows.

1) WKB THEORY

To begin we will rewrite the linearized perturbation equation as

$$\left[\partial_t - (\partial_y \bar{\psi}) \cdot \partial_x \right] \cdot \Delta \psi' - K_s^2 \cdot (\partial_y \bar{\psi}) \cdot \partial_x \psi' \\ = - (\partial_x \bar{\psi}) \cdot \partial_y (\Delta + K_s^2) \psi' \quad (62)$$

Here the various variables and constants have been nondimensionalized according to $t = (U/D) \cdot t^*$, $(x, y) = (x, y)^*/D$, $(\bar{\psi}, \psi') = (\bar{\psi}, \psi')^*/DU$ and $K_s = D \cdot K_s^*$, where U is some characteristic velocity, D is the channel width and an asterisk denotes a dimensional quantity. To express the fact that the basic flow is a slowly varying function of x we will introduce the slow x -scale, $X = \delta x$, where δ is some small parameter, say $\delta = L_y/L_x$. In terms of X , and expanded in powers of the small parameter δ , the coefficients of (62) can be written

$$\partial_y \bar{\psi} = \bar{u}(X, y) = \bar{u}_0(X, y) + \delta \cdot \bar{u}_1(X, y) + \dots \quad (63)$$

and $\partial_x \bar{\psi} = \delta \partial_X \bar{\psi} = \delta \cdot \bar{v}(X, y) + \dots$

Since the coefficients of (62) are slowly varying in x we will, in the spirit of the WKB approximation, assume a solution of the form

$$\psi' = \Phi(X, y) \cdot \exp(i\theta(x, t)) \quad (64)$$

where the frequency ω and wavenumber k are defined to be the derivatives of the phase function $\theta(x, t)$:

$$\partial_t \theta(x, t) = -\omega \quad \text{and} \quad \partial_x \theta(x, t) = k(X) \quad (64)'$$

The frequency and wavenumber are related by a local dispersion relationship, yet to be determined. It is important to realize that the phase function $\theta(x,t)$ (which is in general complex) describes the fast variation while its x -derivative is assumed to be slowly varying [i.e. $\partial_x \theta(x,t) = k(X)$]. For a solution of this form the x -derivatives in (62) become

$$\partial_x \psi' = (ik\Phi + \delta \partial_X \Phi) \cdot \exp(i\theta) \quad (65a)$$

$$\partial_{xx}^2 \psi' = \left[-k^2 \Phi + i\delta (\Phi \partial_X k + 2k \partial_X \Phi) + O(\delta^2) \right] \cdot \exp(i\theta) \quad (65b)$$

$$\text{and } \partial_{xxx}^3 \psi' = \left[-ik^3 \Phi - 3\delta k (\Phi \partial_X k + k \partial_X \Phi) + O(\delta^2) \right] \cdot \exp(i\theta) \quad (65c)$$

The equation upon which the remainder of this discussion is based is obtained by substituting (63)-(65) along with

$$\Phi(X,y) = \Phi_0(X,y) + \delta \cdot \Phi_1(X,y) + \dots \quad (66)$$

into (62) and collecting all the $O(1)$ terms, i.e.

$$\left[\bar{u}_0(X,y) - \frac{\omega}{k(X)} \right] \left[\partial_{yy}^2 - k^2(X) \right] \cdot \Phi_0 + K_s^2 \cdot \bar{u}_0(X,y) \cdot \Phi_0 = 0 \quad (67)$$

With the appropriate boundary conditions (67) constitutes an eigenvalue problem which for a given ω determines the eigenvalue $k(X)$ and the eigenfunction $\Phi_0(X,y)$. The latter can be written as the product $A(X) \cdot \phi(y;X)$ where $\phi(y;X)$ comes directly out of (67) and depends only parametrically on X . The amplitude function, $A(X)$, is determined by the amplitude equation which results at the next level of approximation after the imposition of a solvability condition on the $O(\delta)$ perturbation equation. As demonstrated by Saric and Nayfeh (1975), in their study of

weakly non-parallel boundary layer flows, $A(X)$ represents an $O(\delta)$ correction to the eigenvalue $k(X)$. Using this fact, and (64), the perturbation, to first approximation, can be explicitly written in the form

$$\psi' = \phi(y; X) \cdot \exp \left[i \int_{x_0}^x (k + \delta k_1) dx \right] \cdot \exp(-i\omega \cdot t), \quad (68)$$

where the $O(\delta)$ correction to k contains the effects of the x -derivatives of the basic flow and x_0 is a constant of integration. For parallel flow, ϕ is strictly a function of y , $k_1 = 0$ and k is a constant. On the other hand, when weak non-parallelism is allowed ϕ and k become functions of X and there develops an $O(\delta)$ correction to the latter. From here on we will ignore the presence of δk_1 and focus our attention instead on the x -variation of k induced by the non-parallelism.

At this time we will determine the $O(1)$ zonal flow, \bar{u}_0 . This can be done easily by recalling that by definition, $\bar{Q} = -K_S^2 \bar{\psi}$, from which it follows that

$$K_S^2 \bar{u} = \partial_y \bar{Q} = \beta - \partial_{yy}^2 \bar{u} + \delta^2 \partial_{XY}^2 \bar{v} + \partial_y h \quad (69)$$

In (69), $\beta = (D^2/U) \cdot \beta^*$ is the nondimensional β -parameter and $h = h_0 \cos(2\pi X) \sin(2\pi y)$ is the nondimensional topography whose amplitude is nondimensionalized according to $h_0 = (f_0 D/UH) \cdot h_0^*$. Substituting (63) into (69) and retaining only the $O(1)$ terms leads immediately to the equation governing \bar{u}_0 , i.e.,

$$K_S^2 \bar{u}_0 = \partial_y \bar{Q}_0 = \beta - \partial_{yy}^2 \bar{u}_0 + \partial_y h \quad (70)$$

Solving this equation for \bar{u}_0 yields the result

$$\bar{u}_0(X, y) = u_s - u_w(X) \cdot \cos(n_2 y) \quad \text{where } n_2 = 2\pi, \quad u_s = \beta/K_s^2 \quad (71)$$

$$\text{and } u_w(X) = u_0 \cdot \cos(2\pi X) \quad \text{with } u_0 = \left[\frac{n_2 \cdot h_0}{n_2^2 - K_s^2} \right]$$

To see the connection between the perturbation equation (67) and the more familiar Rayleigh-Kuo equation we note that the coefficient of the second term, given explicitly in (70), is equivalent to the corresponding one in the Rayleigh-Kuo equation if one sets $h = 0$. By analogy with barotropic instability, a necessary condition for instability when $h \neq 0$ is that the northward gradient of potential vorticity must vanish for some y within the channel. In other words, \bar{u}_0 must be equal to zero somewhere in the domain [from the left most relation in (70)]. It follows from (71) that this necessary condition for instability will only be satisfied when $|u_w| > u_s$.

For the sake of convenience we will replace \bar{u}_0 in (71) with \bar{u} . It has been found *a posteriori* that, qualitatively speaking, this substitution has little effect on our final conclusions. The zonal velocity, \bar{u} , is given by (71) with n_2 replaced with $n_2 \cdot (\delta^2 + 1)^{1/2}$ in the denominator of u_0 . This can be verified by using the identity $\partial_y \bar{v} = -\partial_x \bar{u}$ in (69). The actual \bar{u}^* flow is shown in Fig. 22b. We see that the condition for instability discussed in the previous paragraph (i.e., $\bar{u}^* = 0$) is often satisfied in this case.

We will now attempt to solve the eigenvalue problem posed in (67).

2) THE WKB SOLUTION

Equation (67) can not, in general, be solved explicitly unless some further approximation is made. For this reason we will approximate the meridional structure of the disturbance with just three meridional components, i e.;

$$\phi(y;X) = \phi_1(X) \cdot \sin(\pi y) + \phi_3(X) \cdot \sin(3\pi y) + \phi_5(X) \cdot \sin(5\pi y) \quad (72)$$

Recall that the numerically-determined fastest-growing mode described previously was dominated by these three y-components. In part (a) we will use (67) to obtain a dispersion relationship in the form: $F(k, u_w, \omega) = 0$. Thereafter, in part (b), we will find the particular ω for which there exists a solution, $k(X)$, which simultaneously satisfies the dispersion relationship and the boundary conditions which we have yet to define

(a) The dispersion relationship. Substituting (71) and (72) into (67) and collecting like terms leads to three homogeneous equations for the coefficients ϕ_1 , ϕ_3 and ϕ_5 [see (D.1) in Appendix D]. Setting the determinant of the coefficients to zero leads to the following,

$$\omega^3 + B(k, u_w) \cdot \omega^2 + C(k, u_w) \cdot \omega + D(k, u_w) = 0 \quad (73)$$

The coefficients of this cubic equation, which are rather complicated functions of k and u_w , can be found in Appendix D.

For the moment, we will simplify the present analysis by considering the dispersion relation obtained on the basis of retaining only the first two terms in (72) (i.e. using a two-term truncation). In

this special case the dispersion relation can be written very simply in the form

$$\frac{\omega}{k} = u_s - \frac{\beta(K_1^2 + K_3^2)}{2K_1K_3} - \frac{u_w(K_s^2 - K_1^2)}{4K_1^2} \quad (74)$$

$$\pm \frac{u_w}{4K_1K_3} \left\{ \left[2\left(\frac{\beta}{u_w}\right)(K_3^2 - K_1^2) + K_3^2(K_s^2 - K_1^2) \right]^2 + 4K_1^2K_3^2(K_s^2 - K_1^2)(K_s^2 - K_3^2) \right\}^{1/2}$$

where $K_1^2 = k^2 + n_1^2$, $K_3^2 = k^2 + n_3^2$, $n_1 = \pi$ and $n_3 = 3\pi$

This is an algebraic equation which relates frequency and wavenumber at each particular X (recall that u_w is a function of X). On the basis of (74) we make the following remarks:

□ When k is real, complex ω will only be possible if $K_1 < K_s < K_3$. This implies that for unstable flow

$$k^2 = (2\pi\delta m)^2 < K_s^2 - n_1^2 \quad (75)$$

If $u_s^* = 17.0 \text{ m s}^{-1}$ then $K_s = 5.43$ and, from (75), we must have $m < 3.58$ for instability to occur. This shortwave cutoff is consistent with our numerical results wherein zonal wavenumbers four and greater were stable (judging by their relatively small amplitudes, see Fig. 23).

□ Waves are more unstable in an easterly jet than in a westerly jet. This can be seen in (74) by noticing that ω depends not only on the magnitude but also the sign of β/u_w . This asymmetry is such that β (which is positive here) has a stabilizing influence on waves in wester-

lies and a destabilizing influence on waves in easterlies (Kuo, 1973). For the basic zonal flow under consideration our theoretical calculations [i.e., based on (74)] have shown that it appears to be locally stable for all x^* lying between $-L/4$ and $L/4$, where $\beta/u_w \geq 0$, and unstable through much of the rest of the domain, where $\beta/u_w < 0$. Again, this is qualitatively consistent with the numerical results.

□ By analogy with parallel flow instability we can, at each X in the domain, find the real wavenumber (if one exists), designated k_M , for which the imaginary part of ω is maximized, i.e.

$$\partial_{k_i} \omega_i = 0 \quad \text{at } k_M \quad (76)$$

An equation for k_M , in terms of the parameters of this problem, can be found in Appendix D (part b). For each k_M we can also calculate a growth rate, $\omega_i(k_M)$ and a phase speed, $c_r(k_M) = \omega_r(k_M)/k_M$. Consider Fig. 26 which is a plot of $m_M = (2\pi\delta)^{-1} \cdot k_M$, $\omega_i(k_M)$ and $c_r^*(k_M)$ as a function of X (we remind the reader that these curves pertain to the two-term system). The growth rate has been nondimensionalized according to (59). As expected these curves are symmetric about $X = 0.5$ where $u_w(X)$ has its largest negative value. At $X = 0.5$ the most-unstable and the shortest-unstable waves (not shown), have wavenumbers approximately equal to 2 and 3.2, respectively. Moving away from $X = 0.5$ the most-unstable and the shortest-unstable waves lengthen. At any value of X for which instability is found there is no long wave cutoff.

We will now return to the dispersion relation (73) which is based on the three-term system given by (72). Consider Fig. 27 which is a

plot of m_M^* , $\omega_i(k_M)$ and $c_r^*(k_M)$ as a function of X . Compared with Fig. 26 we note that the growth rates and phase speeds are significantly reduced. We also note that the most unstable wavenumbers are slightly larger than before and are now only a weak function of X . It appears then that the range of unstable wavenumbers, growth rates and phase speeds determined using (73) are compatible with those arising from the numerical model. More precisely speaking, when we compare the numerically-determined frequency (i.e., $\omega \approx 3.6 \cdot i$) with the local frequency, say at $X = 0.5$ (i.e., $\omega \approx 0.7 + 4.7 \cdot i$), we find a reasonable agreement. Notice, that in contrast to the numerical mode, which is stationary, the fastest-growing local mode has a non-zero phase speed. The local mode however is travelling so slowly that after one e-folding time its fastest zonal component traverses only one-fiftieth of its wavelength, and for this reason could be considered as approximately stationary.

As it is presently written, (73) is not well suited to our purposes since we are interested in specifying an X -independent ω in order to find $k(X)$. To remedy the situation we simply invert (73) to get k as a polynomial with X -dependent coefficient

$$\begin{aligned}
 & [a_9] \cdot k^9 + [a_8 \omega] \cdot k^8 + [a_7 + b_7 \omega^2] \cdot k^7 + [a_6 \omega + b_6 \omega^3] \cdot k^6 \\
 & + [a_5 + b_5 \omega^2] \cdot k^5 + [a_4 \omega + b_4 \omega^3] \cdot k^4 + [a_3 + b_3 \omega^2] \cdot k^3 \\
 & + [a_2 \omega + b_2 \omega^3] \cdot k^2 + [a_1 \omega^2] \cdot k + [a_0 \omega^3] = 0
 \end{aligned} \tag{77}$$

where the a_n 's and b_n 's are functions of u_w and can be found in Appendix D. This ninth-degree equation clearly yields, for a fixed ω ,

nine roots or branches of $k(X)$. Our final solution therefore should be written as the sum of nine independent solutions each corresponding to one of these branches. The particular ω to be used in (77) will be determined next, after we set the boundary conditions.

(b) Boundary conditions. To set the boundary conditions it will be useful to have in mind the nature of the unstable mode which we are trying to represent. Recalling Figs. 22b, c we observe that the envelope of the mode peaks near $x = L/2$ ($X = 0.5$), where the basic-state easterly jet is centered. Away from the peak the amplitude decays rapidly, especially in the upstream direction. Notice also, that long waves (in x) seem to prevail upstream of the peak and short waves downstream. This perturbation bears many of the identifying marks of a so-called unstable local mode as defined by Pierrehumbert (1984, hereinafter referred to as PH) in his study of baroclinic instability of slowly varying flows.

In PH it was established, numerically, that flows with localized baroclinicity can support two distinct types of unstable modes, referred to as *local* and *global*. Local modes have peak amplitude downstream of the point of maximum baroclinicity, decay to zero exponentially, both upstream and downstream from the peak, and do not require periodic boundary conditions for their existence. Global modes, on the other hand, require periodic boundary conditions for their existence and have growth rates which depend on the average baroclinicity of the basic flow. These characterizations were put on a firm analytical basis via a WKB analysis. Due the generality of the techniques developed in PH, to study these two classes of unstable modes, they can be applied to many other instabilities, including the one under consideration here.

Following PH we will assume that the unstable mode of Fig. 22c is a local mode and as such does not depend on the periodic boundary conditions for its existence. The correctness of this assumption can be judged *a posteriori*. On this basis, we will take the domain to be zonally-infinite [i.e., $x \in (-\infty, +\infty)$]. Consequently, as boundary conditions we will require that the perturbation vanish at plus and minus infinity, i.e.

$$\psi' \rightarrow 0 \quad \text{as } |x| \rightarrow \infty \quad (78)$$

In addition, in order to isolate the locally-unstable easterly jet for further consideration, we will set

$$u_w(X) = \begin{cases} u_0 \cos[2\pi(X + 0.5)] & \text{when } |X| \leq 0.25 \\ 0 & \text{elsewhere.} \end{cases} \quad (79)$$

Notice that in (79) we have translated the X -axis so that the easterly jet is centered about $X = 0$ rather than $X = 0.5$. Subject to (78) and (79) we will now solve (77), using the techniques developed in PH. In this regard, the reader is referred to PH for any details which have been omitted here.

For what follows we will need to consider under what circumstances the perturbation expansion given by (66) can break down. A solution for which this expansion becomes unordered would be invalid and should therefore be discarded. As discussed in PH, an approximation such as this can break down in one of two ways: (1) if $k \rightarrow 0$ at some X then the leading term in (65b) can become comparable to the $O(\delta)$ term and (2) if $dk/dX \rightarrow \infty$ at some X while k remains finite. Only the latter type of

breakdown can occur in this problem since the former corresponds to a classical turning point, and cannot happen for unstable modes in this problem as $k = 0$ in (77) implies that $\omega = 0$.

Returning to (77), we note that since k depends on X through u_w , any particular branch of k is such that $k(-\infty) = k(+\infty)$. Because of this the only way the boundary condition (78) can be satisfied is if the solution switches branches for some X (within the domain). Branch switching, in turn, implies the existence of a point, say X_C , where two branches coalesce. However, as shown in PH, a coalescence point is, in general, also a breakdown point because $dk/dX = (dk/du_w)(du_w/dX)$ and $dk/du_w \rightarrow \infty$ there. [The behaviour of k in the vicinity of a coalescence point is obtained by considering a Taylor series expansion of the dispersion relation.] For this reason some special technique must be employed in order to continue the solution across the coalescence point. Fortunately, in the special case where $du_w/dX = 0$ at the coalescence point, this difficulty is circumvented and the expansion remains ordered through the coalescence point. Consequently, in our problem, we will demand that the coalescence point occurs at $X = 0$ since $du_w/dX = 0$ there.

It remains now to find the particular $\omega = \omega_C$ (if it exists) for which two branches of $k(X)$ merge at $X = 0$. In this regard it can be shown that

$$\partial_k \omega = 0 \tag{80}$$

at coalescence (where ω and k are considered complex). This is equivalent to the condition that $\omega(k)$ have a saddle point at coalescence. To find the saddle point in our problem we will perform a complete conformal mapping of the function $\omega(k)$. Consider Fig. 28 which is a plot

of lines of constant ω_r and ω_i as a function of m_r and m_i [$m = (2\pi\delta)^{-1} \cdot k$]. A saddle point clearly exists at $m = m_c \approx 2.06 + 0.21 \cdot i$. At m_c we find that $\omega_c \approx 0.66 + 4.60 \cdot i$. It should be pointed out that the imaginary part of ω_c is the so-called absolute growth rate at $X = 0$. For a discussion of the concept of absolute instability we refer the reader to Merkin (1977).

The complex frequency ω_c can now be used in (77) to determine $k(X)$. Given $k(X)$ we must ensure that the two branches which merge at $X = 0$, call them $k^+[u_w(X), \omega_c]$ and $k^-[u_w(X), \omega_c]$, are such that

$$k_i^+[u_w(\infty), \omega_c] > 0 \quad \text{and} \quad k_i^-[u_w(-\infty), \omega_c] < 0 \quad (81)$$

in order that the boundary conditions be satisfied. If this is the case, then our final solution is given by (68), with the exponent involving the integral over x written as

$$\int_{x_0}^x k dx = \begin{cases} \int_0^x k^+ dx & \text{for } x \geq 0 \\ \int_0^x k^- dx & \text{for } x < 0 \end{cases} \quad (82)$$

and $\omega = \omega_c$.

Consider Fig. 29 which is plot of two branches of $m = (2\pi\delta)^{-1} \cdot k$, designated m^+ and m^- , as a function of the zonal flow $u_w(X)$ [normalized so that $u_w(0) = -1$]. Notice that indeed the branches coalesce at $u_w(0) = -1$ as required if the solution is to be a valid one. Note also that m_i^+ crosses the u_w axis just slightly upstream of $u_w = -1$. This reflects the fact that the modulation pattern peaks just upstream of $X = 0$. Downstream of this point the mode decays to zero as required by the boundary conditions. Referring to m_i^- , we see that it is negative

for almost all u_w and decreases very rapidly near $u_w = 1$. This last observation indicates that the mode decays rapidly in the upstream direction. A consideration of m_r^+ and m_r^- shows that the mode lengthens upstream and shortens downstream of the point where $u_w = 1$.

Comparing the analytical solution with the numerical solution we conclude that the agreement, at least qualitatively, is quite good. In particular, the analytical solution has correctly reproduced the sharp upstream decay, the slower downstream decay and the location of the peak. In addition, the presence of long waves upstream and short waves downstream of the peak in the numerical solution is also seen in the analytical one. Quantitatively speaking, the agreement is also quite reasonable as can be seen when one compares, for instance, the numerically obtained frequency and the analytic one, $\omega \approx 3.61 \cdot i$ and $\omega_c \approx 0.66 + 4.60 \cdot i$, respectively. Admittedly, in contrast to the numerical mode, the analytic mode has a small but non-zero real frequency. Using a similar argument as before one could make the case that when one compares the period of oscillation of this mode with its e-folding time the mode is for all intents and purposes stationary.

We believe that the major reason for the discrepancy between the numerically and analytically determined frequencies is that the basic assumption that $\delta = L_y/L_x$ is small is only marginally satisfied for the basic flow studied here (recall that $\delta \approx 0.2$). Presumably, had we chosen the channel parameters so that δ were much smaller we would have found a better agreement between ω and ω_c . In fact, we have carried out a few calculations using smaller values for δ ; it was found, however that in these cases the numerical mode could not be resolved using only three y -components. To make a comparison between the numerical and

analytic modes would therefore require more y -components in the theory and hence a considerably more involved algebraic task, which we did not undertake.

For the sake of comparison, we include Fig. 30, which is the two-term counterpart (i.e., based on the two-term system) of Fig. 29. In contrast to the previous case, this mode grows just downstream of $X = 0$ and peaks at the point where $u_w \approx -0.97$. For the two-term system the absolute frequency is $\omega_c \approx 2.82 + 5.39 \cdot i$.

3.3.3 Discussion

In this section we have considered the linear stability of a topographically forced steady-state consisting of a constant mean zonal part and a wave with a single oscillation, in both the zonal and meridional directions [i.e. $(m_\alpha, n_\alpha) = (1, 2)$]. Growth rate curves, as a function of the zonal wind (u_s) and the topographic amplitude (h_0), for one of the unstable modes were obtained numerically. From an analysis of the frequencies and structures of these growing modes it was determined that while topographic instability is not the dominant instability, it does indeed exist for this topographic structure.

A major portion of this study was dedicated to a detailed analysis of the fastest-growing perturbation to a particular superresonant, large-amplitude steady-state flow ($u_s = 17 \text{ m s}^{-1}$ and $h_0 = 1 \text{ km}$). This mode is characteristic of the fastest-growing perturbation to a wide range of steady-states, making our results more general than they might at first appear. The fastest-growing perturbations to these steady-states are, in general, non-topographic insofar as they do not involve the direct interaction of the perturbation with the topography through a form drag mechanism.

We considered the structure and energetics of the fastest-growing perturbation. The mode was found to have a relatively simple meridional structure and a high degree of localization in the zonal direction. Most of the amplitude of the structure is located near and somewhat downstream from an easterly jet in the basic flow. A look at the energetics of the mode revealed that its overall exponential growth is strongly maintained by a transfer of easterly zonal momentum out of the basic-state, near the center of the channel. A smaller, but still important, energy exchange is found further downstream, in a region where the mode is meridionally-oriented when the basic flow is confluent and zonally-oriented when it is diffluent. An unfamiliar behaviour was found by Simmons et al. (1983) in their study of the stability properties of the 300 mb climatological mean January flow.

An analytic approximation to the fastest-growing mode was obtained using the WKB approximation coupled with some techniques developed by Pierrehumbert (1984) to study *baroclinic* instability. The approximate analytic solution correctly predicted the location and the shape of the unstable wavepacket but overestimated the frequency. More specifically, the analytic solution reproduced the amplitude peak just downstream of the easterly jet and the rapid decay of the envelope, both upstream and downstream from the peak (especially upstream). A better agreement between the numerically determined and the analytic frequency would have certainly been found had the basic flow been more slowly varying in the zonal direction, as required by WKB theory.

We believe that this study has been useful from the point of view of highlighting the role downstream variations play in the linear instability of inhomogeneous barotropic flow. In addition, this study

has confirmed the utility of local instability analyses in assessing regions of maximum eigenmode growth. Although this sort of analysis is too simple to be directly applied to the behaviour of any real fluid, it can assist in the physical understanding of the connection between spatial inhomogeneities, in a basic flow and preferred regions eddy activity.

In this chapter we have considered the *linear* instability of a particular class of non-zonal basic states which exist as exact solutions to the inviscid barotropic vorticity equation. Although linear theory can be useful in describing the initial growth of an infinitesimal perturbation to a given unstable basic flow, it is seriously limited by the fact that the latter remains formally unchanging with time. No matter how small the perturbation is initially it will, given the constant supply of basic state energy, grow so large that nonlinear effects cannot be ignored. In the next chapter we will consider the *nonlinear* evolution of initially small (as opposed to infinitesimal) perturbations to a number of unstable basic flows. Amongst the questions we will be asking are: (1) in what way(s) do the effects of nonlinearity halt the growth of the perturbation (as they must if energy is to be conserved)?, (2) how large, in amplitude, does the perturbation become before it is stabilized?; (3) does the perturbation maintain this maximum amplitude or does it begin some sort decay stage?, (4) how does the basic flow alter with time as the perturbation evolves?

CHAPTER 4
NONLINEAR ANALYSIS

4.1 Some background

In Chapter 3 the *linear* stability of free and topographically forced waves on a β -plane channel was investigated. In the case of topographically forced waves it was found that topographic (form drag), shear (Rayleigh) and resonant instabilities were present. For a given unstable equilibrium flow the strength, as well as the nature, of the instability depended on the particular parameters of the problem (such as the amplitude of the sinusoidal topography and the mean zonal wind). For example, near linear resonance (as determined by the channel width, D , the β -parameter and the mean zonal wind, u_s) the equilibrium flows were found to be unstable to infinitesimal perturbations of the form drag variety.

In the present investigation we will attempt to extend some of our earlier *linear* results into the *nonlinear* domain. As before, the equilibrium flows are the result of the interaction of a westerly mean zonal wind over a two-dimensional topography. The nonlinear stability properties of these flows will be determined by means of numerical integration of the spectral equations [see (11)] using as initial conditions each of the equilibrium flows plus its fastest-growing linear disturbance. (The fastest-growing linear disturbances are obtained, numerically, as in Chapter 3.) Unlike some similar studies, involving various *ad hoc* spectral truncations (e.g., Charney and DeVore, 1979; Fischer, 1980 and Egger and Metz, 1981), our integrations will be performed using sufficient resolution to ensure the accuracy of the solutions.

In some ways the objectives and methodology of the present investigation are similar to those of Mukougawa and Hirota (1986b). The latter also studied the nonlinear temporal evolution of forced waves in order to understand the phenomenon of wave amplification during blocking episodes in the troposphere. In contrast to our study, however, the bulk of their investigations involved the analytical treatment of near-resonant flows using a low-order spectral model, as in Charney and DeVore (1979). It was found that the evolution of the forced wave amplitude depends on the sign of the initial zonal flow perturbation: if the zonal flow is decelerated initially, the wave amplifies in a nonlinear oscillation; otherwise the wave amplitude decreases. In either case, the period of the oscillation decreases with an increase of the amplitude of the initial forced wave. [The use of the low-order model for these near-resonant flows was justified in a fully nonlinear spectral model with many degrees of freedom.] In the present study we will be considering off-resonant flows where many degrees of freedom are required to capture the nonlinear evolution (as will be demonstrated).

Direct numerical integration is by no means the only way to test the nonlinear stability of an equilibrium flow subject to a finite-amplitude disturbance. Instead, one might employ variational methods to determine criteria for nonlinear stability. In Arnol'd (1966), for instance, two powerful stability theorems were so obtained. (A thorough discussion on the subject of Arnol'd's nonlinear stability theorems can be found in McIntyre and Shepherd, 1986.) As discussed in Section 3.1, when the second theorem of Arnol'd is applied to our particular equilibrium solutions the following is obtained: if $u_s \geq \beta/(\pi/D)^2$ the equilibrium

flow is nonlinearly stable (i.e., stable in the Liapunov sense). (Liapunov stability means that if the disturbance is small initially the perturbed flow will remain "near" the unperturbed flow for all time.) Since the equilibrium flows which we will be considering in this study are all such that $u_s < \beta/(\pi/D)^2$ this stability criterion is not very useful.

Another means of studying the nonlinear behaviour of small-amplitude disturbances is to use the methods of weakly nonlinear theory. In fact, weakly nonlinear theory comprises a large proportion of the entire nonlinear theory now known. Deininger (1981), for example, exploited weakly nonlinear theory to obtain the finite-amplitude stability characteristics of a topographically forced wave on an infinite β -plane. Deininger found that a nonlinear feedback between the topographic wave and the disturbance produces an oscillation for topographically subresonant zonal flow and an explosive nonlinear instability for topographically superresonant zonal flow. It is important to bear in mind, however, that these results are restricted to a time period in which the disturbance is small, albeit finite. In the case of explosive instability nothing can be said about the behaviour of the disturbance beyond the time it achieves any significant amplitude. (Another weakness in this approach lies in the fact that the spectral expansion for the disturbance is severely truncated.) In our study we prefer not to make any *a priori* assumption regarding the amplitude or spatial characteristics of the disturbance and for this reason have opted for direct numerical integration (despite the heavy computer load).

Still another way to study the nonlinear stability of inviscid equilibrium flows is to utilize the methods of statistical mechanics.

Frederiksen and Carnevale (1986), for instance, used these methods to study the nonlinear stability properties of flow over topography in spherical geometry. In that study, climatic states were obtained using each of the equilibrium flows plus a finite-amplitude disturbance as initial conditions. The nonlinear stability properties of a given equilibrium flow was then obtained by comparing the initial condition with its corresponding climate. If the climate was the same as the initial condition, then the equilibrium flow was deemed stable; otherwise it was unstable. It was found, for example, that equilibrium flows for which the solid body rotation component of the zonal wind, u_1 , is eastward were unstable due to the generation of large amplitude transient waves. In contrast, for flows with westward u_1 , the equilibrium flow and the climate were virtually identical. Since in our study we are more interested in the time-dependence of the disturbances the methods of statistical mechanics have only limited utility. Notwithstanding this fact, in Section 4.4 we will obtain statistical equilibria in order to help interpret the asymptotic behaviour of our simulations.

Having set the stage we will now describe our own investigations. To begin, in Section 4.2 we discuss some of the technical aspects of our numerical model. In this section we pay particular attention to the fact that the truncated spectral equations do not identically conserve energy and potential enstrophy, as does the model equation. In Section 4.3 we discuss in detail each of the experiments, while in Section 4.4 we incorporate equilibrium statistical mechanics to rationalize the long term behaviour seen in our numerical simulations. Finally, in Section 4.5 we summarize our results.

4.2 Some preliminaries

As stated, in this study we intend to describe the results of a number of fully nonlinear integrations of the truncated spectral equations. In each case the initial condition represents an equilibrium flow plus its fastest-growing linear disturbance (hereinafter denoted FGLD). To this end we set as the initial condition for our nonlinear simulations to come

$$\psi(x, y, t=0) = \tilde{\psi}(x, y) + \delta \cdot \underline{\Psi}_r(x, y), \quad (83)$$

where $\underline{\Psi}_r$ is the real part of the eigenfunction corresponding to the FGLD to $\tilde{\psi}$. [The underscore indicates that $\underline{\Psi}_r$ has been normalized so that it is of the same order as $\tilde{\psi}^*$, i.e., $\underline{\Psi}_r = (\text{Max}|\tilde{\psi}^*|/\text{Max}|\underline{\Psi}_r^*|)\underline{\Psi}_r$.] The δ -parameter in (83) simply fixes the initial amplitude of the disturbance relative to the equilibrium flow. [Note that δ here is different from that of Section 3.3.] In what follows, δ will range from between approximately 0.02 to 0.3.

It is well known that fluid motions governed by the model equation [see (1)] are highly constrained due to the conservation of various quadratic invariants. Perhaps the most obvious time-invariant quantity associated with (1) is the channel averaged potential vorticity, $\langle Q \rangle$. (Recall that angle brackets denote horizontal averaging.) In addition to the fact that $d_t \langle Q \rangle = 0$, we also have

$$d_t E = d_t \left\langle \frac{|\nabla \psi|^2}{2} \right\rangle = 0 \quad \text{and} \quad d_t Z = d_t \left\langle \frac{Q^2}{2} \right\rangle = 0 \quad (84)$$

where E and Z are the energy and potential enstrophy, respectively. Besides E and Z conservation, in the absence of topography, the channel

averaged zonal flow is also conserved, i.e., $d_t \langle u \rangle = 0$. On the other hand, in the presence of a two-dimensional topography, we get instead that,

$$d_t \langle u \rangle = f_0 \langle v(h/H) \rangle \quad (85)$$

This is a form of the so-called form drag equation which implies that the channel averaged zonal flow can only change when, on average, there is a nonzero meridional flow across isolines of the two-dimensional topography, $h(x,y)$.

Returning to the spectral equations (11) we reiterate that these equations have been used by many other researchers, including Lorenz (1963), Boville (1981), Mitchell and Derome (1983) and Mukougawa and Hirota (1986b). Although they are relatively easy equations to formulate and implement they do have at least one (often ignored) drawback, as pertains the spectral forms of energy and potential enstrophy. It would be desirable if the finite set of spectral equations conserved E and Z as does the original model equation. However, as we will see, this system conserves these quantities only in the limit of infinite meridional resolution (i.e., as $N \rightarrow \infty$). The origin of this problem can be seen, perhaps most fundamentally, in the special case when $h = 0$. In this case, we know analytically that $d_t \langle u \rangle = 0$, however numerically we get

$$d_t \langle u \rangle = \sum_{\beta \epsilon \alpha} [F_\alpha(y-D) - F_\alpha(y-0)] (K_\epsilon^2 / K_\alpha^2) \psi_\beta \psi_\epsilon c_{\beta \epsilon \alpha} \quad (86)$$

where F_α denotes a mean zonal basis function of the form $\sqrt{2} \cos(\pi n_\alpha y/D)$. A detailed analysis (presented in Appendix E) of the triple sum on the

right-hand side of (86) reveals that it vanishes, nontrivially, only in the limit of infinite meridional resolution. In the general case where $h \neq 0$ we find the situation to be similar in terms of the numerical treatment of E and Z (as shown in Appendix F). Happily though, E and Z [and $\langle u \rangle$ when $h = 0$] are nearly conserved at moderate meridional resolution, say at $N \geq 15$ (as will be demonstrated through direct numerical integration). The fact that E and Z are not identically conserved, numerically, can actually be turned to our advantage in the sense that their non-conservation signals that the meridional resolution may not be entirely adequate.

Except where otherwise stated, in this study we set $M = N = 15$, leading to a set of 465 nonlinear differential equations. At this point it should be mentioned that for this resolution it was more efficient to use a transform method to solve the model equation rather than the interaction coefficient method implied by (11). Although the two methods yield the same results, for large resolution studies such as this the transform method is considerably more efficient. [For detailed account of the spectral transform method we refer the reader to Appendix B of Mitchell, 1982.] The time-stepping was performed using a centered scheme with the problem of time-decoupling controlled with a weak Robert time filter ($\nu \leq 0.01$). This time filter was designed by Robert (1966) and was later analyzed by Asselin (1972). Also, the original computer code was vectorized in order to take full advantage of a high speed CRAY X-MP supercomputer.

The linear disturbances used to perturb the initial steady flows, were obtained numerically using standard matrix eigenvalue techniques of the sort described in Chapter 3. Except where otherwise stated, we used the channel parameters set in Section 3.1 [see (22)].

4.3 Numerical simulations

We now describe a number of numerical simulations, each started with a steady flow plus its fastest-growing linear disturbance. In all, three basic experiments will be described. In the first experiment, involving an initial weak instability [$\tau = O(50)$ days], we will investigate how the linear disturbance behaves at finite-amplitude. Since the initial disturbance cannot grow exponentially for an indefinite period of time, certain nonlinear corrections must be affected in order to stabilize the system (albeit, maybe just temporarily). In the second experiment, involving a much stronger instability [$\tau = O(5)$ days], particular interest will be paid to the longer term behaviour of the system. The first two experiments incorporate a simple sinusoidal topography of the type used in Chapter 3. The third experiment, on the other hand, involves a less idealized topography, like that used by Kasahara (1966) in his study of the dynamical influence of mountain barriers upon atmospheric flow patterns. This latter simulation is performed in order to check the extent to which the behaviour seen in the previous simulations is a consequence of the highly idealized single-wave orography.

As stated, the first two experiments involve a topography which is a simple sinusoidal function, more specifically,

$$h = h_{\alpha} \cdot 2 \sin(2\pi m_{\alpha} x/L) \sin(\pi n_{\alpha} y/D) \quad (87)$$

where $m_{\alpha} = 2$ and $n_{\alpha} = 1$ [i.e., $\alpha = (2,1)$]. With this topography the steady flow streamfunction arising from (4) can be written

$$\bar{\psi} = -u_s \cdot y + \bar{\psi}_\alpha \cdot 2 \sin(2\pi m_\alpha x/L) \sin(\pi n_\alpha y/D) \quad (88)$$

where $\bar{\psi}_\alpha = f_0 (h_\alpha/H) / (K_\alpha^2 - K_s^2)$ and $K_s^2 = \beta/u_s$

We notice that the steady flow streamfunction comprises a mean zonal component (i.e., $-u_s \cdot y$) plus a forced stationary wave which has precisely the same form as the topography. With regards to the latter we mention that in both of the experiments involving (87), $h_\alpha > 0$ and $K_\alpha^2 < K_s^2$, which implies that the forced stationary wave is exactly half a wavelength out of phase with the topography (since $\bar{\psi}_\alpha < 0$). A full linear stability analysis of this particular steady flow, in terms of h_α and u_s , can be found in Section 3.1 (see, for example, region IV of Figure 13).

Before continuing we note that we will frequently use nondimensionalized quantities. In this regard it should be understood that we have nondimensionalized the space coordinates and time with D^{-1} and u_s/D , respectively.

4.3.1 Experiment 1: Initial weak instability

a. Initial condition

In this experiment we set $u_s = 10 \text{ m s}^{-1}$ (or $u_s = 1$, in nondimensional terms) and $2h_\alpha/H = 0.095$. The steady flow resulting from this parameter setting is shown in Fig. 31a. Since the steady flow is symmetric about $x = L/2$ we have plotted the streamfunction over only half the domain. (The position of the topographic ridge is indicated with an arrow in Fig. 31a.) The structure of the FGLD [i.e., $\Psi_F(x,y)$]

corresponding to this flow is shown in Fig. 31b. To resolve the disturbance we have used 15 zonal and 15 meridional wavenumbers (i.e., $M - N = 15$). We find that the disturbance has absolutely no mean zonal energy and, due to the symmetric nature of the basic flow, contains only odd zonal wavenumbers.

The disturbance of Fig. 31b has an e-folding time ($\tau = |1/\omega_i|$) of approximately 47 days and a period of oscillation ($T = |2\pi/\omega_r|$) of about 33 days. Part of the motivation for studying the time-dependent behaviour of this slowly amplifying disturbance lies in the fact that much of the analytical theory used to study the finite-amplitude stability of planetary waves (e.g., Loesch, 1978 and Deininger, 1981; 1982) pivots around the assumption of weak instability. In this way, then, we will be able to compare our numerical results with the analytical ones. We stress, however, that in contrast to the analytical approach, in our numerical treatment we make absolutely no a priori assumptions regarding the disturbance amplitude; that is, the initially small-amplitude disturbance is not required to remain small.

To understand the subsequent time-dependent behaviour of this perturbed steady flow, it is imperative that we understand the initial instability mechanism itself. So, to aid us in this endeavor we form the energy equation governing the initial linear disturbance, i.e.

$$d_t E' = - \langle u'v'(\partial_x \tilde{v} + \partial_y \tilde{u}) \rangle - \langle (u'^2 - v'^2) \partial_x \tilde{u} \rangle \quad (89)$$

This equation has been discussed in detail in subsection 3.3.2. As concerns the disturbance at hand, we find that the second term on the right-hand side of (89) is by far the largest (over the disturbance's entire period of oscillation), indicating that this instability relies mainly on the existence of zonal shears in \tilde{u} . More specifically, this

instability depends on regions of confluence ($\partial_x \bar{u} > 0$) and difffluence ($\partial_x \bar{u} < 0$) in the steady flow. To see this mechanism more clearly, we have plotted, in Fig. 31c, positive contours of $-(u'^2 - v'^2) \partial_x \bar{u}$. Notice that the major contribution to the channel average of this quantity comes from a region near the southern boundary, where the steady flow is diffluent and the disturbance is zonal.

It is interesting to consider the effect of truncation on this disturbance. Referring to Table 3 we notice that the instability first appears at $M = N = 3$ but does not begin to converge till around $M = N = 15$. Given that such a relatively large number of waves is required to resolve $\Psi_r(x, y)$ it is natural to question the role the small scales play. To partially answer this question, we present Fig. 32a, which shows the zonal and meridional energy spectra of Ψ_r (note that Ψ_r has no energy in even m). We see that Ψ_r is dominated in the zonal direction by $m = 1$ and in the meridional direction by $n = 1$ and $n = 2$. In fact, a detailed analysis reveals that most of the structure can be ascribed to just two wave components, namely, $\beta = (1, 1)$ and $\epsilon = (1, 2)$. Comparing $E'(m)$ and $E'(n)$ we also conclude that most of the small scale structure in Ψ_r lies in the meridional direction.

Further to Fig. 32a we present Fig. 32b which is a plot of $\Delta \Psi_r$, with the β and ϵ waves removed in order to highlight the small scales. Particularly striking here is the localized band of large vorticity gradient in the northern half of the channel. The fact that this structure exhibits a strong zonal-wavenumber-2 modulation pattern, corresponding to the zonal structure of the basic wave, may suggest the presence of a nonparallel critical layer. (The existence of such a critical layer, for a neutral wave, was demonstrated by Merkin, 1982.)

Since the subject of nonparallel critical layers is well outside of the scope of the present study we will not pursue this interesting subject any further. To conclude our description of the FGLD we point out that since the initial disturbance requires such a fine structure in order to be resolved, a usual multiple scaling approach based on severe truncation (e.g., Deininger, 1981) would not be applicable.

Now we turn to an examination of the dynamical interactions between the forced stationary wave and the superimposed disturbance with respect to which it is unstable. In so doing, we hope to address the following questions: (1) by what means will the initially small-amplitude disturbance be stabilized and how large will it grow before stabilization? (2) what role will topographic form drag play? (3) after the initial stabilization, will the instability redevelop, thereby restarting the whole process or will the system move into a new regime with little, or no, memory of its initial condition? (4) will the smaller scale waves remain at their initial low-energy level or will they play an increasingly significant role as time passes?

b. Time-dependent behaviour

In this experiment we set $\delta = 0.02$ so that the amplitude of the disturbance is initially very small compared with the steady wave. The time integration will extend over about eight e-folding times of the initial, slowly amplifying, disturbance. To determine the right time step, Δt , we note that the highest frequency eigenmode obtained from the linear analysis has $1/\omega_r \approx 4.2$ hours. Therefore, we choose $\Delta t = 1$ hour to ensure that this high frequency mode is resolved, as required by the Courant-Friedrichs-Lewy (CFL) convergence condition for computational stability (i.e., $\omega_r \Delta t < 1$).

Before describing the simulation itself we will define two terms to be often used in the sequel. The *basic wave*, denoted ψ^b , is simply the wave in the spectral expansion with the same wavenumber as the topography, i.e.

$$\psi^b = \psi_{\alpha}^+(t) \cdot F_{\alpha}^+(x, y) + \psi_{\alpha}^-(t) \cdot F_{\alpha}^-(x, y) \quad \text{where} \quad (90)$$

$$F_{\alpha}^+ = 2 \sin(2\pi m_{\alpha} x/L) \sin(\pi n_{\alpha} y/D), \quad \& \quad F_{\alpha}^- = 2 \cos(2\pi m_{\alpha} x/L) \sin(\pi n_{\alpha} y/D).$$

Recalling (87) we see that $\psi_{\alpha}^- \cdot F_{\alpha}^-$ is that part of the basic wave that is a quarter of a wavelength out of phase with the topography. On the other hand, the *disturbance*, denoted ψ^d , is defined to include all the waves except for the basic wave. According to these definitions, at $t = 0$ we have that $\psi^b = \tilde{\psi}_{\alpha} \cdot F_{\alpha}$ and $\psi^d = \delta \cdot \underline{\Psi}_r$. In other words, initially the basic wave corresponds to the forced stationary wave component of the steady flow while the disturbance corresponds to the superimposed FGLD.

An informative overview of the simulation is afforded through Fig. 33a which shows the total energy, E , and the mean zonal energy, \bar{E} , over 9600 timesteps. We see, as hoped, that E remains nearly constant, i.e., to within 0.05 % of its initial value. The potential enstrophy (not shown) is also conserved to within 0.05 % of its initial value. The mean zonal energy, on the other hand, goes through some rather dramatic changes over the integration period. The evolution of \bar{E} begins with a monotonic decrease till about day 200 (or about four e-folding times) at which point an amplifying oscillation with a period of approximately 15 days appears. To quantify the relative importance of the changes in \bar{E} we note that at $t = 394$ days \bar{E} comprises less than 40 % of the total energy, as compared with more than 75 % at $t = 0$. Needless

to say, an appreciation of the dynamics underlying the behaviour of the mean zonal energy will be prerequisite to a firm understanding of the dynamical interactions between the basic wave and the disturbance.

The evolution of the basic wave energy, E^b , and the disturbance energy, E^d , is shown in Fig 33b. Comparing these curves with \bar{E} from Fig. 33a we find that, perhaps surprisingly, in the first half of the integration the disturbance appears to derive most of its energy from the mean zonal part of the flow rather than the basic wave. However, despite its relative passivity during this time, we will see that the basic wave is crucial, both from the point of view of the evolution of the mean flow and the disturbance. More precisely, we find that the basic wave: (i) allows for the modification of the mean flow via topographic form drag and (ii) provides the zonal shears upon which the disturbance initially feeds (as described in part a). Before discussing certain aspects of (i) and (ii) we point out that this behaviour is in stark contrast to the nonlinear equilibrating mechanism described in Deininger (1981). In Deininger's weakly nonlinear study the mean zonal flow was unchanged due to the fact the basic wave (or "topographic" wave, using his terminology) remained fixed relative to the topography, thereby disabling topographic form drag.

To appreciate the important role the basic wave plays in this simulation and, in particular, to understand its effect on the mean flow we recall the form drag equation (85). For this special case of a single-wave topography, the form drag equation can be rewritten as

$$d_t \langle u \rangle = - (2\pi m_\alpha f_\alpha / HL) h_\alpha \psi_\alpha(t) \quad (91a)$$

Recall that $\psi_{\alpha}(t)$ is the spectral coefficient of the component of the basic wave that is a quarter of a wavelength out of phase with the topography (recall also that $h_{\alpha} > 0$). This equation is a mathematical statement of the fact that low pressure (i.e., $\psi_{\alpha} > 0$) to the east of a mountain causes a deceleration of the mean-flow (i.e., $d_t \langle u \rangle < 0$). Conversely, high pressure toward the east ($\psi_{\alpha} < 0$) of a mountain implies an acceleration of the mean flow ($d_t \langle u \rangle > 0$). (In Deininger (1981), $\psi_{\alpha}(t) = 0$ so that this mechanism was inoperative.) Bearing in mind these ideas, consider Figs. 34a, b which show the evolution, over the first 240 days, of $\psi^b = \psi^b(\psi_{\alpha} - \tilde{\psi}_{\alpha}, \psi_{\alpha})$ and $\langle u \rangle$, respectively. As expected, we find that $\langle u \rangle$ decreases when $\psi_{\alpha} > 0$ (i.e., $0 < t \lesssim 200$ days) and increases when $\psi_{\alpha} < 0$ (i.e., $200 \lesssim t \lesssim 240$ days).

Given that the basic wave is directly responsible for changes in the channel-averaged flow, we now ask to what extent this can account for the behaviour of \bar{E} seen in Fig. 33a. To see the link between the basic wave and \bar{E} consider that $2\bar{E} = \langle \bar{u}^2 \rangle = \langle [u_s + \hat{u}(y, t)]^2 \rangle$, which in turn, implies

$$d_t \bar{E} = u_s \cdot d_t \langle u \rangle + \frac{1}{2} \cdot d_t \langle \hat{u}^2 \rangle \quad (91b)$$

Using (91a) in (91b) reveals that the basic wave, through its influence on $\langle u \rangle$, systematically affects the tendency of \bar{E} . In fact, in this simulation most of the changes in \bar{E} seen in Fig. 33a can be accounted for by this dynamical arrangement. Now, putting these observations together, we conclude that despite the apparent passivity of the basic wave (see E^b in Fig. 33b during the first half of the simulation) small changes in its phase relative to the topography result in significant

changes in the mean zonal energy. From the point of view of the disturbance this is important since energy which is lost or gained by the mean flow then becomes available for its own growth or decay.

Returning to Fig. 34a we notice that this wave behaves fairly erratically for the first 200 days. However, after day 200 the wave begins to show a fairly systematic westward phase propagation (as evidenced by the clockwise rotation of the trajectory). This westward propagation can be seen very clearly in Fig. 34c, which extends the trajectory to day 400. The evolution of $\langle u \rangle$ over the same time period is shown in Fig. 34d. The approximate 15-day vacillation seen in $\langle u \rangle$ can be understood as the consequence of the interference of the free-travelling wave of Fig. 34c [i.e., $(\psi_\alpha - \tilde{\psi}_\alpha) \cdot \dot{F}_\alpha + \psi_\alpha \cdot F_\alpha$], and the initial forced-stationary wave [i.e., $\tilde{\psi}_\alpha \cdot F_\alpha$]. That such a vacillation is possible has been nicely demonstrated by Lindzen et al. (1982), in their study of vacillations in zonally-averaged flows. In that study the authors used a linearized wave equation [obtained by substituting, in our notation, $\psi = -u_s \cdot y + \psi^b$ into (1)] to demonstrate that the approximate period of this vacillation is determined by the period of the free-travelling Rossby wave with the same horizontal wavenumber as the topography, i.e.,

$$T_\alpha = 2\pi / |\omega_\alpha| \quad \text{where} \quad \omega_\alpha = \frac{2\pi}{L m_\alpha} (u_s - \beta / K_\alpha^2) \quad (92)$$

For the case at hand T_α , as determined by (92), is approximately equal to 16 days which compares very well with the 15 day period of oscillation we find numerically.

We now turn our attention to the behaviour of the disturbance in this simulation (see E^d in Fig. 33b). To begin we remark on the

exceedingly large amplitude the disturbance attains. (For instance, $E^d/E^b \approx 0.47$ at $t = 200$ days as compared with $E^d/E^b \approx 0.00037$ at $t = 0$.) Clearly, no analytical method which is based on the assumption that the disturbance forever remains small could capture the finite-amplitude behaviour of this disturbance. Next, we point out that during the entire simulation the disturbance is dominated by the β and ϵ waves (see the dashed curve in Fig. 33b). (We remind the reader that these were the dominant waves in ψ^d initially.) In order to follow the behaviour of ψ^d it will suffice, therefore, to consider the behaviour of these waves alone. The amplitude of these primary waves, over the first 240 days is shown in Fig. 35a (where $[A_\beta^2, A_\epsilon^2] \equiv [\psi_\beta^2 + \psi_{\bar{\beta}}^2, \psi_\epsilon^2 + \psi_{\bar{\epsilon}}^2]$). Notice that the amplitude of both waves changes smoothly from a period of quasi-exponential growth to decay. As pertains the respective phases of the primary waves we find that they propagate zonally at nearly the same phase speed, but in the opposite direction. Consider, for example, the westward propagation of the β -wave as shown in Fig. 35b.

Looking more carefully at the primary waves we find that, due to small changes in their time-dependent phase speeds, the sum of their phases evolves as in Fig. 35c. We note that $\Sigma\theta \equiv \theta_\beta + \theta_\epsilon + \theta_\alpha$ includes a small contribution from the basic wave (e.g., $|\theta_\alpha| < 0.5^\circ$). Notice that for about the first 120 days the primary waves behave almost linearly, insofar as their phase sum barely changes at all (θ_β decreasing and θ_ϵ increasing). It turns out that during this initial quasi-linear stage the disturbance is always positioned to extract energy from the basic wave, through the instability mechanism described in part a. Eventually, however, the phase sum of the primary waves

begins to change and, in particular, to approach a value of 90° . Comparing Fig. 35c with Fig. 35a we notice that the growth of the disturbance halts precisely when $\Sigma\theta = 90^\circ$. At this time the unstable phase relationship which initially existed between the primary waves and the basic wave has been adjusted in such a way as to "turn off" the growth mechanism, thereby leading to the decay (albeit short-lived) of the disturbance.

Following the behaviour of the disturbance past the initial adjustment stage we notice from Fig 33b that E^d appears to go through a second stabilization (following a peak in E^d at $t \approx 320$ days). After this second stabilization the disturbance explodes in amplitude. From what we have seen so far it is absolutely clear that regardless of the criteria one might select, the steady flow of Fig 31a is nonlinearly unstable. Despite the fact that the initial disturbance possessed such a large e-folding time (i.e., $\tau \approx 47$ days) and such a small amplitude, the system is found departing very rapidly from its initial condition after only six e-folding times. Further to this consider Figs 36a-c which show the total streamfunction at $t = 100, 200$ and 300 days, respectively. In addition, consider Figs 36d-f which show the vorticity of the disturbance at the same times. Take note that in Figs. 36d-f the contour interval at $t = 200$ and 300 days is five times greater than at $t = 100$ days. Although the small scale waves have not played a significant role up till now it is apparent from this sequence that they are becoming increasingly energetic and as such will presumably play a greater part in the future.

By way of summarizing our results we will briefly respond to some of the queries posed at the onset: (1) the initially small-amplitude

disturbance did not remain small but, rather, eventually became as large as the basic wave itself; (2) an interaction between the basic wave and the topography, via form drag, led to an amplifying 15-day vacillation in the mean flow which came to dominate the overall picture; (3) the small scale waves remained relatively passive, however, indications were that they would become increasing significant (this will be considered further, shortly). One of the more interesting features of this simulation was the mean flow vacillation, which arose from the periodic interference between a forced stationary wave on the scale of the topography and a free travelling Rossby wave (with the same wavenumber). Lindzen et al. (1982) argue that such an interference effect is a plausible explanation for some vacillations found in both rotating annulus experiments (Pfeffer et al., 1980a,b) and the atmosphere (Winston and Krueger, 1961). The authors point out, however, that their theory cannot, in itself, explain how the travelling Rossby waves are generated. Possibly these waves are generated as in our simulation, that is, through a finite-amplitude interaction between the forced stationary wave and a superimposed disturbance with respect to which it is unstable.

Now, rather than take this simulation any further we have decided to perform a new experiment initialized with a steady flow which is much more unstable to linear disturbances [e.g., $\tau = O(5)$ days]. In this more physically relevant experiment we hope to see the long term behaviour of the system earlier in the integration. With regards to the long term behaviour of this, as well as the previous, simulation we should bear in mind that our model is quite unrealistic. Clearly, the inclusion of friction and forcing would change the picture, since these

processes operate at time scales of a few days to some weeks. Notwithstanding this fact, we believe that a solid understanding of the inviscid limit is requisite to understanding more complicated systems.

4.3.2 Experiment 2? Initial strong instability

a Initial condition

As in the previous experiment we will use the sinusoidal topography given in (87). In this experiment, however, we choose $u_s = 16$ m/s and $2h_a/H = 0.12$. For these parameter values one should expect the steady flow to be more unstable than before since u_s is closer to its resonance value (of approximately 19.89 m/s) and the topographic amplitude is higher. This expectation is confirmed by a numerical analysis which yields a FGLD for which $(\tau, T) \approx (4.72, 28.37)$ days (when $M = N = 10$). Since the initial disturbance is still well resolved when $M = N = 9$ (see Table 3) we will, for convenience, use this lower resolution initial disturbance for this simulation (We note that in the actual integration the model is run at the higher $M = N = 15$ truncation level) The disturbance defined by $M = N = 9$ is such that $(\tau, T) \approx (4.70, 28.41)$ days. Consider Figs 37a, b which shows $\bar{\psi}$ and ψ_r in this case

b Time-dependent behaviour

Here we will mainly discuss our results for $\delta = \sqrt{0.02}$, however some mention will be made of a simulation starting with a larger amplitude initial disturbance (i.e., $\delta = 2\sqrt{0.02}$). On the basis of the initial linear analysis we have chosen a timestep of of $\Delta t = 15$ minutes for this

simulation. Consider Fig. 37c which shows E and \bar{E} over the integration period. We feel that, on the basis of the good energy conservation seen in Fig. 37c, our solution is reasonably accurate (E stays within 0.5 % of its initial value). Further to this, we refer the reader to Table 4, which compares a few important quantities at $t = 60$ days obtained after running the model at a lower resolution ($M = N = 13$) and with a smaller timestep ($\Delta t = 5$ minutes). Also, as a quick assessment of the treatment of the smaller scale waves in the numerical model, we note that at $t = 60$ days the potential enstrophy, Z , is within 3 % of its initial value. The fact that the potential enstrophy is not as well conserved as the energy indicates that, by $t = 60$ days, the small scale part of the flow is not being treated quite as well as the larger scale part (this will be pursued further shortly).

Returning to Fig. 37c we notice that \bar{E} behaves quite interestingly over the integration period. As can be seen, \bar{E} monotonically decreases till $t \approx 14.5$ days and thereafter remains relatively constant till $t \approx 25$ days. Notice that by $t = 25$ days the mean zonal energy has decreased to approximately 25 % of its initial value. Following day 25, \bar{E} shows a sharp increasing trend which is marked by a large, but diminishing, vacillation (with a period of approximately 15 days). In the last half of the simulation \bar{E} oscillates around a mean value which represents about 75 % of the total energy. (Initially, \bar{E} comprises only 25 % of the total energy.) By way of summarizing the overall behaviour of the mean zonal energy we simply state that in the first 25 days there is an energy transfer from the mean zonal to the wavy part of the flow (i.e., $\bar{E} \rightarrow E^*$) while in the last 75 days there is a much more significant reverse transfer (i.e., $\bar{E} \leftarrow E^*$).

Turning to the behaviour of $\langle u \rangle$, shown in Fig. 38a, we notice that, after only four or so e-folding times (recall that $\tau \approx 5$ days), the mean wind reverses direction, going from westerly to easterly. Following this dramatic reversal, $\langle u \rangle$ continues to decrease for about another 30 days at which point it settles down to a period of relative calm as it oscillates gently around an average value of approximately -1.3 (or -21 m s^{-1} in dimensional units). [Recall that initially $\langle u \rangle = +1.0$ (or 16 m s^{-1}).] Since we know that $d_t \langle u \rangle \propto -h_\alpha \cdot \psi_\alpha(t)$ we should expect corresponding changes in the basic wave. To see these changes, consider Fig. 38b which shows that the basic wave initially propagates eastward but reverses completely towards the west at around the time of the mean wind reversal. Over the last fifty days the basic wave exhibits an oscillatory behaviour, which is the combination of a westward propagating transient component and, a much stronger, stationary component [The stationary component represents high (low) pressure situated directly over the mountain (valley).]

As concerns the streamfunction, consider Figs 39a, b which show ψ and \bar{u} at $t = 25$ days. At this time the flow is dominated by a wavy structure on the scale of, but slightly out of phase with, the topography. A sequence of subsequent streamfunction plots (not shown) reveals that the transient component of the basic wave decays and the easterly mean-wind increases. For example, consider Figs. 39c, d which shows ψ and \bar{u} at $t = 60$ days. Notice the strong easterly flow which departs southward over the mountain and northward over the valley. Although the wavy part of the flow is largely dominated by the wave on the scale of the topography, other scales are also evident. To see the contribution of the non-topographic scales consider Fig 39e which shows

the zonal and meridional energy spectra, with the basic wave removed. Notice the rather flat appearance of both spectra at large wavenumbers, which suggests that the small scales may be beginning to equilibrate, in the statistical mechanical sense. [Whether a statistical equilibrium can actually be supported by this finite system is questionable since it identically conserves neither of the quadratic invariants (this will be taken up further in Section 4.4).] Further, to Fig. 39e we point out that the sum of the individual energies of the non-topographic modes is only about one half that of the basic wave itself.

To assess the sensitivity of the system to a change in the magnitude of the initial disturbance we reran the model with $\delta = 2/\sqrt{0.02}$ (twice the previous disturbance amplitude). Outside of a faster initial development, the behaviour of this simulation is in all essential respects identical to the $\delta = \sqrt{0.02}$ case. This can be seen, for instance, by comparing the dashed and solid curves of Fig. 38a. Notice that although the mean wind reversal occurs earlier than before, $\langle u \rangle$ ultimately settles down to approximately the same value. The fact that these two cases behave so similarly is not that surprising since their initial E and Z values are so close [i.e., $(E_0, Z_0) \approx (2.078, 74.184)$ when $\delta = \sqrt{0.02}$ and $(E_0, Z_0) \approx (2.152, 75.375)$ when $\delta = 2/\sqrt{0.02}$]. In Section 4.4 we will offer an explanation, based on the theory of statistical mechanics, for the similarity between these simulations. Finally, we present Fig. 40 which shows the evolution of the total and mean zonal potential enstrophies. Notice that shortly after the mean wind reversal (at $t \approx 25$ days) the total potential enstrophy begins to show a slow but noticeable decreasing trend. This behaviour is indicative of increasing activity around the truncation wavenumber.

A similar mean wind reversal as we have observed here was also seen by Edelman (1972). The latter obtained an approximate stationary solution of the shallow water equations, initialized with uniform westerlies, by performing successive time-averaging of the simulation. However, as pointed out by Fischer (1980), Edelmann's solution may have converged to a stationary solution with easterly winds as a consequence of the method of integration. Egger and Metz (1980) also found, through simulation of the barotropic vorticity equation, that $\langle u \rangle$ can decrease dramatically when it is initially positive (i.e., westerly). However, Egger and Metz's conclusions were limited by the severe truncation used (Sawford and Frederiksen, 1983).

The fact that uniform westerly flow over topography can generate strong transients leading to its ultimate demise has been known for some time now. In contrast, it is known that an initial uniform easterly flow will not necessarily generate any strong transient behaviour. Kasahara (1966), for example, through direct numerical simulation of the shallow water equations, found that westerly flow over topography could produce a train of long waves on the lee side of an obstacle. On the other hand, no such long waves were seen to appear in the case of initial easterlies. To see whether our model behaves similarly or not we performed two simulations starting with $u_s = +16 \text{ m s}^{-1}$ and $u_s = -16 \text{ m s}^{-1}$ [Corresponding to initial uniform westerlies and easterlies, respectively (i.e., $\psi = \pm u_s y$ at $t = 0$).] Referring to Figs. 4la, b, we indeed find their behaviour to be very different, with the easterly case remaining stable and the westerly case leading to large oscillations (with $\langle u \rangle$ tending to decrease). We note that the qualitative differences between initial westerly and easterly flow over

topography can be understood using conservation of potential vorticity arguments. Rather than review these arguments we simply refer the reader to Holton (1979, pg. 89-91).

Returning to Fig. 41b we find that in the stable easterly case the vacillation period obtained by linear interference theory [see (92)] and that by integration are almost identical (i.e., $T_{\alpha} \approx 4.6$ days). (We note that the circular shape of the trajectory is also consistent with the theory.) By contrast, in the unstable westerly case we find that: (1) the theoretical period (of approximately 42 days) is much longer than the numerical period (of approximately 15 days) and (2) the trajectory is quasi-elliptical rather than circular. The failure of the theory in this case lies in the fact that, strictly speaking, the theory only works in situations wherein the variation of the mean zonal wind is small enough for the linearization to apply. As a final remark we point out that the elliptical shape of the latter orbit is reminiscent of Yoden (1987) who described a new class of stratospheric vacillations using a highly truncated spectral model. These vacillations were interpreted as a nonlinear interference between a stationary wave and a topographically modified Rossby wave where variations of the mean zonal wind are important to the wave behaviour. (In linear interference theory it is assumed a priori that the fluctuation of the mean zonal wind has no effect on the wave structure.)

In the next experiment we will check the extent to which the qualitative behaviour we have found in this experiment is a function of our choice of a highly idealized sinusoidal topography.

4.3.3 Experiment 3: Localized topography

a. Initial condition

In contrast to the previous ones this experiment will involve a topography which is localized in space. More specifically, the topography will be Gaussian in the zonal direction and sinusoidal in the meridional direction, i.e.,

$$h(x,y) = \hat{h}(x) \cdot \sin(\pi y/D) \quad (93)$$

$$\text{where } \hat{h}(x) = \begin{cases} h_g \cdot \left[e^{-((2x-L)/2r)^2} - e^{-(L/2r)^2} \right] & \text{for } 0 \leq x \leq L \\ 0 & \text{otherwise} \end{cases}$$

Note that $\hat{h}(x)$ has a maximum, at $x = L/2$ of $h_o = h_g \cdot (1 - \exp[-(L/2r)^2])$ and decays to zero at $x = 0$ and $x = L$. In the sequel, we take $h_o/H = 0.1$ and $r = D/2$. Ultimately, this topography will be projected onto our basis functions given in (9). We note that the spectrally expanded topography will differ from (93) by a constant, owing to the fact that the spectral expansion has no channel average. However, since $h(x,y)$ only appears as a differentiated quantity in (1), this disparity is inconsequential. Consider Fig. 42a which is a plot of $h^*(x,y)$

Given the localized topography of Fig. 42a the corresponding steady flow is obtained by substituting the spectral form of (93) into (4) and applying the Galerkin procedure, with the result that

$$\bar{\psi} = -u_s \cdot y + \sum_{\alpha} \bar{\psi}_{\alpha} \cdot F_{\alpha}(x,y) \quad (94)$$

[The $\bar{\psi}_\alpha$'s are defined in (88).] Recalling (88) we see that rather than one resonance point, as in the case of the single-wave topography, we now have linear resonance whenever $u_s = \beta/K_\alpha^2$. For instance, $u_s = 17$ m/s is sandwiched between resonances at approximately 19.9 and 15.3 m/s. [These resonant wind speeds are associated with the $\alpha = (2,1)$ and $\alpha = (3,1)$ waves]. In this case, the flow defined by (93)-(94) is dominated by a combined zonal-wavenumber-2 and -3 structure. The actual steady flow is shown in Fig. 42b.

A stability analysis reveals that the FGLD to the steady flow of Fig. 42b is such that $(\tau, T) \approx (13.3, 35.6)$ days (when $M = N = 15$). The structure of the FGLD is shown in Fig. 42c.

b. Time-dependent behaviour

In this simulation we chose $\delta = 2\sqrt{0.02}$ and $\Delta t = 0.25$ hour. Consider Fig. 43a which shows the evolution of E and \bar{E} for this simulation. We note immediately the qualitative similarity in \bar{E} , in this simulation, and \bar{E} seen previously (see e.g., Fig. 37c). As before, \bar{E} initially decreases as $\langle u \rangle$ (not shown) tends to zero. [As regards $\langle u \rangle$, we note that $\langle u \rangle \approx 1.000, -0.014$ and -0.760 at $t = 0, 100$ and 400 days, respectively.] Following the mean wind reversal (at about $t = 100$ days), \bar{E} increases to, and remains at, a much higher value than at $t = 0$.

Consider Fig. 43b which shows the evolution of the energy in zonal wavenumber-1 and -2. As can be seen, most of the energy that is lost by the mean flow in the first 100 days is transferred into zonal wavenumber-1. However, following $t = 100$ days the energy in zonal wavenumber-1 is gradually returned to the mean flow. As in the previous simulations this latter trend is characterized by a mean flow

vacillation arising from the periodic interference between two waves with the same horizontal wavenumber but different phase speeds.

The eddy streamfunction and mean zonal flow at $t = 100$ and $t = 400$ days are shown in Figs. 43c, d. [Take note that the contour interval in Fig. 43c is three times that of Fig. 43d.] By comparing these plots (and bearing in mind Figs. 43a, b) we find that after around day 100 the eddy part of the flow becomes substantially decreased while the mean zonal part becomes more negative. In Fig. 43d (i.e., ψ^* at $t = 400$ days) we note, for future reference, the presence of a high pressure system overlying the mountain.

On the basis of this experiment we conclude that the qualitative behaviour we saw in the previous simulation is not merely an artifact of the sinusoidal topography. Having said this we will now turn our attention to rationalizing the asymptotic behaviour of these simulations using the methods of equilibrium statistical mechanics.

4.4 Statistical mechanical equilibrium

In the last two subsections it was found that the numerical simulations consistently evolved towards relatively stable states with strong easterlies, on the one hand, and high pressures overlying high ground, on the other. Along with this tendency there was, in each case, a slow decrease in the potential enstrophy. The nature of these asymptotic states, together with the increasing activity around the truncation wavenumber (as measured by the slight lack of conservation of potential enstrophy), suggested to us that the simulations were relaxing towards classical statistical equilibria. In this section we will pursue this matter further.

To check to what extent the asymptotic behaviour of our numerical simulations can be understood as a relaxation towards statistical mechanical equilibrium is problematic, since these methods rely on the conservation of E and Z in the truncated system. [Recall the E and Z are not exactly conserved in our particular, but widely used, system.] By way of circumventing this problem we propose to: (1) adjust the numerical model in such a way that E and Z are identically conserved; (2) perform a new simulation initialized as close as possible to experiment 2 and finally; (3) compare the asymptotic behaviour of this simulation with the corresponding equilibrium derived using the methods of statistical mechanics. In this way, we hope to shed some light, albeit indirectly, on the long term behaviour of our previous simulations.

In subsection 4.4.1 we write down the equations governing statistical equilibrium and outline the numerical method used to solve them. We note that this will comprise only a brief review of the methods of classical statistical mechanics since the details can be

found elsewhere (e.g., Salmon et al., 1976). In subsection 4.4.2 we describe the results of the new numerical simulation, while in subsection 4.4.3, we compare the long term behaviour of the new simulation with the corresponding statistical equilibrium.

4.4.1 Methods of statistical mechanics: a brief review

The tacit objective of statistical mechanics is to obtain time-mean solutions to a finite set of nonlinear equations, without having to actually solve the initial-value problem itself. In practice, this involves replacing the finite set of deterministic equations [involving, say, the real spectral coefficients $(\psi_\beta(t))$] by a time-independent set governing some statistical property of flow. The solutions to this latter set of equations represent an ensemble average over a large number of realizations of the system (all with the same initial E and Z). The prerequisites for the previous step are that Liouville's theorem be satisfied (i.e., $\sum \partial\psi_\beta/\partial\psi_\beta = 0$) and that the truncated versions of energy and potential enstrophy be conserved. Furthermore, to ensure that the system remains in statistical equilibrium, it is usual to assume equal a priori probability for all accessible (i.e., allowed by the initial E and Z) points in phase space. [This is the so-called ergodic hypothesis.] Under this assumption it can be shown that the equilibrium solutions, which represent ensemble averages, are equivalent to long time averages over a single realization.

Returning to our particular set of spectral equations (11) we note that Liouville's theorem is satisfied since there are no self-interactions (i.e., $c_{\beta\epsilon\alpha} = 0$, whenever any two indices are equal). However, as we already know, this system of equations does not

identically conserve the truncated versions of energy and potential enstrophy. To rectify this situation will require the following corrective measures: (1) setting $u_s = 0$, to ensure energy conservation and (2) projecting $\beta \cdot y$ onto our orthonormal basis [given in (9)], to ensure potential enstrophy conservation (see Appendix F). With regards to (2) we will, for the time being, simply absorb the projected $\beta \cdot y$ into h (see Appendix G).

Now, if we write $x_i = K_i \cdot \psi_i$, $H_i = f_0 \cdot h_i / H$ and $\beta_{ijl} = -c_{ijl}$ the resulting spectral equations can be expressed as in Salmon et al. (1976, equation 1.6), i.e.

$$d_t x_i = \sum_{j1} \left[\frac{K_i}{K_i K_j} \right] \beta_{ij1} x_j x_1 - \sum_{j1} \left[\frac{1}{K_i K_j} \right] \beta_{ij1} x_j H_1 \quad (95)$$

In this case the energy and potential enstrophy are given by

$$\sum_i x_i^2 = 2E \quad \text{and} \quad \sum_i K_i^2 x_i^2 - 2 \sum_i K_i H_i x_i + \sum_i H_i^2 = 2Z, \quad (96a,b)$$

respectively. Under the various assumptions outlined earlier, it can be shown that the expectation values (denoted with bold angle brackets) of x_i and $E_i = x_i^2$ at statistical equilibrium are

$$\langle x_i \rangle = \beta_0 K_i (\alpha_0 + \beta_0 K_i^2)^{-1} H_i \quad (97a)$$

$$\text{and} \quad \langle x_i^2 \rangle = \frac{1}{2} (\alpha_0 + \beta_0 K_i^2)^{-1} + \beta_0^2 K_i^2 (\alpha_0 + \beta_0 K_i^2)^{-2} H_i^2 \quad (97b)$$

where $\alpha_0 + \beta_0 K_i^2$ is necessarily positive for every i . The parameters α_0 and β_0 in (97) are determined by solving the two coupled equations which arise after equating the expectations for the total energy and potential enstrophy to the invariant values, E and Z , i.e.

$$\sum_i \langle E_i \rangle = 2E \quad \text{and} \quad \sum_i \langle Z_i \rangle = 2Z \quad (98a,b)$$

Equations 98a, b will be solved using the Newton-Raphson method at the $M = N = 15$ truncation level, corresponding to our numerical simulations.

A few interpretational comments regarding (97a,b) are in order. First, we note that since ensemble averages are equivalent to long-time averages, the right-hand side of (97a) represents the stationary part of the streamfunction (Sawford and Frederiksen, 1983). Furthermore, given high enough resolution $\beta_0 > 0$ (since $\alpha_0 + \beta_0 k_1^2 > 0 \forall 1$) so that the streamfunction and topography are positively correlated. In other words, if the flow contains small enough scales the equilibrium streamfunction is such that we will find high pressure over mountains and low pressure over valleys. Referring to (97b) we notice that while the expected transient part of the streamfunction is zero, the energy of the transient flow is not (as evidenced by the presence of the first term). More to the point, the first and second terms on the right hand side represent the energy in the transient and the stationary parts of the flow, respectively.

4.4.2 Numerical simulation: experiment

At this stage we remind the reader that in order to ensure the conservation of E and Z we have set $u_s = 0$ and projected βv onto the orthonormal basis (9), i.e., $\beta v = \sum \beta_1 \sqrt{2} \cos(\pi i v / D)$ (where β_1 is given in Appendix G). Assuming a linear relationship between $\bar{\psi}$ and $\bar{\theta}$ as well as a sinusoidal topography, we get for steady flow,

$$\bar{\psi} = \sum_i \bar{\psi}_i / 2 \cos(\pi i y / D) + \bar{\psi}_\alpha \cdot 2 \sin(2\pi m_\alpha x / L) \sin(\pi n_\alpha y / D) \quad (99)$$

where $\bar{\psi}_i = \beta_i / (K_i^2 - K_s^2)$ and $\bar{\psi}_\alpha = f_0 (h_\alpha / H) / (K_\alpha^2 - K_s^2)$

This equation is meant to be compared with (88) which gives $\bar{\psi}$ for the case when $u_s \neq 0$ and the planetary vorticity is a linear function in y . We emphasize that in order to relate the findings in this section to those of the previous one we intend to adjust β so that $\bar{\psi}$, as defined by (99), is as close as possible to $\bar{\psi}$, as defined by (88)

As shown in Appendix F if $\beta \approx 0.7885 \times 10^{-11} \text{ m}^{-1} \text{ s}^{-1}$, and K_s^2 has the same value as in experiment 2, then $\langle \bar{u} \rangle = - \langle \partial_y \bar{\psi} \rangle \approx 16 \text{ m s}^{-1}$. Obviously we have chosen the β -parameter so that we get the same initial westerly mean-wind as in experiment 2. Further to this, if we take $2h_\alpha / H = 0.12$ then the wavy part of $\bar{\psi}$ is also identical to that of experiment 2. The FGLD to this steady flow has $(\tau, T) \approx (4.78, 29.59)$ days. This compares very favourably with the FGLD of experiment 2, for which $(\tau, T) \approx (4.72, 28.37)$ days. As before, we will initialize the integration using this steady flow plus its FGLD, with $\delta = 2/0.02$. The initial streamfunction in this case is shown in Fig. 44a, while a scatter diagram of ψ versus Q is shown in Fig. 44b. We emphasize the fact that initially the relationship between Q and ψ is very nearly linear.

Consider Figs. 44c, d which show the evolution of the mean wind and the trajectory of the basic wave, respectively. Comparing Fig. 44c with the dashed curve of Fig. 38a [showing the evolution of $\langle u \rangle$ in experiment 2 ($\delta = 2/0.02$)] we notice immediately the strong resemblance. Although in this simulation $\langle u \rangle$ tends towards a slightly larger negative value than before, the qualitative behaviour is nearly the same. The

basic wave trajectory corresponding to experiment 2 (not shown) is also quite similar to that given in Fig. 44d. On the basis of these comparisons we can quite safely say that the dynamics governing the long term behaviour of these two simulations are for all intents and purposes the same. We will now show that the long term behaviour of experiment 4 is connected with the tendency of the truncated dynamical system to evolve towards a statistical equilibrium

4.4.3 Approach to equilibrium of the numerical simulation

To compare the long-term behaviour of the numerical simulation with statistical equilibrium it would perhaps be most appropriate to consider a time-average of say the last 50 days of the numerical simulation. Given that the simulation varies little over the last 50 days we will, instead, simply compare the simulation at $t = 100$ days with the corresponding statistical equilibrium, as done in Figs 45a, b, respectively. As can be seen, the equilibrium and simulated streamfunctions are quite similar. More specifically, both solutions are characterized by a strong easterly flow which departs southward over the mountain and northward over the valley.

As further evidence that the simulation is evolving towards statistical equilibrium we present the energy spectra for the simulation ($t = 100$) and the statistical equilibrium in Fig 45c. The peak in the equilibrium zonal spectrum at $m_y = 2$ is related to the fact the energy is enhanced on the topographic scale [see the second term on the right of (97b)]. Comparing the two sets of curves we find the closest agreement at the largest scales (i.e., for $m, n < 2$), which suggests that the large scales are the first to equilibrate. The agreement is the smaller

scales is not nearly as good but close enough, to suggest that the simulation is indeed approaching equilibrium energy spectrum throughout. Finally, we present Table 5 which compares a few quantities taken from the simulation and the equilibrium solution, respectively. Note that a comparison is also made between the equilibrium solutions for $\delta = 2/0.02$ and $\sqrt{0.02}$. In this connection, we comment that the similarity between these two solutions is consistent with our findings in experiment 2, where we considered both $\delta = 2/0.02$ and $\delta = \sqrt{0.02}$.

4.5 Discussion

In this chapter we have considered the inviscid *nonlinear* stability of topographically forced planetary flows consisting of a constant westerly mean zonal flow and a wave on the scale of the sinusoidal topography. The basic flows exist as finite-amplitude steady state solutions of the barotropic vorticity equation (defined on a midlatitude β -plane channel). The nonlinear stability of these flows was tested by means of numerical integration of a spectral analogue of the model equation where the initial conditions consisted of each steady solution plus a small amplitude disturbance. In each case the small amplitude disturbance represented the equilibrium flow's fastest-growing linear disturbance. Calculations were made using sufficient resolution to ensure the accuracy of the initial linear eigenmodes as well as the time-dependent solutions.

As alluded to already, each of the equilibrium flows tested was found to be linearly unstable. In the first experiment, involving a weakly unstable steady flow, the linear analysis revealed that the instability was of the Rayleigh type, which relied on zonal shears in the basic flow (as opposed to a form drag or resonant interaction mechanism). In addition, it was discovered that the fastest-growing linear disturbance was dominated by two wave components whose relative phase relationship was the key to the linear instability. In the subsequent simulation it was revealed that nonlinear interactions between the mean zonal flow, the basic wave and the disturbance resulted in changes in this unstable phase relationship leading to a temporary halt in the disturbance growth. At the time of this temporary stabilization the energy of the initially small amplitude disturbance

was found to comprise a significant fraction of the total energy. The fact that the disturbance was able to achieve such a large amplitude (at the expense of the mean zonal flow) indicates that weakly nonlinear theory, such as that used by Deininger (1981), would not be capable of explaining the behaviour of this simulation.

One of the more interesting features of the simulation just described was the appearance, shortly after the initial stabilization of the linear disturbance, of a 15-day mean flow vacillation. This vacillation, which eventually came to dominate the overall picture, was rationalized using a simple linear interference theory like that proposed by Lindzen et al. (1982). More specifically, it was argued that the vacillation arose from the periodic interference between a forced stationary wave on the scale of the topography and a free travelling Rossby wave (with the same horizontal wavenumber). The vacillation seen in our model is interesting since similar vacillations have been found to exist in rotating annulus experiments as well as in the atmosphere (Lindzen et al., 1982). Another interesting feature of the model simulation was the overall tendency of initial westerly mean zonal flow to decrease.

The second simulation described in this chapter involved an equilibrium flow which was much more unstable than the first. (The fastest-growing linear disturbance had an e-folding time of approximately five days*) As in the previous experiment, in this simulation the mean zonal flow was found to decrease as time passed. In fact, after only four e-folding times of the initial disturbance the channel averaged zonal flow changed direction entirely (going from westerly to easterly). Following this dramatic reversal the flow

eventually settled down to a quasi-stable state representing a strong easterly zonal flow being diverted southward over mountains and northward over valleys. We note that additional experiments involving a larger amplitude initial disturbance and a Gaussian topography confirmed the generality of this sort of behaviour. [A similar behaviour as we encountered here was found by Edelmann (1972) who computed stationary solutions of the shallow water equations by means of so-called iterated time-averaging.]

In many ways the asymptotic behaviour of the simulation just described was found to be reminiscent of the statistical equilibria derived by Salmon et al. (1976). In order to check the extent to which the behaviour of this simulation can be understood as an approach towards statistical equilibrium, the latter was explicitly determined using the same initial condition and resolution as that used in the integration. Following a comparison of the simulation and the corresponding statistical equilibrium it was discovered that indeed many aspects of the numerical simulation could be interpreted as a manifestation of the system evolving towards statistical equilibrium. We believe that this result strengthens the case for utilizing the methods of statistical mechanics when testing the stability of equilibrium solutions involving flow over topography.

CHAPTER 5

SUMMARY AND CONCLUSIONS

This study has been concerned with the stability of free and topographically forced planetary waves. Instability theory has long been central to our understanding of the fluctuations in the large-scale circulation of the atmosphere, but it was only relatively recently that these methods have been applied to flows which vary in both horizontal directions. Although instability studies involving parallel flows are of interest (as evidenced by the plethora of such studies contained in the literature) their relevance to naturally occurring flows, such as the atmosphere, is somewhat questionable. [As discussed in Chapter 1 the time-averaged state of the atmosphere is characterized by a longitudinally varying flow as a consequence of topographic and local thermal forcing.] Investigations dealing with the stability of parallel flows are woefully inadequate, for example, when it comes to describing the dynamics involved in regional cyclogenesis. In this investigation, by way of coming a little closer to reality, we considered the stability of basic flows which vary in two horizontal directions.

In Chapter 2, after formulating our mathematical model, we derived a particular class of exact steady-state solutions to the model equation (i.e., the barotropic vorticity equation). These solutions involved the diversion of a westerly mean zonal flow (i.e., where the average is around latitude circles) by an idealized sinusoidal topography. It has been shown in Derome (1984) that these particular finite-amplitude solutions are, in the absence of dissipation, the same as those of Charney and Eliassen (1949) except that the latter were obtained as

solutions to a corresponding linear problem. Finally, in the last section of Chapter 2 we derived a set of spectral equations which would enable us to study certain aspects of the linear and nonlinear stability of these solutions which could not be studied analytically.

In Chapter 3 we investigated the linear stability properties of the equilibrium flows derived in the previous chapter. Here the equilibrium flows were perturbed by infinitesimal perturbations and their stability judged on the basis of whether or not the perturbations had nonzero growth rates. Section 3.1 constituted a full parametric analysis of the linear stability of both free and forced equilibrium flows of this sort. In this section equilibrium flows were studied having the gravest possible meridional scale allowed by the β -plane channel and a zonal wavenumber of either 1 or 2. The forced zonal-wavenumber-1 flow was found to have three major regions of instability in parameter space, two of which had stationary growing perturbations. The free Rossby wave of that scale was stable for all amplitudes. The forced zonal wavenumber two wave had two adjacent instability domains, one on each side of the resonant mean zonal wind. The free wave became unstable for sufficiently large amplitudes. The results of this section were interpreted through the use of a severely truncated spectral model and were related to those of previous studies with infinite β -planes. In this section we also reported the existence of a travelling subresonant topographic instability which seems to have gone unnoticed in previous studies.

It was revealed in the stability analysis of Section 3.1 that the equilibrium flows were unstable to shear (Rayleigh), resonant interaction and topographic (form drag) instabilities. Following this,

in Section 3.2 the dependence of the meridional structure of growing perturbations on topographic instability was studied in more detail. In this analysis perturbations were taken consisting of an arbitrary mean zonal part and a wavy part which had the same zonal wavenumber as the forcing but arbitrary meridional structure. This configuration allowed us to: (1) isolate those instabilities which depended crucially on form drag and (2) investigate non-topographic effects on topographic instability such as those arising from the convergence of Reynolds stresses. (Perturbations involving an arbitrary zonal structure were also studied and it was found that, qualitatively speaking, the results were unchanged.) Following a numerical analysis it was discovered, in particular, that unstable long waves (i.e., those with zonal wavelength longer than their meridional wavelength) exist only under superresonant conditions. This was found to contradict some previous results, based on various *ad hoc* assumptions, which suggest that long waves are unstable only when the flow is subresonant. Further, this model revealed the existence of some interesting travelling instabilities which were shown to depend both on form drag and Reynolds stresses. (In that these two mechanisms temporally alternate in supplying the perturbation, the energy required to maintain its exponential growth.)

In Section 3.3 the linear instability of a weakly non-zonal basic flow was investigated numerically using the spectral method and analytically via WKB theory. Part of the motivation for this study lay in the recent success of Frederiksen (1983) in studying the stability properties of the time-averaged Northern Hemisphere flows for the months of January and July 1978. Frederiksen found a good agreement between the observed geographical distribution of synoptic scale eddy heat flux

and the distribution predicted by his numerically-determined fastest-growing mode. Due, however, to the complexity of his model he was not able to fully comment on the basic dynamical mechanisms responsible for the local growth of his idealized zonally-varying flows. Our barotropic β -channel model, on the other hand, is simple enough that a WKB analysis, in conjunction with some techniques developed by Pierrehumbert (1984), could be used to shed some light on this problem.

Our numerical analysis revealed that the slowest-growing eigenmode to a particular weakly non-zonal basic flow was stationary, on the scale of the topography and depended crucially on a form drag mechanism (of the sort illuminated in Section 3.2). The fastest-growing eigenmode, on the other hand, did not involve a form drag mechanism but depended, rather, on the presence of local shears inherent in the basic flow itself. A closer look at this mode revealed a simple meridional structure which was strongly modulated in the zonal direction. The peak in the modulation pattern was associated with an easterly jet in the basic flow which was particularly unstable as a result of the beta effect. A secondary maximum in the modulation pattern was associated with regions of basic flow confluence and diffluence. The corresponding analytic solution, acquired using the WKB approximation, correctly reproduced the location and shape of the unstable wavepacket but overestimated the frequency. It was suggested that had the basic flow been more slowly varying in the zonal direction a better agreement in the frequency would also have been obtained.

Till Chapter 4 we had only considered the linear instability properties of free and forced waves. Although linear theory is useful in predicting the initial behaviour of a small disturbance superimposed on

an unstable basic flow it is of little use once the former achieves any appreciable amplitude. In Chapter 4, on the other hand, we used a fully nonlinear spectral numerical model to study the evolution of a number of disturbances past the point where the linearization procedure failed. Three basic experiments were performed, the first of which involved a basic flow which was only weakly unstable. In the latter it was found that the basic flow was nonlinearly unstable in the sense that the initially very small amplitude disturbance grew nearly as large as the basic wave itself. In this connection, and in contrast to the nonlinear equilibration mechanism proposed by Deininger (1981), it was discovered that the growth experienced by the disturbance in the early stages of the simulation was largely at the expense of the energy of the mean zonal part of the basic flow rather than the basic wave itself. The crucial role of the topography in this redistribution of energy between the mean zonal flow and the eddies was noted. One of the more interesting features of this simulation was a mean flow vacillation which appeared half way into the simulation and which came to dominate the flow thereafter. This vacillation was found to be the consequence of the periodic interference between two waves with the same horizontal wavenumber (that of the topography) but different phase speeds.

The second experiment described in Chapter 4 involved a basic flow which was initially much more unstable to linear disturbances. Once again, the basic flow was found to be nonlinearly unstable. Moreover, as in the previous simulation the mean zonal flow decreased dramatically with time. In fact, in this particular simulation the channel-averaged flow eventually reversed direction: going from westerly to easterly. Following this reversal, the flow appeared to settle into a quasi-steady

state, characterized by an easterly mean flow which was diverted southward over mountains and northward over valleys. A similar sort of long-term behaviour was found in the third experiment of Chapter 4 and which involved a more complicated topography (i.e., nonsinusoidal). The various connections between these results and those of some previous investigators (i.e., Kasahara, 1966; Edelman, 1972; Egger and Metz, 1981; Yoden, 1987), who used models with varying degrees of simplification, was noted. Finally, at the end of Chapter 4 we exploited the methods of statistical mechanics in order to rationalize the asymptotic behaviour of some of our simulations. From this analysis it was concluded that the long-term behaviour of the simulations was consistent with an approach towards statistical equilibrium.

APPENDIX A

DETAILS OF THE DISPERSION RELATIONSHIP

The various terms in the dispersion relationship [Eq. (26)] associated with the severely truncated model are given explicitly below.

a Wave dispersion

$$\omega_{\beta} = \frac{2\pi}{L^m_{\beta}} (u_s - \beta/K_{\beta}^2) \quad (\text{A } 1\text{a})$$

$$\omega_{\epsilon} = \frac{2\pi}{L^m_{\epsilon}} (u_s - \beta/K_{\epsilon}^2) \quad (\text{A } 1\text{b})$$

b Wave interaction

$$A_{\beta\epsilon} = (u_s - \beta/K_{\beta}^2)(u_s - \beta/K_{\epsilon}^2)(\bar{\psi}_{\alpha}^c c_{\beta\alpha\epsilon}/u_s)^2 \quad (\text{A } 2\text{a})$$

$$A_{\gamma\beta} = (u_s - \beta/K_{\gamma}^2)(u_s - \beta/K_{\beta}^2)(\bar{\psi}_{\alpha}^c c_{\gamma\alpha\beta}/u_s)^2 \quad (\text{A } 2\text{b})$$

APPENDIX B

DECOUPLING OF THE STABILITY MATRIX

As mentioned in subsection 3 2 3, the stability matrix decouples into two submatrices. We will show here that this is related to the symmetries present in the perturbation equations.

The equation for \bar{u}' , the mean zonal perturbation wind, is obtained by zonally averaging (39) and takes the form

$$\partial_t \bar{u}' - \partial_y [\bar{v}_s (\Delta + K_s^2) \psi'^*] - \partial_x [(f_o/H) h_s \partial_x \psi'^*] = 0 \quad (B 1)$$

while the equation for ψ'^* (deviation from the zonal average), obtained by subtracting (B 1) from (39), can be written as

$$\partial_t \Delta \psi'^* + u_s (\Delta + K_s^2) \partial_x \psi'^* - \bar{v}_s (\Delta + K_s^2) \bar{u}' + \bar{u}' \partial_x [(f_o/H) h_s] = 0 \quad (B 2)$$

when only one zonal harmonic is allowed in the x direction. In the following discussion, we will call a function even (odd) if it has the stated parity with respect to the middle of the channel ($y = D/2$) and we will take h_s , and hence \bar{v}_s [see (40)], to be even. By inspection of (B.1) and (B.2) we see that solutions with the following parities are possible: (a) ψ'^* and \bar{u}' both even [i.e., n odd in the $\sin(n\pi y/D)$ of ψ'^* and \bar{u}'] and (b) ψ'^* and \bar{u}' both odd (n even). Solutions of the first type have a \bar{u}' with a nonzero channel average and must involve the form drag mechanism; they are associated with the A_T matrix. Solutions of the second type have a \bar{u}' with a zero channel average and may or may not involve the form drag mechanism, they are associated with the A_R matrix.

APPENDIX C

TOPOGRAPHIC INSTABILITY: THE DISPERSION RELATIONSHIP

a. Interaction Coefficients

The interaction coefficients in (50) are defined as follows

$$\hat{c}_{\theta\beta} = C_0/3, \quad \hat{c}_{\theta\epsilon} = -C_0/15, \quad \hat{c}_{\phi\beta} = -C_0/5 \quad \text{and} \quad \hat{c}_{\phi\epsilon} = 27C_0/35 \quad (\text{C.1})$$

with $C_0 = \frac{16\sqrt{2}\pi}{LD}$ (D and L are the channel width and length, respectively)

b. The frequency near linear resonance

To obtain an approximate expression for ω , valid near linear resonance, we take

$$\Delta_\beta = K_s^2 - K_\beta^2 \approx 0 \quad (\text{C.2})$$

Writing the basic state amplitude in terms of Δ_β , i.e.,

$$\tilde{\psi}_\alpha = - (f_0 \cdot h_\alpha / \hbar) / \Delta_\beta \quad (\text{C.3})$$

we note that $\Delta_\beta > 0$ implies subresonant flow and $\Delta_\beta < 0$ superresonant flow. The fact that $\tilde{\psi}_\alpha \rightarrow \infty$ as $\Delta_\beta \rightarrow 0$ will allow us to neglect a number of terms in (50) leading to a simple final result. For future reference we note also that, near linear resonance,

$$\Delta_\theta > 0, \quad \Delta_\epsilon < 0,$$

(C.4)

and $\Delta_\phi < 0$ if $\delta_1 = D/L < \sqrt{2}$ ($\Delta_\phi \geq 0$ if $\delta_1 \geq \sqrt{2}$)

For the channel dimensions used in this study $\delta_1 \approx 0.14 \leq \sqrt{2}$ so that $\Delta_\phi < 0$ (We mention that channel widths for which $\delta_1 \geq \sqrt{2}$ are unrealistically large.)

The solution to (50) can be written

$$\omega^2 = \frac{b}{2} \pm \frac{b}{2} \left[1 - 4c/b^2 \right]^{1/2} \quad (C 5)$$

where, near resonance,

$$b \approx \hat{b} \cdot \tilde{\psi}_\alpha^2 = \left[\frac{\Delta_\theta}{K_\theta^2} \hat{c}_{\theta\epsilon}^2 + \frac{\Delta_\phi}{K_\phi^2} \hat{c}_{\phi\epsilon}^2 \right] \frac{\Delta_\epsilon}{K_\epsilon^2} \tilde{\psi}_\alpha^2 \quad (C 6a)$$

$$\text{and } c \approx \hat{c} \Delta_\beta \tilde{\psi}_\alpha^4 = \left[\frac{\Delta_\theta \Delta_\phi \Delta_\epsilon}{K_\theta^2 K_\phi^2 K_\epsilon^2 K_\beta^2} (\hat{c}_{\theta\beta} \hat{c}_{\phi\epsilon} - \hat{c}_{\theta\epsilon} \hat{c}_{\phi\beta})^2 \right] \Delta_\beta \tilde{\psi}_\alpha^4 \quad (C 6b)$$

Since $4c/b^2 = 4(\hat{c}/\hat{b}^2) \Delta_\beta \rightarrow 0$ as $\Delta_\beta \rightarrow 0$ the radicand in (C 5) is positive implying that unstable near resonant flow is necessarily stationary (i.e., ω^2 is real and negative). To choose the appropriate sign in (C 5) consider the ratio of the terms in the square bracket of (C 6a) and note that

$$\delta_2 = \lim_{\Delta_\beta \rightarrow 0} \left[(\Delta_\theta \hat{c}_{\theta\epsilon}^2 / K_\theta^2) / (\Delta_\phi \hat{c}_{\phi\epsilon}^2 / K_\phi^2) \right] = \frac{49}{729} \left[1 - (2/\delta_1^2) \right]^{-1} \quad (C 7)$$

which is approximately equal to 6.78×10^{-4} when $\delta_1 = 0.14$. Since $|\delta_2| \ll 1$ we can write

$$b \approx \frac{\Delta_\phi \Delta_\epsilon}{K_\phi^2 K_\epsilon^2} \hat{c}_{\phi\epsilon}^2 \tilde{\psi}_\alpha^2 \quad (C 8)$$

It follows that $b > 0$ (since $\Delta_\phi \Delta_\epsilon > 0$), which in turn, implies that the negative sign in (C.5) must be taken if ω^2 is to be negative. From here it is a simple matter to show that for $\Delta_\beta \approx 0$

$$\omega^2 \approx c/b, \quad (C.9)$$

which is equivalent to (52)

The following ratio is used to obtain (55)

$$\delta_3 = \lim_{\Delta_\beta \rightarrow 0} \left[(\Delta_{\theta_\lambda} \hat{C}_{\theta\beta}^2 / K_\theta^2) / (\Delta_\phi \hat{C}_{\phi\beta}^2 / K_\phi^2) \right] = \frac{25}{9} \left[1 - (2/\delta_1^2) \lambda \right]^{-1} \quad (C.10)$$

which is approximately equal to - 0 028 when $\delta_1 \approx 0 14$.

APPENDIX D

DETAILS OF THE TWO AND THREE TERM SYSTEMS

a. Three-term system

The equations governing ϕ_1 , ϕ_3 and ϕ_5 are as follows

$$\begin{aligned} (\omega + a) \cdot \phi_1 & - b \cdot \phi_3 & - & 0 \\ - c \phi_1 + (\omega + d) \cdot \phi_3 & - e \cdot \phi_5 & - & 0 \\ & - f \phi_3 + (\omega + g) \phi_5 & - & 0 \end{aligned} \quad (D 1)$$

where $a = k \cdot [u_s + (u_w/2)] \cdot (K_s^2 - K_1^2)/K_1^2$ $e = k u_w (K_s^2 - K_5^2)/(2 K_3^2)$

$b = k u_w \cdot (K_s^2 - K_3^2)/(2 K_1^2)$ $f = k u_w (K_s^2 - K_3^2)/(2 K_5^2)$

$c = k \cdot u_w \cdot (K_s^2 - K_1^2)/(2 K_3^2)$ $g = k u_s (K_s^2 - K_5^2)/K_5^2$

$d = k u_s \cdot (K_s^2 - K_3^2)/K_3^2$

also $K_p^2 = k^2 + n_p^2$ and $n_p = p \cdot \pi$ for $p = 1, 3$ and 5

Setting the determinant of the coefficients of (D 1) to zero leads to an equation for ω [see also (73)], i.e.

$$\omega^3 + B \cdot \omega^2 + C \omega + D = 0 \quad (D 2)$$

where $B = a + d + g$, $C = d g + a d + a g - b e - b c$

and $D = a d g - a f e - c g b$

Inverting (D.2) leads to (77) with the a_n 's and b_n 's defined as follows

$$a_0 = n_1^2 n_3^2 n_5^2$$

$$a_1 = [u_s + (u_w/2)] n_3^2 n_5^2 (K_s^2 - n_1^2) + u_s n_1^2 n_3^2 (K_s^2 - K_3^2) + u_s n_1^2 n_3^2 (K_s^2 - K_5^2)$$

$$a_2 = [u_s(u_s + (u_w/2)) - (u_w^2/4)] n_5^2 (K_s^2 - n_1^2) (K_s^2 - n_3^2)$$

$$+ [u_s^2 - (u_w^2/4)] n_1^2 (K_s^2 - n_3^2) (K_s^2 - n_5^2)$$

$$+ u_s [u_s + (u_w/2)] n_3^2 (K_s^2 - n_1^2) (K_s^2 - n_5^2)$$

$$a_3 = ([u_s + (u_w/2)]^2 [u_s - (u_w/2)] - [u_s u_w^2/4]) (K_s^2 - n_1^2) (K_s^2 - n_3^2) (K_s^2 - n_5^2)$$

$$a_4 = [u_s(u_s + (u_w/2)) - (u_w^2/4)] [(K_s^2 - n_1^2) (K_s^2 - n_3^2) - n_5^2 (2K_s^2 - n_1^2 - n_3^2)]$$

$$+ [u_s^2 - (u_w^2/4)] [(K_s^2 - n_3^2) (K_s^2 - n_5^2) - n_1^2 (2K_s^2 - n_3^2 - n_5^2)]$$

$$+ u_s [u_s + (u_w/2)] [(K_s^2 - n_1^2) (K_s^2 - n_5^2) - n_3^2 (2K_s^2 - n_1^2 - n_5^2)]$$

$$a_5 = [(u_s u_w^2/4) - (u_s + (u_w/2))^2 (u_s - (u_w/2))] [(K_s^2 - n_1^2) (K_s^2 - n_3^2)$$

$$+ (2K_s^2 - n_1^2 - n_3^2) (K_s^2 - n_5^2)]$$

$$a_6 = - [3u_s^2 + u_s u_w - (u_w^2/2)] [2K_s^2 - n_1^2 - n_3^2 - n_5^2]$$

$$a_7 = [(u_s + (u_w/2))^2 (u_s - (u_w/2)) - (u_s u_w^2/4)] [3K_s^2 - n_1^2 - n_3^2 - n_5^2]$$

$$a_8 = 3u_s^2 + u_s u_w - (u_w^2/2)$$

$$a_9 = (u_s u_w^2/4) - [u_s + (u_w/2)]^2 [u_s - (u_w/2)]$$

$$b_2 = n_1^2 n_3^2 + n_1^2 n_5^2 + n_3^2 n_5^2$$

$$b_3 = [(u_s + (u_w/2))][n_3^2(K_s^2 - n_1^2) + n_5^2(K_s^2 - n_1^2 - n_3^2)]$$

$$+ u_s [n_1^2(K_s^2 - n_3^2) + n_5^2(K_s^2 - n_1^2 - n_3^2)]$$

$$+ u_s [n_1^2(K_s^2 - n_5^2) + n_3^2(K_s^2 - n_1^2 - n_5^2)]$$

$$b_4 = n_1^2 + n_3^2 + n_5^2$$

$$b_5 = [3u_s + (u_w/2)](K_s^2 - n_1^2 - n_3^2 - n_5^2)$$

$$b_6 = 1$$

$$b_7 = - [3u_s + (u_w/2)]$$

b Two-term system

1) DISPERSION RELATIONSHIP When $\phi_2 = 0$ then the equations governing ϕ_1 and ϕ_3 are obtained from (D.1) by setting $e = f = g = 0$. Similarly the two-term dispersion equation given in (74) results from (D.2) after setting $e = f = g = 0$.

2) DETERMINATION OF k_M Assuming $\omega = \omega_r + \omega_i$ where $\omega_i \neq 0$ we define k_M to be the wavenumber which maximizes ω_i . To determine k_M we simply set $\partial_k \omega_i = 0$ and then search for the largest of the real positive roots of the resulting equation. The condition $\partial_k \omega_i = 0$ leads to an 8th-order algebraic equation in powers of k^2 (found easily with the aid of an algebraic manipulator) the roots of which were determined using a standard method. The coefficients of this equation are (note that C_n multiplies k^{2n} , $K_s^2 = \beta/u_s$ and $K_w^2 = \beta/u_w$)

$$c_8 = 5$$

$$c_7 = 20n_1^2 + 20n_3^2$$

$$c_6 = -5K_S^4 + 30n_3^4 + 30n_1^4 - 4n_3^2K_S^2 + 4n_3^2K_W^2 - 6n_1^2K_S^2 - 4n_1^2K_W^2 + 80n_1^2n_3^2$$

$$c_5 = 20n_3^6 - 8n_3^4K_S^2 + 8n_3^4K_W^2 + 20n_1^6 - 12n_1^4K_S^2 - 8n_1^4K_W^2 + 120n_1^4n_3^2 + 12n_3^2K_S^4$$

$$- 8n_3^2K_W^2K_S^2 - 8n_1^2K_S^4 + 120n_1^2n_3^4 + 8n_1^2K_W^2K_S^2 - 40n_1^2n_3^2K_S^2$$

$$c_4 = 5n_3^8 - 4n_3^6K_S^2 + 4n_3^6K_W^2 - 10n_3^4K_S^4 - 12n_3^4K_W^4 - 20n_3^4K_W^2K_S^2 + 5n_1^8 - 6n_1^6K_S^2$$

$$- 4n_1^6K_W^2 + 80n_1^6n_3^2 - 3n_1^4K_S^4 - 12n_1^4K_W^4 + 180n_1^4n_3^4 + 8n_1^4K_W^2K_S^2 - 72n_1^4n_3^2K_S^2$$

$$- 8n_1^4n_3^2K_W^2 + 80n_1^2n_3^6 - 68n_1^2n_3^4K_S^2 + 8n_1^2n_3^4K_W^2 - 12n_1^2n_3^2K_S^4 + 24n_1^2n_3^2K_W^4$$

$$+ 12n_1^2n_3^2K_W^2K_S^2$$

$$c_3 = -4n_3^6K_S^4 - 16n_3^6K_W^4 - 16n_3^6K_W^2K_S^2 + 20n_1^8n_3^2 - 16n_1^6K_W^4 + 120n_1^6n_3^4 - 40n_1^6n_3^2K_S^2$$

$$+ 120n_1^4n_3^6 - 120n_1^4n_3^4K_S^2 + 4n_1^4n_3^2K_S^4 + 16n_1^4n_3^2K_W^4 + 16n_1^4n_3^2K_W^2K_S^2 + 20n_1^2n_3^8$$

$$- 40n_1^2n_3^6K_S^2 + 16n_1^2n_3^4K_W^4$$

$$c_2 = -n_3^8K_S^4 - 4n_3^8K_W^4 - 4n_3^8K_W^2K_S^2 - 4n_1^8K_W^4 + 30n_1^8n_3^4 - 4n_1^8n_3^2K_S^2 + 4n_1^8n_3^2K_W^2 + 80n_1^6n_3^6$$

$$- 68n_1^6n_3^4K_S^2 + 8n_1^6n_3^4K_W^2 + 4n_1^6n_3^2K_S^4 - 8n_1^6n_3^2K_W^4 - 4n_1^6n_3^2K_W^2K_S^2 + 30n_1^4n_3^8$$

$$- 72n_1^4n_3^6K_S^2 + 8n_1^4n_3^6K_W^2 + 18n_1^4n_3^4K_S^4 + 24n_1^4n_3^4K_W^4 + 12n_1^4n_3^4K_W^2K_S^2 - 6n_1^2n_3^8K_S^2$$

$$- 4n_1^2n_3^8K_W^2 + 4n_1^2n_3^6K_S^4 - 8n_1^2n_3^6K_W^4 - 4n_1^2n_3^6K_W^2K_S^2$$

$$c_1 = 20n_1^8n_3^6 - 8n_1^8n_3^4K_S^2 + 8n_1^8n_3^4K_W^2 + 20n_1^6n_3^8 - 40n_1^6n_3^6K_S^2 + 8n_1^6n_3^4K_S^4 - 8n_1^6n_3^4K_W^2K_S^2$$

$$- 12n_1^4n_3^8K_S^2 - 8n_1^4n_3^8K_W^2 + 12n_1^4n_3^6K_S^4 + 8n_1^4n_3^6K_W^2K_S^2$$

$$c_0 = 5n_1^8n_3^8 - 4n_1^8n_3^6K_S^2 + 4n_1^8n_3^6K_W^2 + 4n_1^8n_3^4K_W^4 - 6n_1^6n_3^8K_S^2 - 4n_1^6n_3^8K_W^2 + 4n_1^6n_3^6K_S^4$$

$$- 8n_1^6n_3^6K_W^4 - 4n_1^6n_3^6K_W^2K_S^2 + n_1^4n_3^8K_S^4 + 4n_1^4n_3^8K_W^4 + 4n_1^4n_3^8K_W^2K_S^2$$

Appendix E

$\langle u \rangle$ in the numerical model ($h = 0$)

In this appendix we will show that in the absence of topography (i.e., $h = 0$) the channel-averaged zonal flow, $\langle u \rangle$, is conserved only in the limit of infinite meridional resolution. To begin we recall (86) and note that

$$F_\alpha(y=D) - F_\alpha(y=0) = \begin{cases} 0 & \text{for } n_\alpha \text{ even} \\ -2/2 & \text{for } n_\alpha \text{ odd} \end{cases} \quad (\text{E.1})$$

where F_α denotes a mean zonal basis function of the form $\sqrt{2} \cos(\pi n_\alpha y/D)$

It follows, therefore, that in the numerical model

$$d_t \langle u \rangle = -2/2 \sum_{\beta < \epsilon} (K_\epsilon^2 / K_\alpha^2) \psi_\beta \psi_\epsilon c_{\beta\epsilon\alpha} = -2/2 \sum_\alpha K_\alpha^{-2} \sum_{\beta\epsilon} K_\epsilon^2 \psi_\beta \psi_\epsilon c_{\beta\epsilon\alpha} \quad (\text{E.2})$$

where n_α is odd. We also note that $c_{\beta\epsilon\alpha}$ is nonzero only when F_β and F_ϵ are both eddy basis functions and $F_\beta = F_\epsilon$. Concentrating on the inner summation on the right-most side of (E.2) we observe that: (1) each product $\psi_\beta \psi_\epsilon$ appears twice, once multiplied by $K_\epsilon^2 c_{\beta\epsilon\alpha}$ and once by $K_\beta^2 c_{\epsilon\beta\alpha}$, (2) $c_{\epsilon\beta\alpha} = -c_{\beta\epsilon\alpha}$ and (3) $c_{\beta\epsilon\alpha} = 0$ if $m_\beta \neq m_\epsilon$. It follows from (1)-(3) that

$$d_t \langle u \rangle = -2/2 \sum_{\beta < \epsilon} \psi_\beta \psi_\epsilon (n_\epsilon^2 - n_\beta^2) \sum_\alpha (c_{\beta\epsilon\alpha} / n_\alpha^2) \quad (\text{E.3})$$

where $\sum_{\beta < \epsilon}$ denotes summation over all pairs (β, ϵ) but without repetition.

The interaction coefficients, $c_{\beta\epsilon\alpha}$, can be obtained in explicit form from Appendix A of Mitchell (1982). Using our notation we get

$$c_{\beta\epsilon\alpha} = \frac{\sqrt{2}}{LD} \pi m (n_\epsilon + n_\beta) \left[\frac{1 - (-1)^{n_\epsilon + n_\beta + n_\alpha}}{n_\epsilon + n_\beta + n_\alpha} + \frac{1 - (-1)^{n_\epsilon + n_\beta - n_\alpha}}{n_\epsilon + n_\beta - n_\alpha} \right] \\ + \frac{\sqrt{2}}{LD} \pi m (n_\epsilon - n_\beta) \left[\frac{1 - (-1)^{-n_\epsilon + n_\beta + n_\alpha}}{-n_\epsilon + n_\beta + n_\alpha} + \frac{1 - (-1)^{n_\epsilon - n_\beta - n_\alpha}}{-n_\epsilon + n_\beta - n_\alpha} \right] \quad (E.4)$$

where $m = m_\epsilon = m_\beta$ and the denominators are assumed to be nonzero. Using the fact that n_α is odd we can rewrite (E.4) more compactly as

$$c_{\beta\epsilon\alpha} = \frac{\sqrt{2}}{LD} \pi m \left[1 + (-1)^{n_\epsilon + n_\beta} \right] \left\{ \frac{n_\epsilon + n_\beta}{n_\epsilon + n_\beta + n_\alpha} + \frac{n_\epsilon + n_\beta}{n_\epsilon + n_\beta - n_\alpha} \right. \\ \left. - \frac{n_\epsilon - n_\beta}{n_\epsilon - n_\beta - n_\alpha} - \frac{n_\epsilon - n_\beta}{n_\epsilon - n_\beta + n_\alpha} \right\} \quad (E.5)$$

Letting $s = n_\epsilon + n_\beta$ and $d = n_\epsilon - n_\beta$ it follows from (E.5) that

(i) when $d \neq 0$

$$\sum_{\alpha} (c_{\beta\epsilon\alpha} / n_\alpha^2) = \frac{\sqrt{2}}{LD} \pi m \left[1 + (-1)^{n_\epsilon + n_\beta} \right] \sum_{n_\alpha} \frac{1}{s} \left[\frac{1}{n_\alpha + s} - \frac{1}{n_\alpha - s} \right] \\ - \frac{1}{d} \left[\frac{1}{n_\alpha + d} - \frac{1}{n_\alpha - d} \right] \quad (E.6)$$

(ii) when $d = 0$

$$\sum_{\alpha} (c_{\beta\epsilon\alpha} / n_\alpha^2) = \frac{\sqrt{2}}{LD} \pi m \left[1 + (-1)^{2n_\epsilon} \right] \sum_{n_\alpha} (2/n_\alpha^2) \quad (E.7)$$

Evaluating the infinite series in (E.6) and (E.7) we arrive at the following

$$\sum_{\alpha} (c_{\beta\epsilon\alpha}/n_{\alpha}^2) = \begin{cases} 0 & \text{if } n_{\epsilon} \neq n_{\beta} \\ \frac{4\sqrt{2}}{LD} \pi m (\pi^2/8) & \text{if } n_{\epsilon} = n_{\beta} \end{cases} \quad (\text{E.8})$$

It follows from (E.3) and (E.8), therefore, that $d_{\epsilon}\langle u \rangle = 0$, since for $n_{\epsilon} = n_{\beta}$ the factor $n_{\epsilon}^2 - n_{\beta}^2 = 0$ while for $n_{\epsilon} \neq n_{\beta}$ we have that $\sum (c_{\beta\epsilon\alpha}/n_{\alpha}^2) = 0$. It is crucial to understand that this result is true only if we have infinite meridional resolution. When we truncate at some meridional wavenumber $\langle u \rangle$ is not identically conserved to the extent to which $\sum (c_{\beta\epsilon\alpha}/n_{\alpha}^2) \neq 0$ when $n_{\epsilon} \neq n_{\beta}$.

As a final remark we comment that in the special case where we include only one meridional mode the channel-averaged zonal flow is indeed conserved. The latter can be seen by using $n_{\epsilon} = n_{\beta}$ in (E.3).

Appendix F

E and Z in the numerical model

In this appendix we discuss the behaviour of energy and potential enstrophy in the numerical model (recall that E and Z are analytically conserved). In particular we will show that neither of these quantities is identically conserved at finite N (where N is the number of meridional wavenumbers in the spectral expansion).

a. Energy

As concerns the energy we note that by definition:

$$E = \bar{E} + E^* = \frac{1}{2} \langle \bar{u}^2 \rangle + \frac{1}{2} \langle u^{*2} + v^{*2} \rangle \quad (\text{F.1})$$

Substituting $\bar{u} = u_s + \hat{u}(y, \tau)$ in (F.1) we get for the tendency of E :

$$d_t E = u_s \cdot d_t \langle u \rangle + \frac{1}{2} \cdot d_t \langle \hat{u}^2 + u^{*2} + v^{*2} \rangle \quad (\text{F.2})$$

From (11) it follows that the spectral versions of the two terms on the right-hand side of (F.2) can be written:

$$d_t \langle u \rangle = \sum_{\beta \in \alpha} D_\alpha K_\alpha^2 \psi_\beta \psi_\alpha c_{\beta \in \alpha} - \sum_{\beta \in \alpha} D_\alpha \psi_\beta (f_o h_\alpha / H) c_{\beta \in \alpha} \quad \text{and} \quad (\text{F.3})$$

$$d_t \langle \hat{u}^2 + u^{*2} + v^{*2} \rangle = -2u_s \sum_{\beta \in \alpha} (f_o h_\beta / H) \psi_\alpha b_{\beta \in \alpha} \quad (\text{F.4})$$

where $D_\alpha = [F_\alpha(y=D) - F_\alpha(y=0)] / K_\alpha^2$ with $F_\alpha = \sqrt{2} \cos(\pi n_\alpha y / D)$

Now, by considering the sums in (F.3) carefully (as in Appendix E) we find that when, and only when, $N \rightarrow \infty$ the first term vanishes while the second term becomes:

$$d_t \langle u \rangle = \sum_{\beta\alpha} (f_0 h_\beta / H) \psi_\alpha b_{\beta\alpha} \quad (F.5)$$

which is simply $f_0 \langle v(h/H) \rangle$. It follows after substituting (F.5) and (F.4) into (F.2) that energy is conserved as $N \rightarrow \infty$ but is, in general, not conserved when N is finite owing to the mistreatment of $d_t \langle u \rangle$ by the numerical scheme (this is true even if $h = 0$). Notice that in the case where $u_s = 0$, energy is conserved despite this latter fact.

b. *Potential enstrophy*

Now we will briefly consider the behaviour of potential enstrophy in the numerical model. Writing the potential enstrophy as

$$Z = \frac{1}{2} \langle Q^2 \rangle = \frac{1}{2} \langle (\Delta\psi + \beta y + f_0 h/H)^2 \rangle \quad (F.6)$$

it follows that

$$d_t Z = \frac{1}{2} \cdot d_t \langle (\Delta\psi)^2 \rangle + \beta d_t \langle u \rangle + f_0 \cdot d_t \langle \Delta\psi(h/H) \rangle \quad (F.7)$$

After inspecting (F.7) we conclude that just as E was not conserved for finite values of N neither is Z , in part due to the second term in (F.7). It is found, however, that in the special case where $u_s = 0$ and $\beta = 0$ (or where βy is projected onto the set of basis functions) potential enstrophy is identically conserved in the numerical model.

Despite the fact that E and Z are not identically conserved numerically, we have found by experience, that they are nearly conserved at moderate meridional resolutions (say, $N \geq 15$)

APPENDIX G

E AND Z IN THE STATISTICAL MECHANICAL MODEL

a Projection of $\beta \cdot y$ onto our orthonormal basis

As discussed in Appendix F, given our choice of basis functions (9) E and Z are not, in general, identically conserved numerically for a finite N. However, E and Z are conserved numerically when (1) $u_s = 0$ (i.e. the mean-wind vanishes at the walls) and (2) when $\beta \cdot y$ is projected onto our orthonormal basis. With regards to the latter we write

$$\beta \cdot y = \sum_1 \beta_1 \sqrt{2} \cos(\pi i y / D) \quad (G 1)$$

where $\beta_1 = \begin{cases} -2\sqrt{2}\beta D / \pi i^2 & \text{when } i \text{ is odd} \\ 0 & \text{when } i \text{ is even} \end{cases}$

b Steady channel-averaged flow, $\langle \tilde{u} \rangle$

Given the constant of proportionality K_s^2 [in (4)] then $\langle \tilde{u} \rangle = -\langle \partial_y \tilde{\psi} \rangle$ can be written (assuming $\bar{h} = 0$),

$$\langle \tilde{u} \rangle = \frac{2\sqrt{2}}{D} \sum_1 \beta_1 / (k_i^2 - K_s^2) \quad (G 2)$$

where $k_i = \pi i / D$. As discussed in the text it is our objective to specify $\langle \tilde{u} \rangle$ and K_s and find β . To this end we simply substitute (G.1) into (G.2) and solve for β , with the result that (for i odd)

$$\beta = \langle \tilde{u} \rangle \cdot \left[\frac{8D^2}{\pi^4} \sum_1 (i^2 (\hat{K}_s^2 - i^2))^{-1} \right]^{-1} \text{ with } \hat{K}_s^2 = K_s^2 / (\pi/D)^2. \quad (G 3)$$

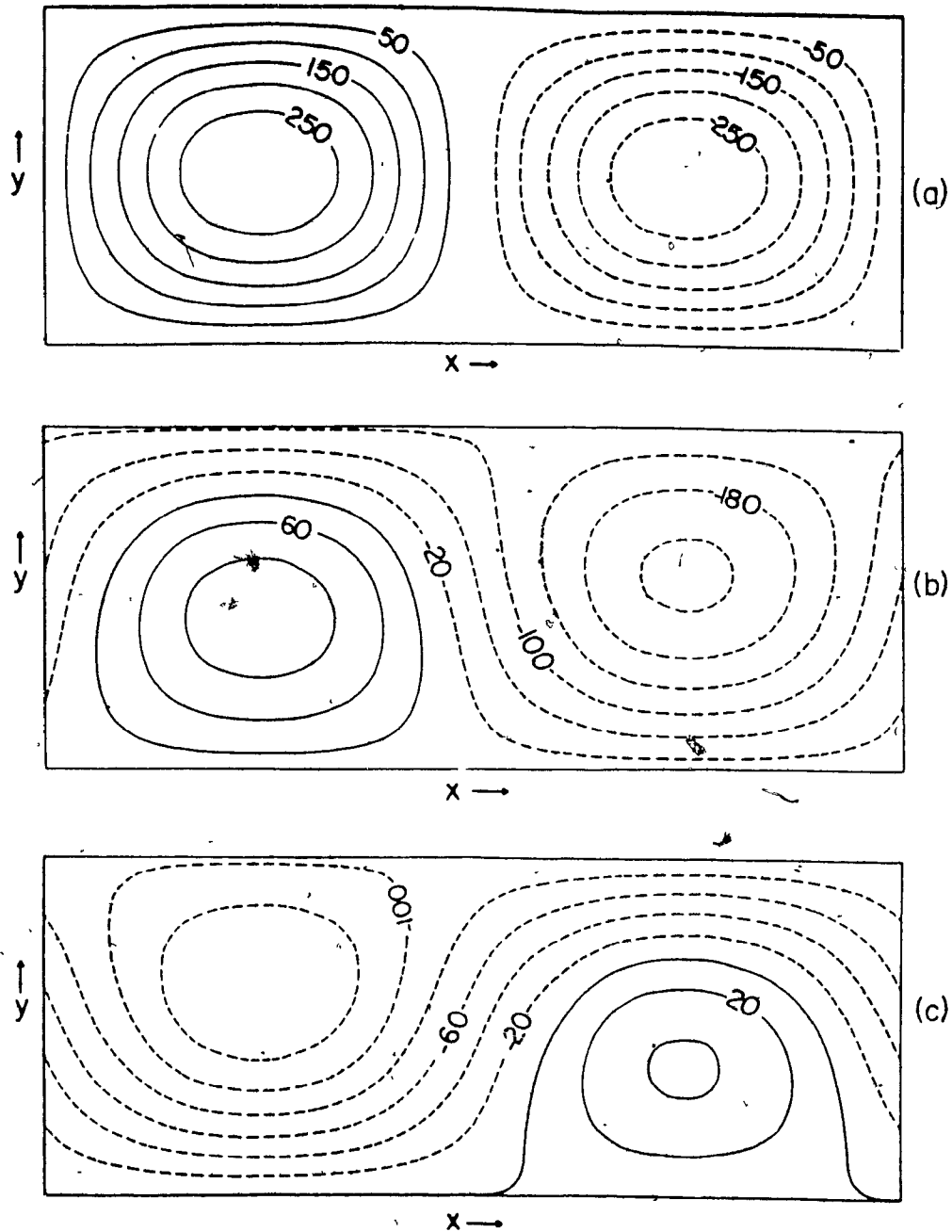


Figure 1 Super and subresonant flows.

- (a) Topography in meters: $\alpha = (1, 1)$, $2h_\alpha/H = 0.03$;
- (b) superresonant flow: $u_s = 25$ m/s;
- (c) subresonant flow: $u_s = 23$ m/s.

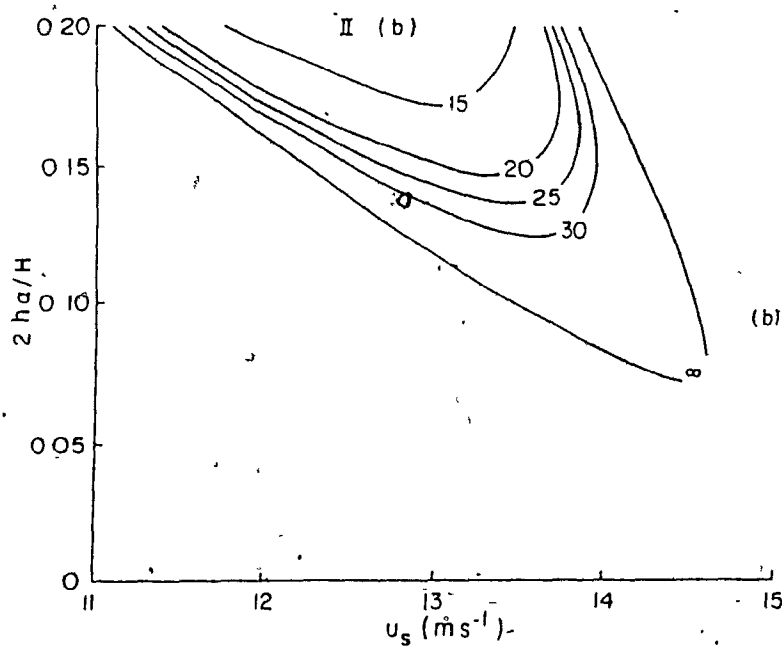
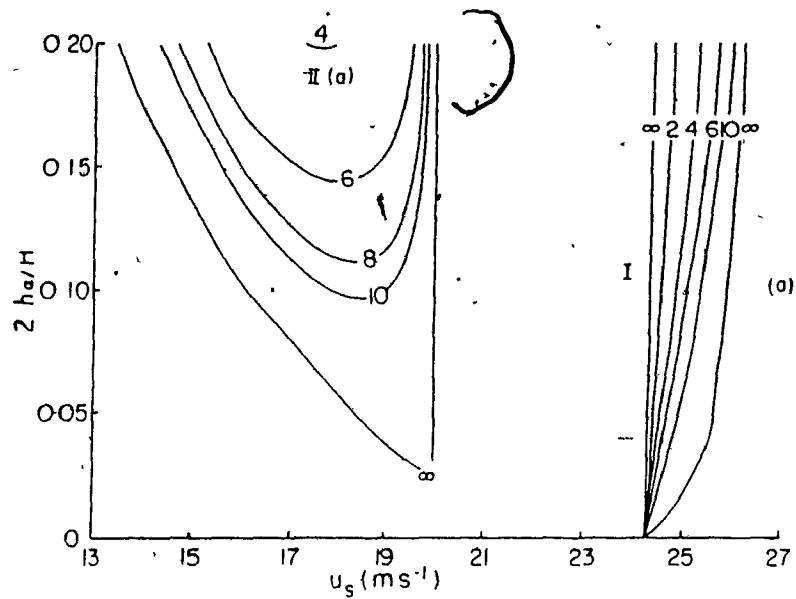


Figure 2 Contours of e-folding time in days for the fastest-growing perturbations to zonal-wavenumber-1 flows.

- (a) Regions I and II(a);
- (b) region II(b).

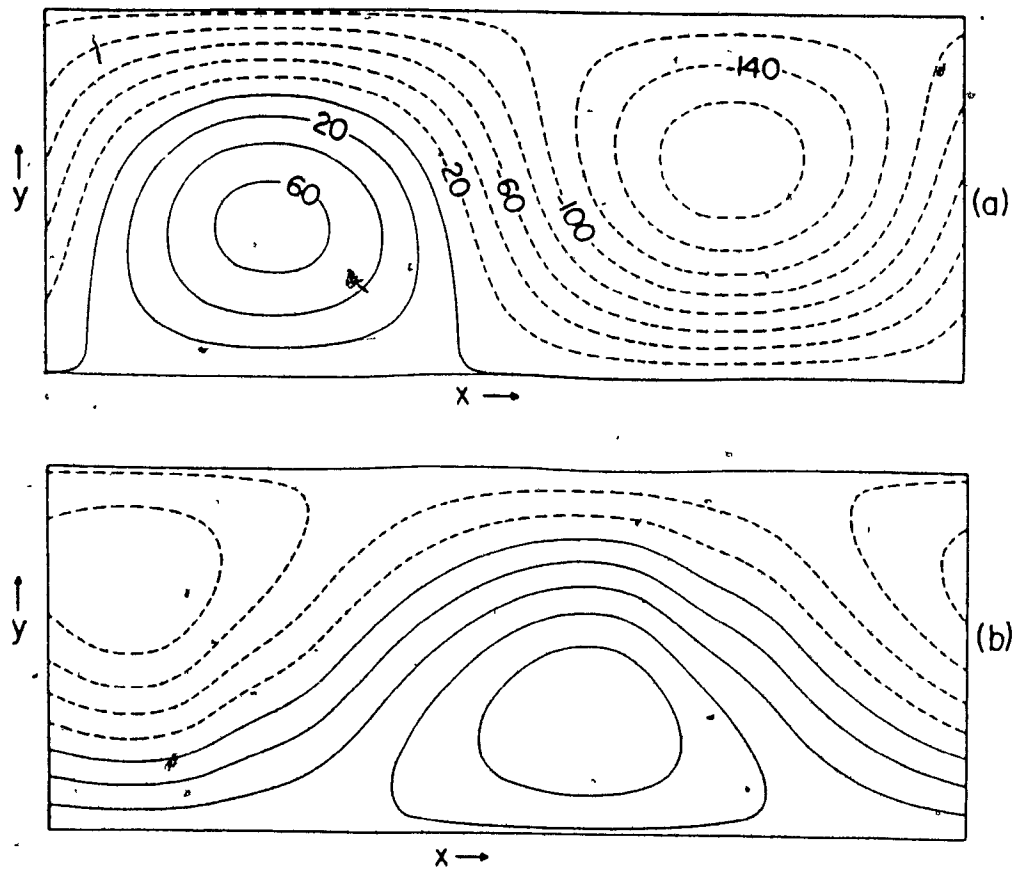


Figure 3 Unstable superresonant zonal-wavenumber-1 flow (region I).

- (a) Basic flow: $u_s = 25$ m/s, $2h_\alpha/H = 0.02$;
 (b) growing perturbation: $\omega = 0.02i$ day⁻¹.

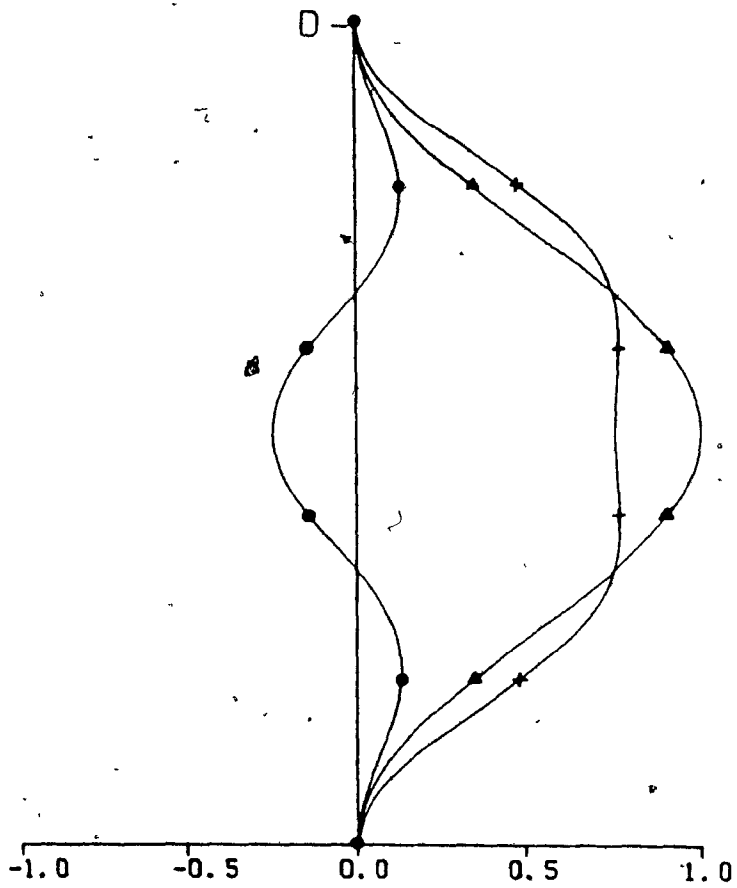


Figure 4. Reynolds stress (dot), form drag (triangle) and total zonal momentum tendency (plus) for the case of Figure 3.

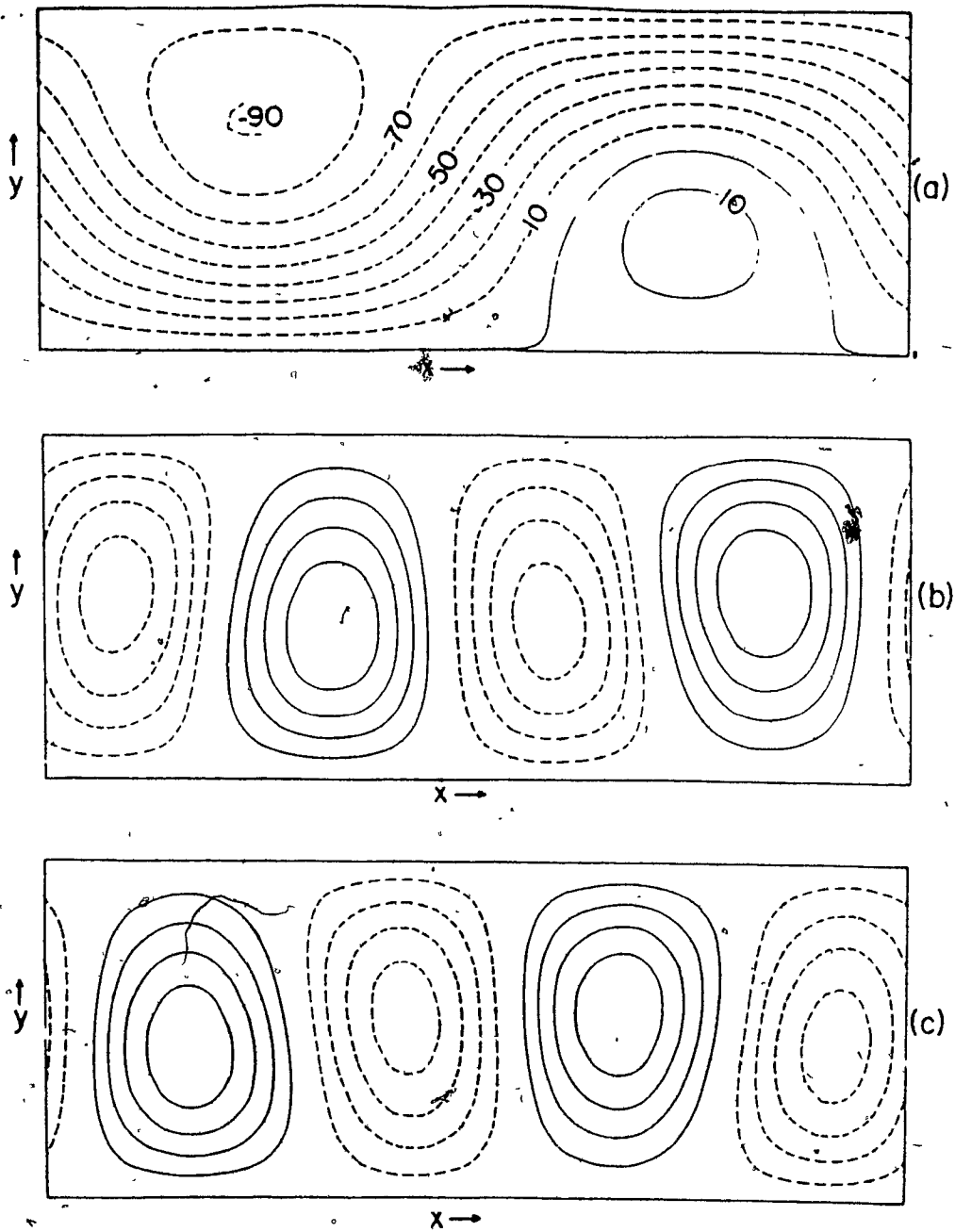


Figure 5 Unstable subresonant zonal-wavenumber-1 flow [region II(a)].

- (a) Basic flow: $u_s = 18 \text{ m/s}$, $2h_\alpha/H = 0.1$;
- (b) growing perturbation: $\omega = 0.11 \text{ day}^{-1}$;
- (c) damping perturbation: $\omega = -0.11 \text{ day}^{-1}$.

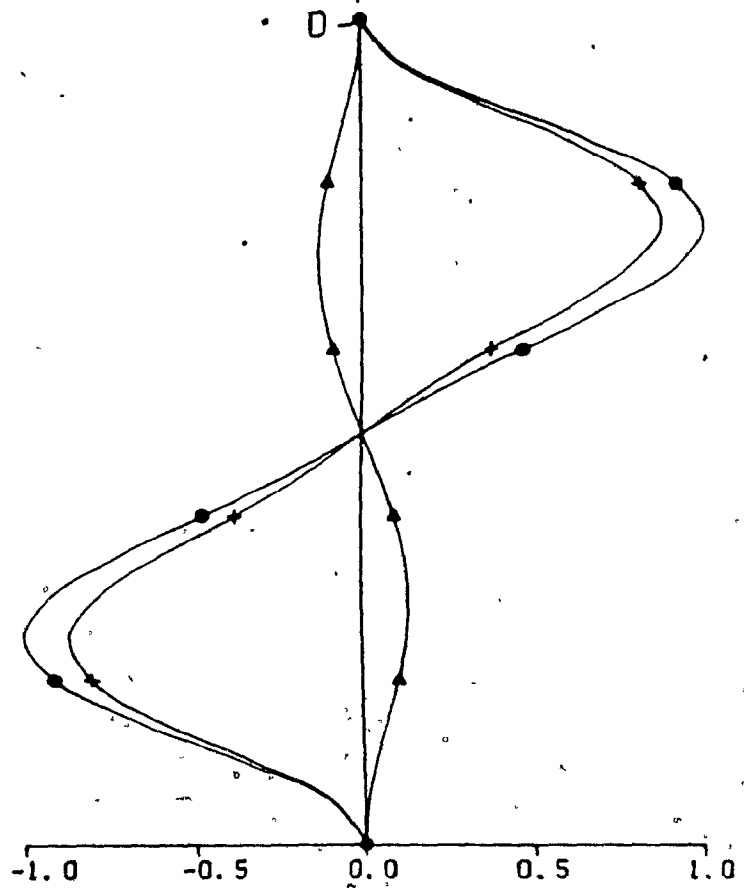


Figure 6 As in Figure 4 but for the case of Figure 5.

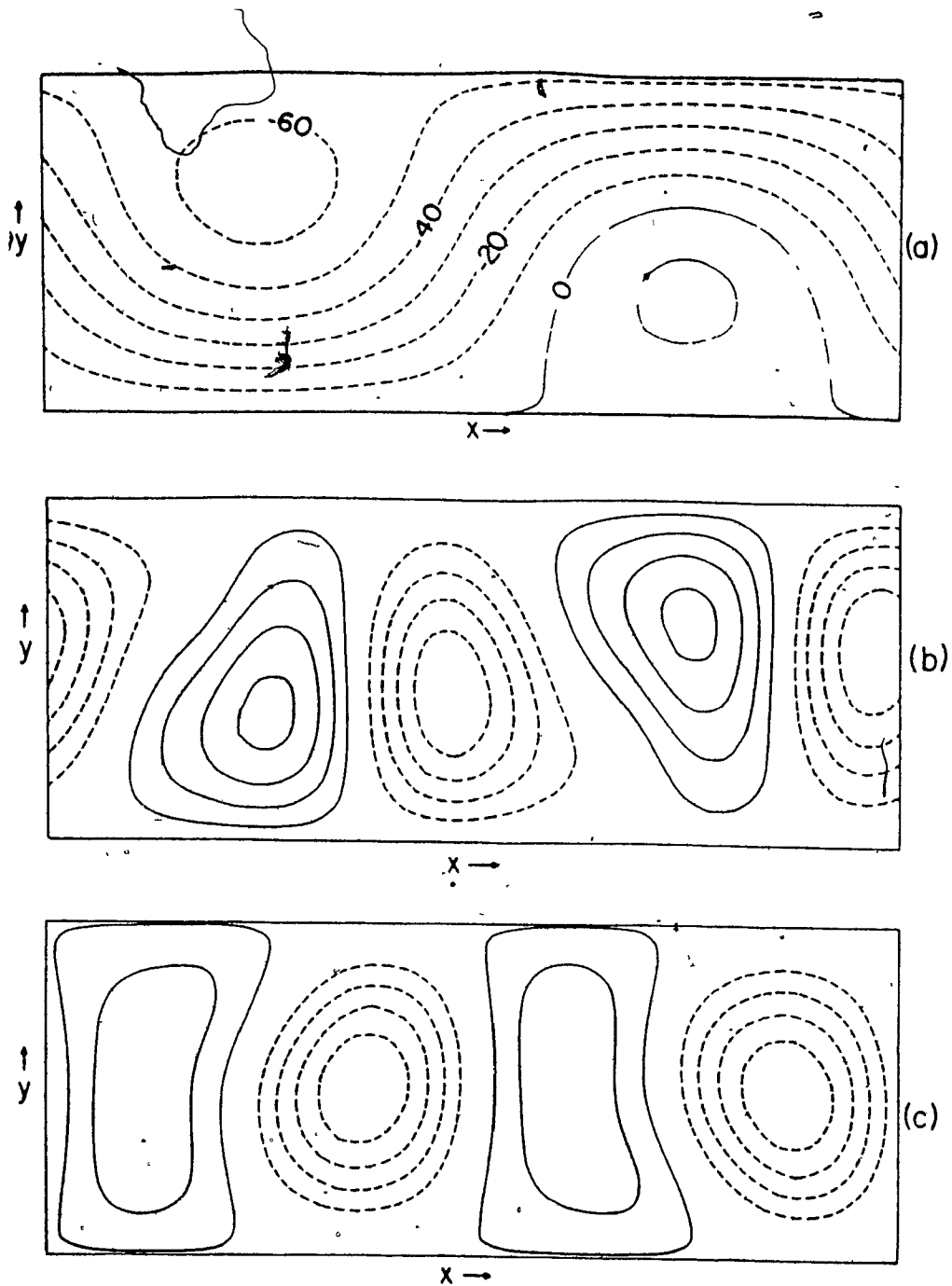


Figure 7 Unstable subresonant zonal-wavenumber-1 flow [region II(b)].

(a) Basic flow: $u_s = 12.5$ m/s, $2h_\alpha/H = 0.2$;

(b) growing perturbation at $t = 0$: $\omega = -0.18 + 0.09i$ day $^{-1}$;

(c) as in (b) but at $t = 9$ days.

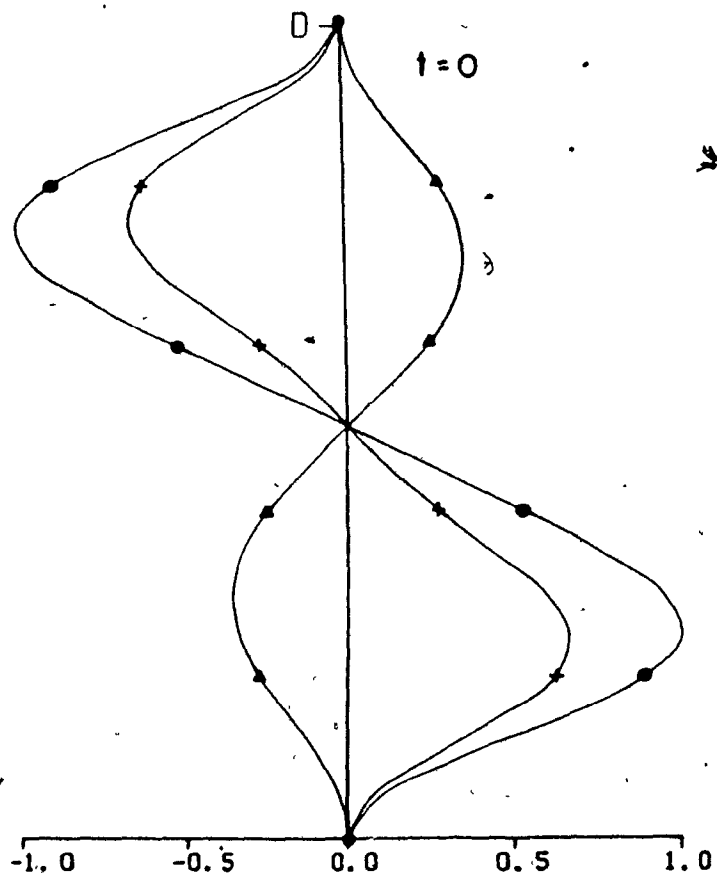


Figure 8 As in Figure 4 but for the case of Figure 7 ($t = 0$).

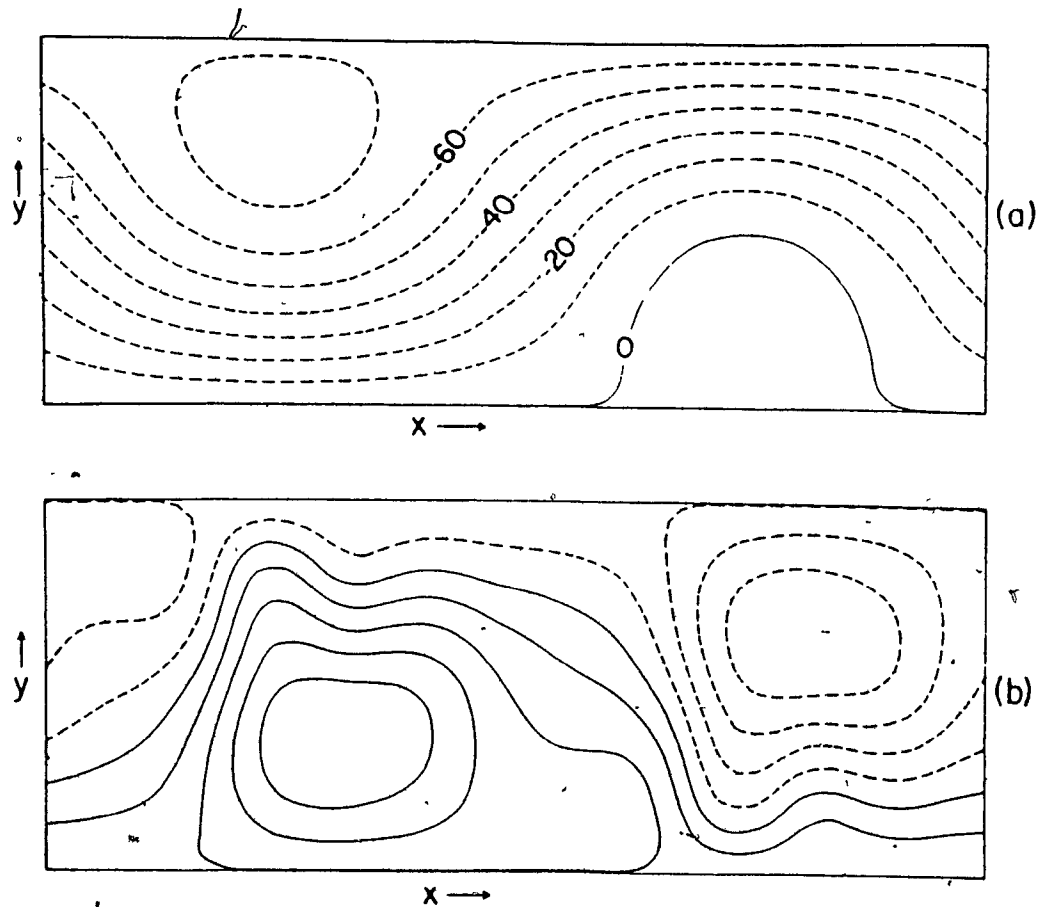


Figure 9 Subresonant zonal-wavenumber-1 topographic instability.

- (a) Basic flow: $u_s = 16.3$ m/s, $2h_a/H = 0.1$;
 (b) growing perturbation at $t = 7T/8 \approx 25.8$ days:
 $\omega = -0.21 + 0.009i$ day⁻¹.

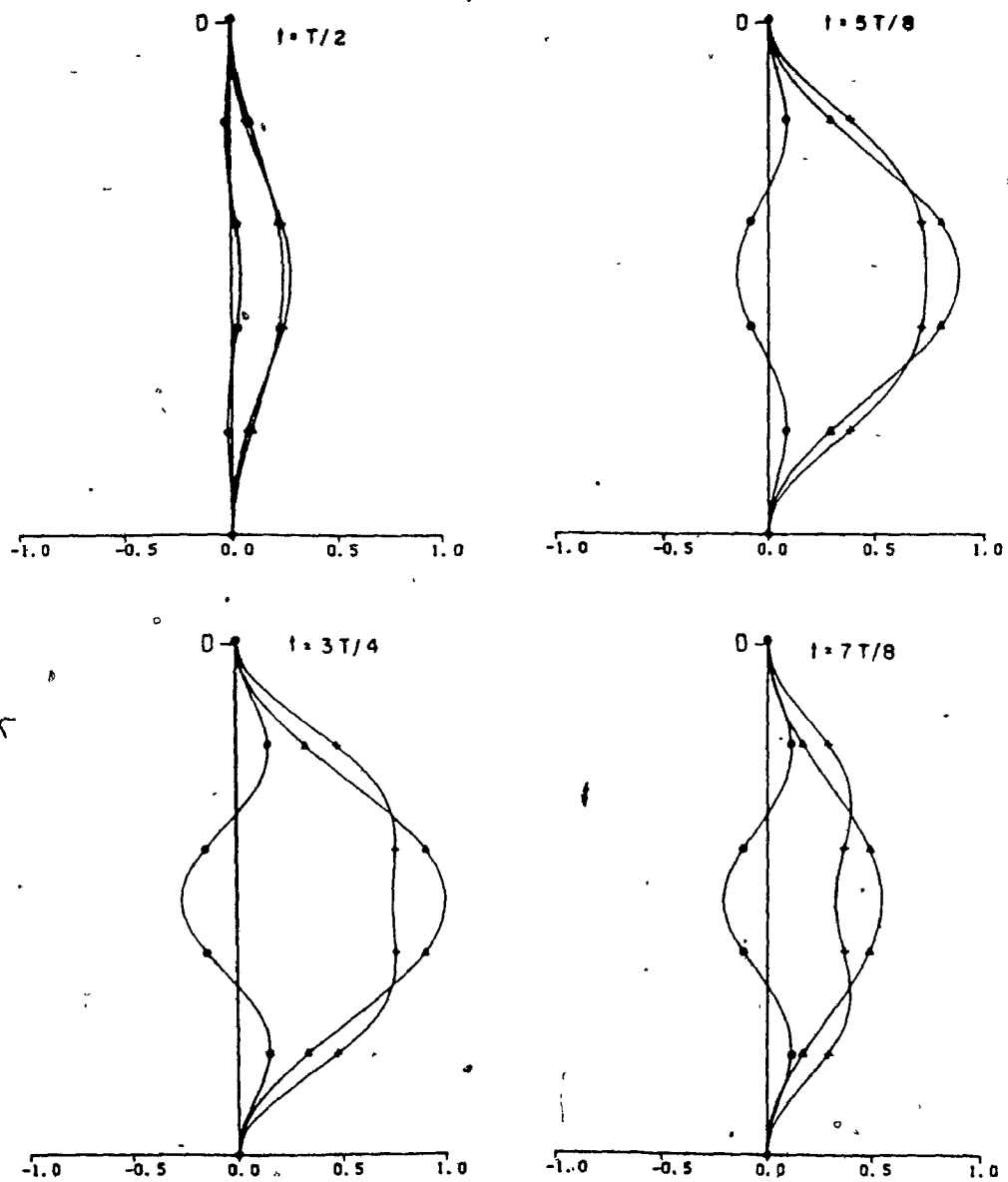


Figure 10 As in Figure 4 but for the case of Figure 9 at various times. The period T of the oscillation is 29.5 days.

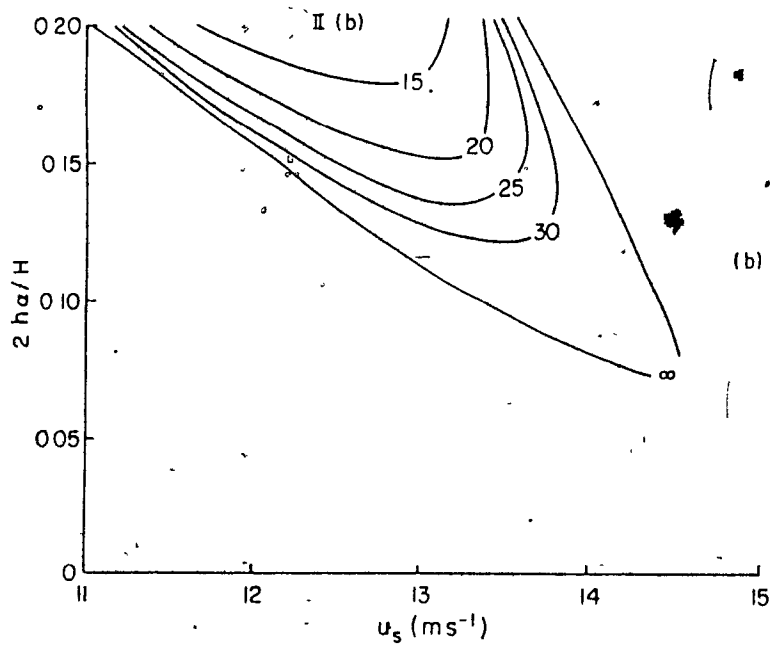
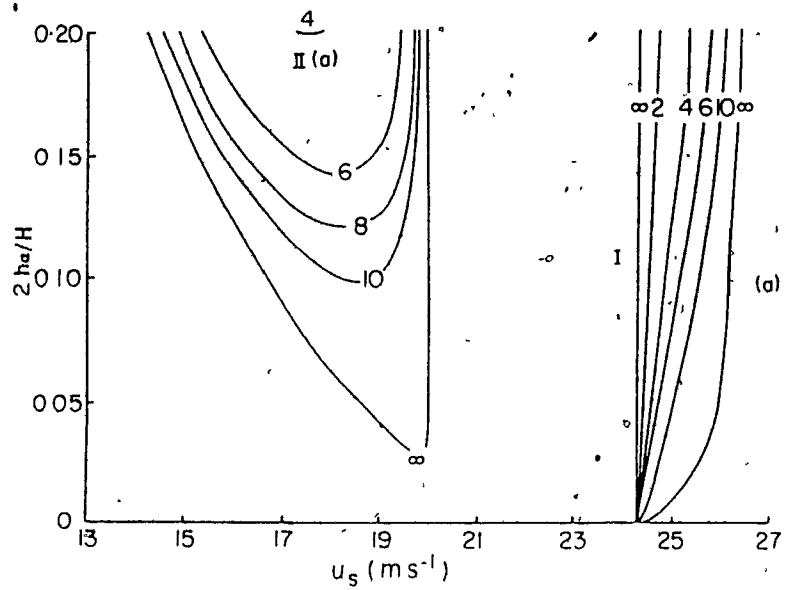


Figure 11 As in Figure 2 but for the severe truncation.

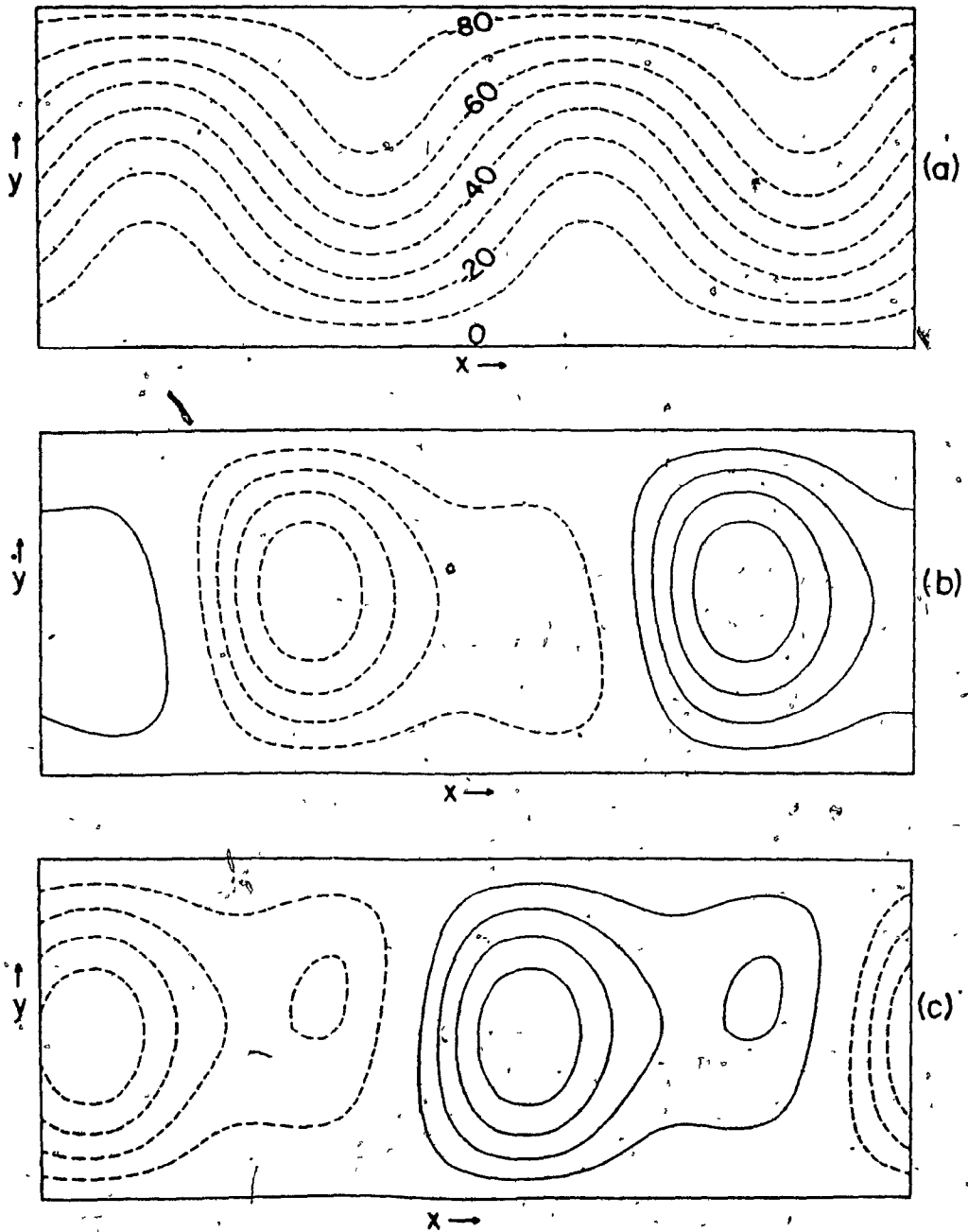


Figure 12 Unstable zonal-wavenumber-2 free Rossby wave flow.

- (a) Basic flow: $U = 20$ m/s;
- (b) growing perturbation at $t = 0$: $\omega = -0.10 + 0.06i$ day $^{-1}$;
- (c) as in (b) but at $t = 16$ days.

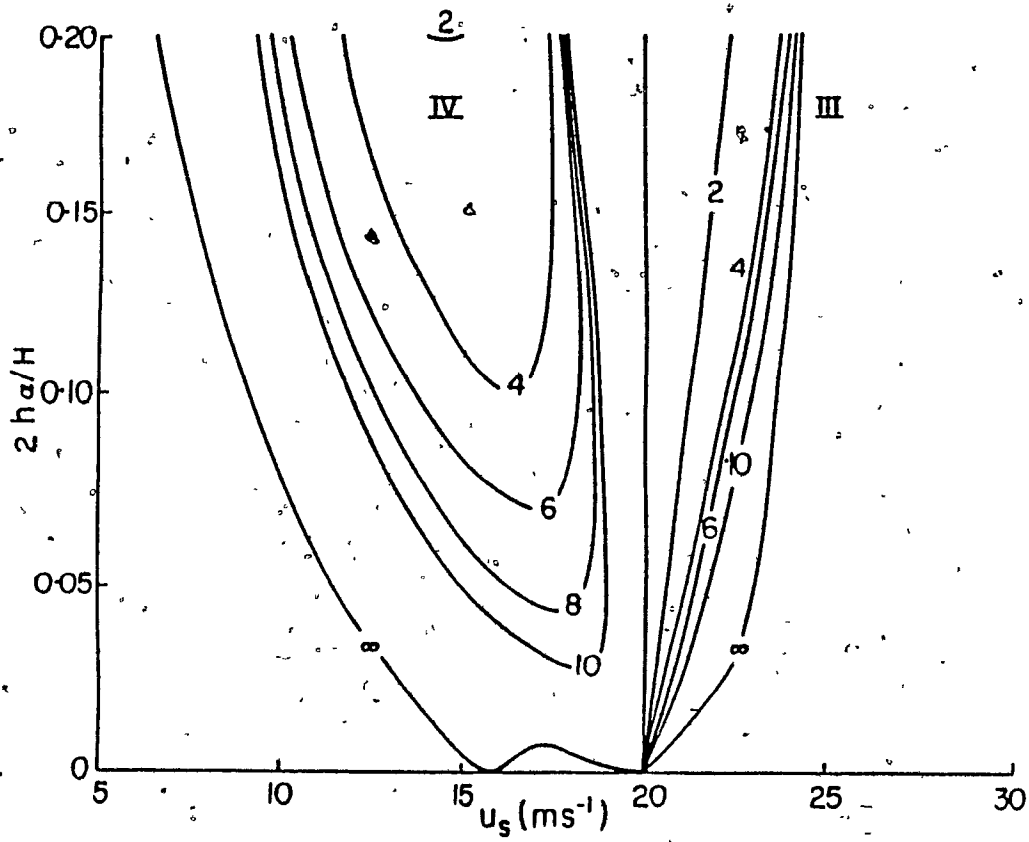


Figure 10 As in Figure 2 but for zonal-wavenumber-2 flows.

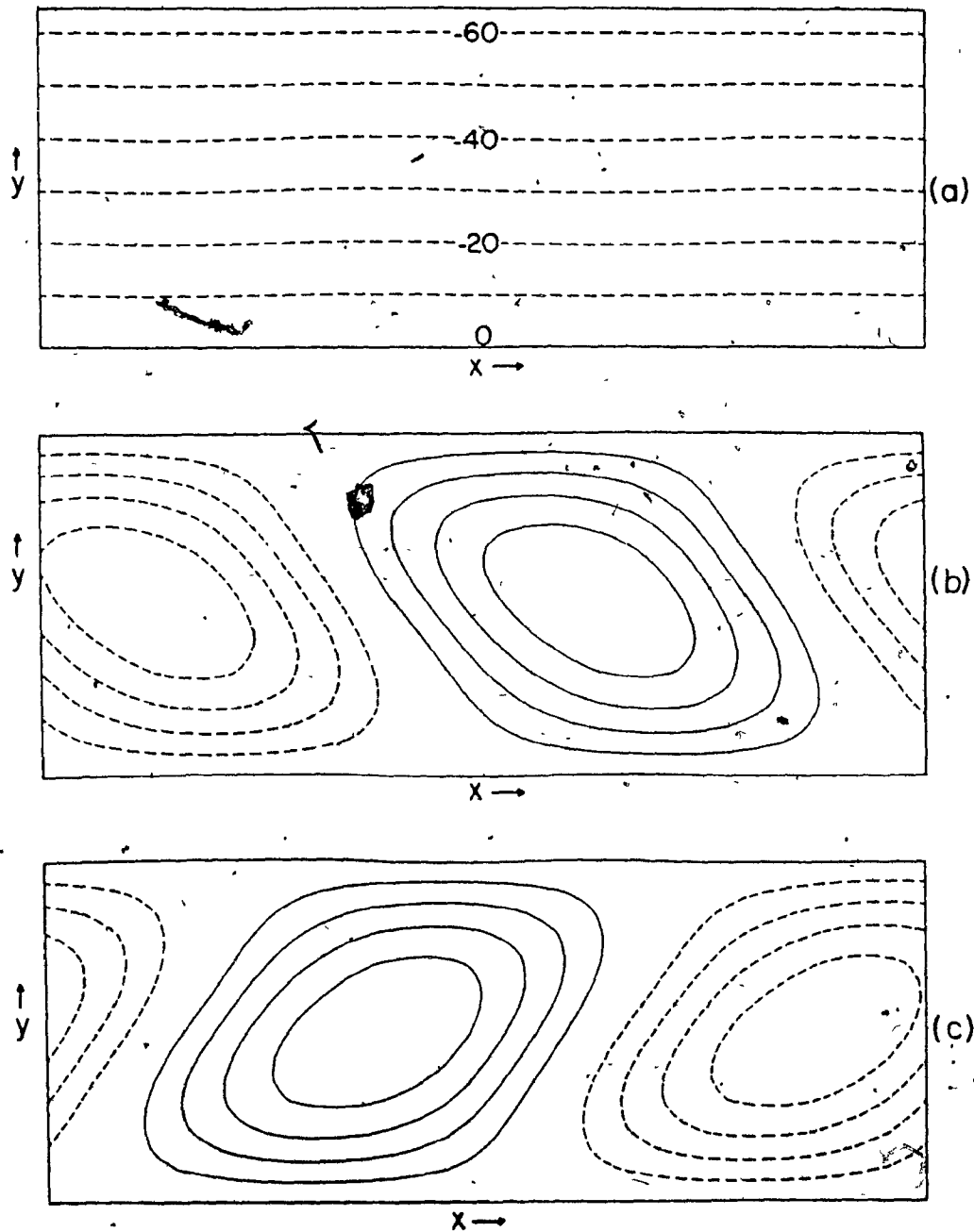


Figure 14 Unstable zonal-wavenumber-2 flow (resonant interaction).

- (a) Basic flow: $u_s = 15.4$ m/s, $2h_\alpha/H = 0.001$;
- (b) growing perturbation ($t = 0$): $\omega = -0.17 + 0.003i$ day $^{-1}$;
- (c) as in (b) but at $t = 9$ days.

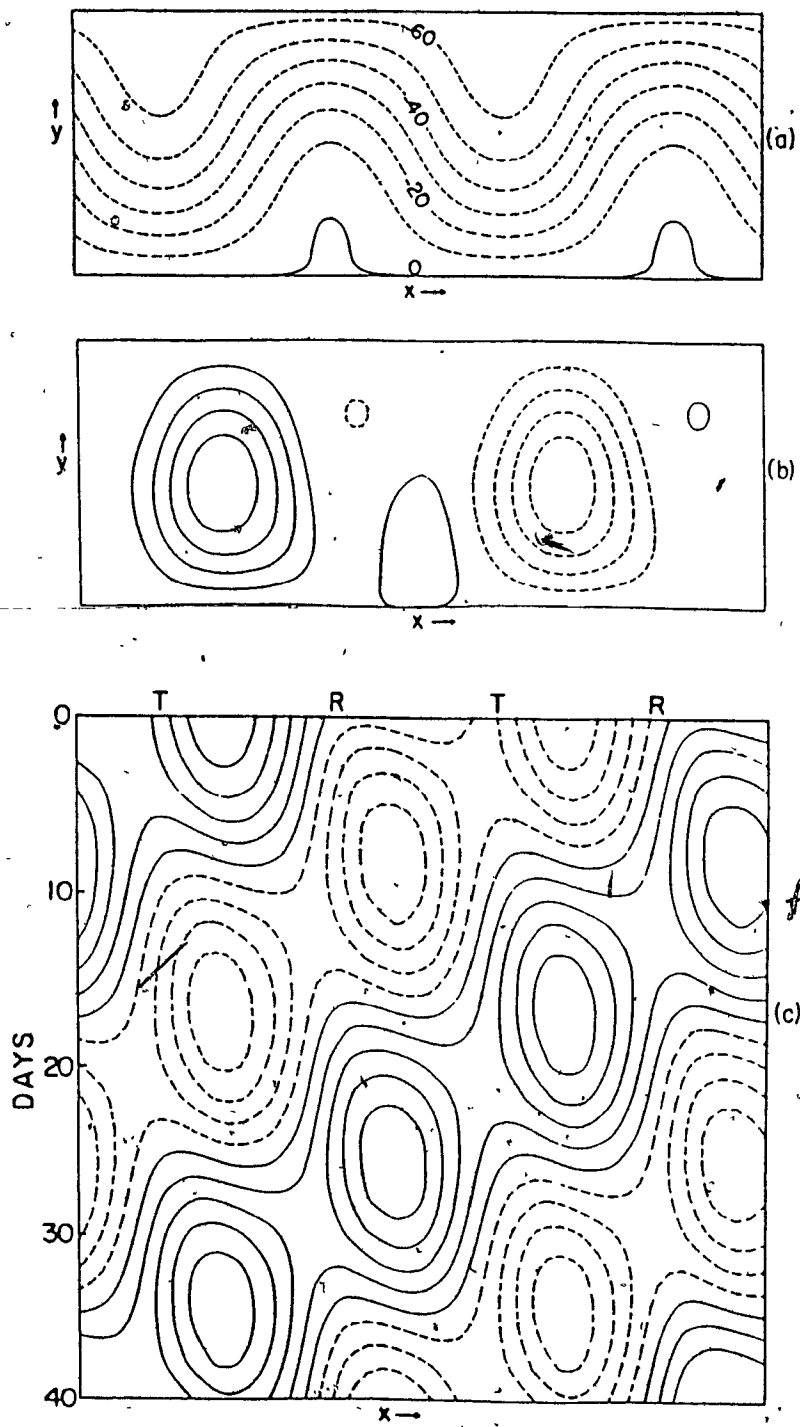


Figure 15 Unstable subresonant zonal-wavenumber-2 flow (shear instability).

- (a) Basic flow: $u_s = 15.4 \text{ m/s}$, $-2h_\alpha/H = 0.05$;
- (b) growing perturbation ($t = 0$): $\bar{\omega} = -0.18 + 0.11i \text{ day}^{-1}$;
- (c) 40-day Hovmöller diagram at $y = D/2$.

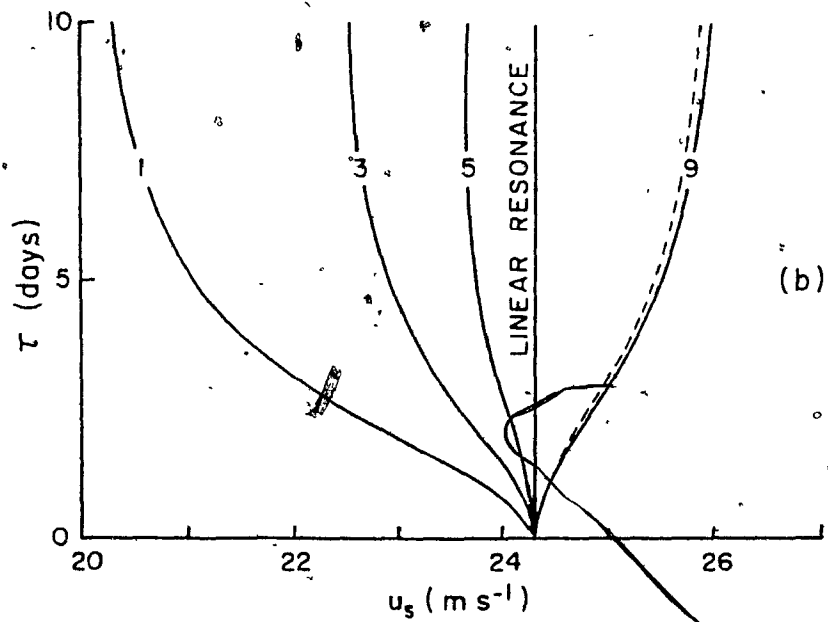
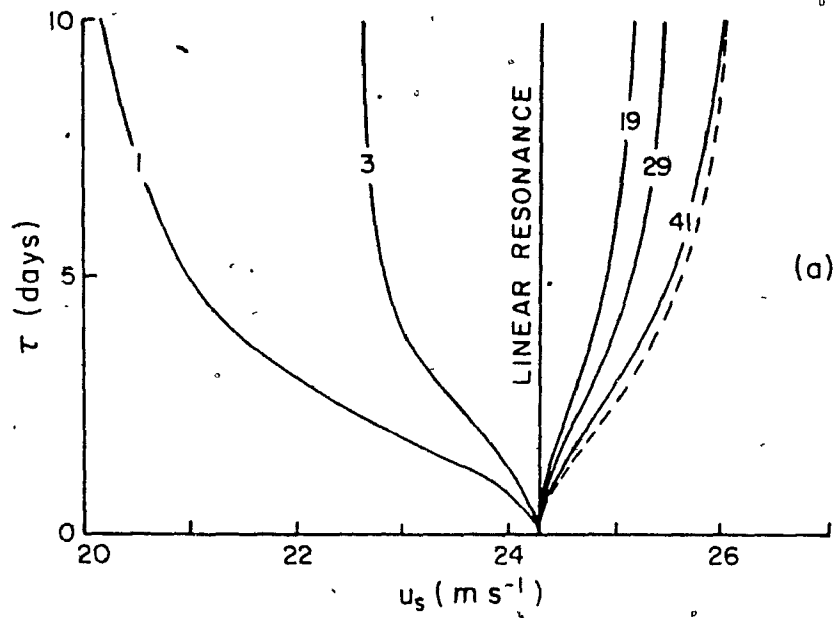


Figure 16 e-folding curves for various eddy truncations, NW .

- (a) $NZ = 41$ (dashed curve corresponds to $TR = [1,1]$);
- (b) $NZ = 9$ (dashed curve corresponds to $TR = [9,9]$ with 9 zonal wavenumbers). $2h_\alpha/H = 0.2$.

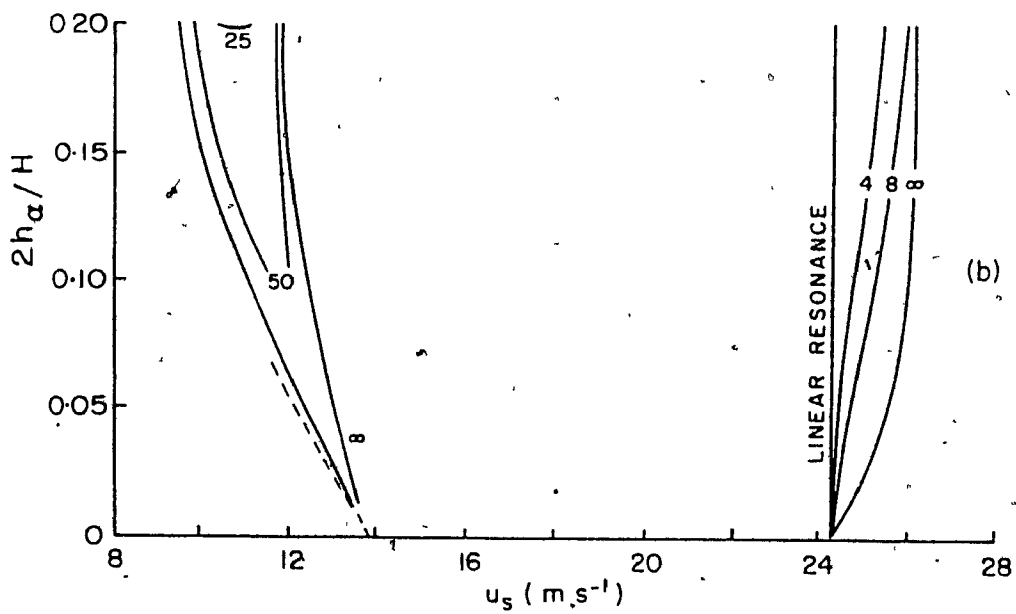
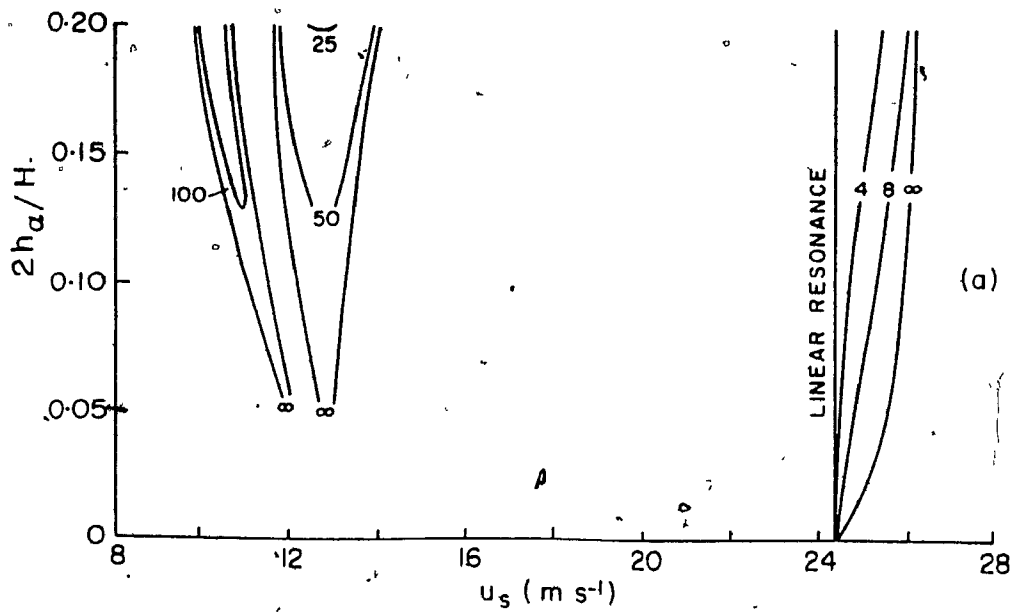


Figure 17 Contours of e-folding time in days.

(a) $TR = [41, 41]$;

(b) $TR = [3, 3]$ (dashed curve was obtained analytically).

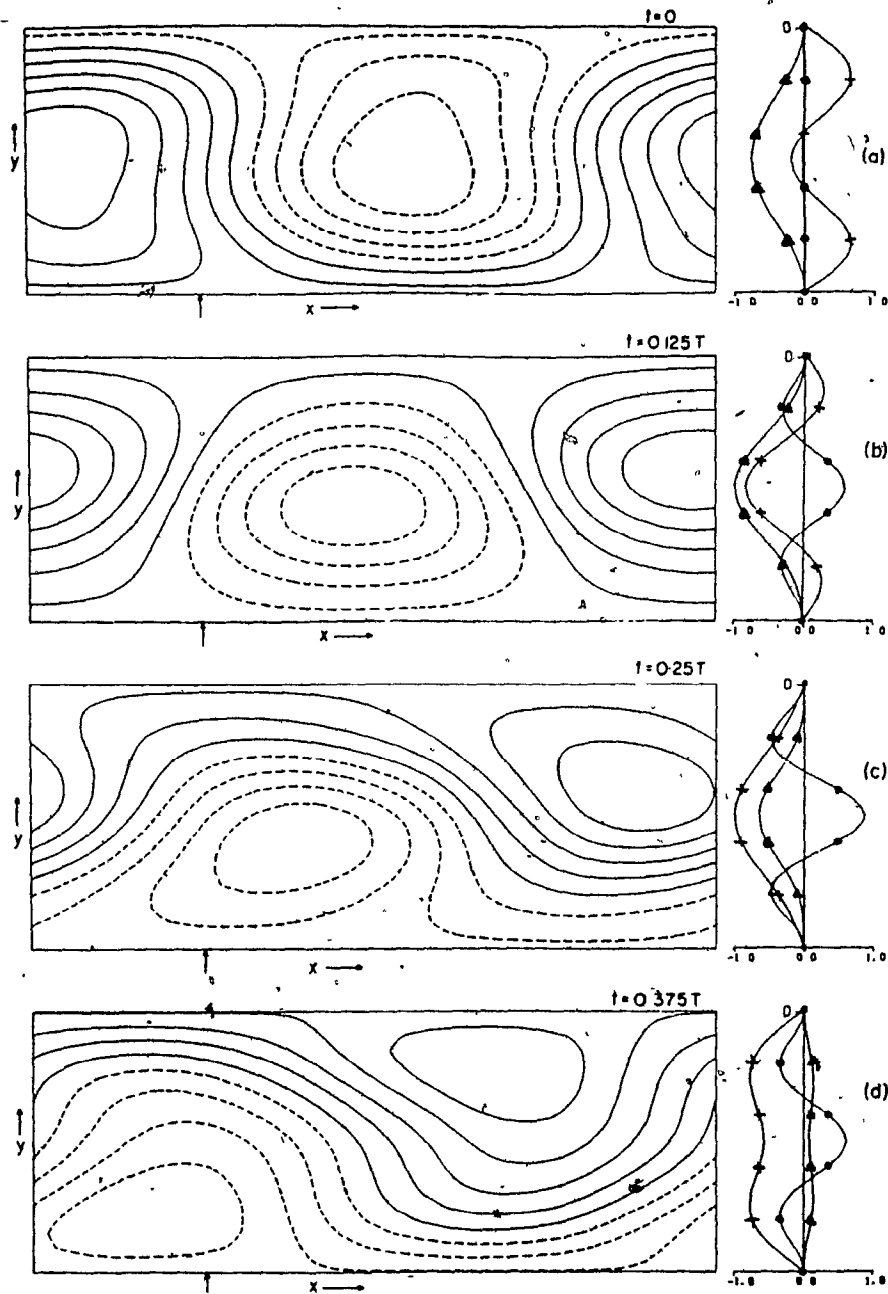


Figure 18 Subresonant travelling instability.

Basic flow: $u_s = 11.0$ m/s, $2h_\alpha/H = 0.2$;
 perturbation: $\omega \approx -0.4 + 0.04i$ day $^{-1}$. Reynolds stress
 (dot), form drag (triangle), and \bar{u}' (plus). $T \approx 16$ days.

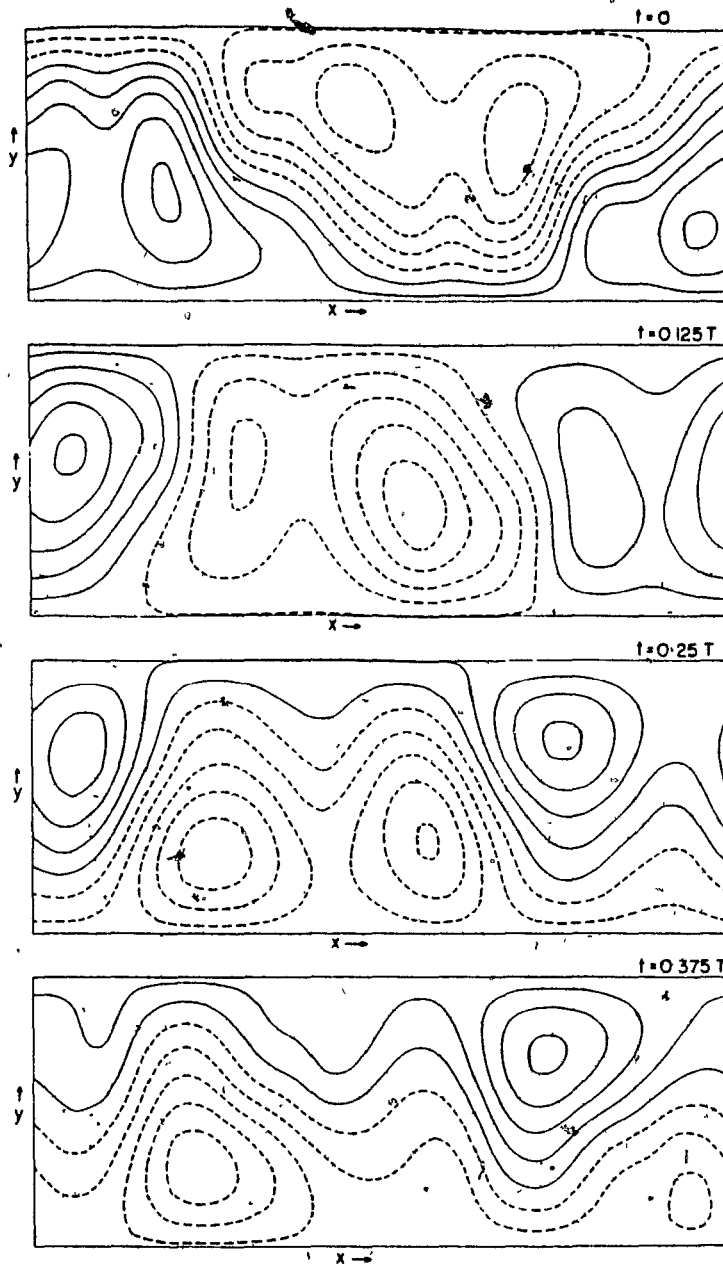


Figure 19 Subresonant travelling instability: high resolution.

Basic flow: $u_s = 13.0$ m/s, $2h_\alpha/H = 0.2$;
 perturbation: $\omega \approx -0.3 + 0.02i$ day $^{-1}$. $T \approx 20$ days.

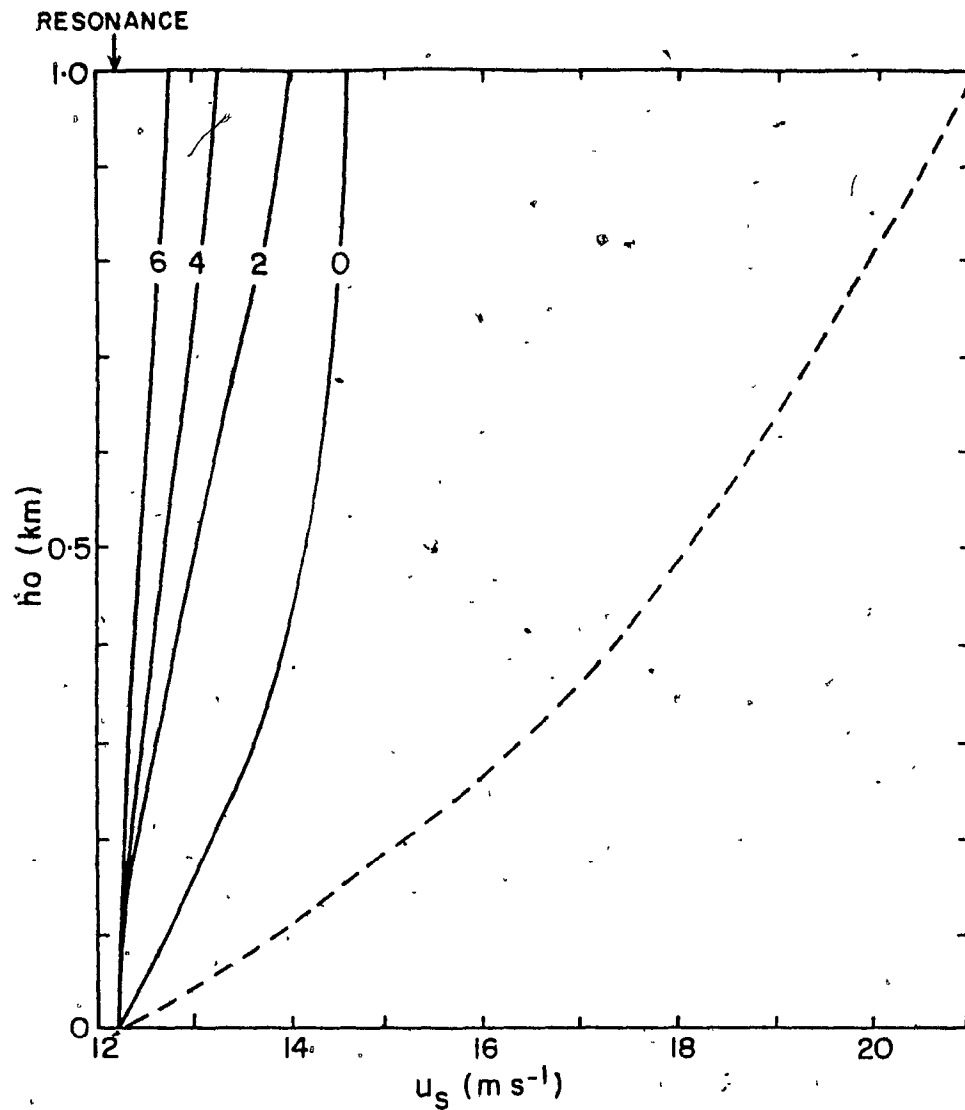


Figure 20 Contours of nondimensional growth rate for the topographic mode. Dashed line is the severe truncation neutral curve.

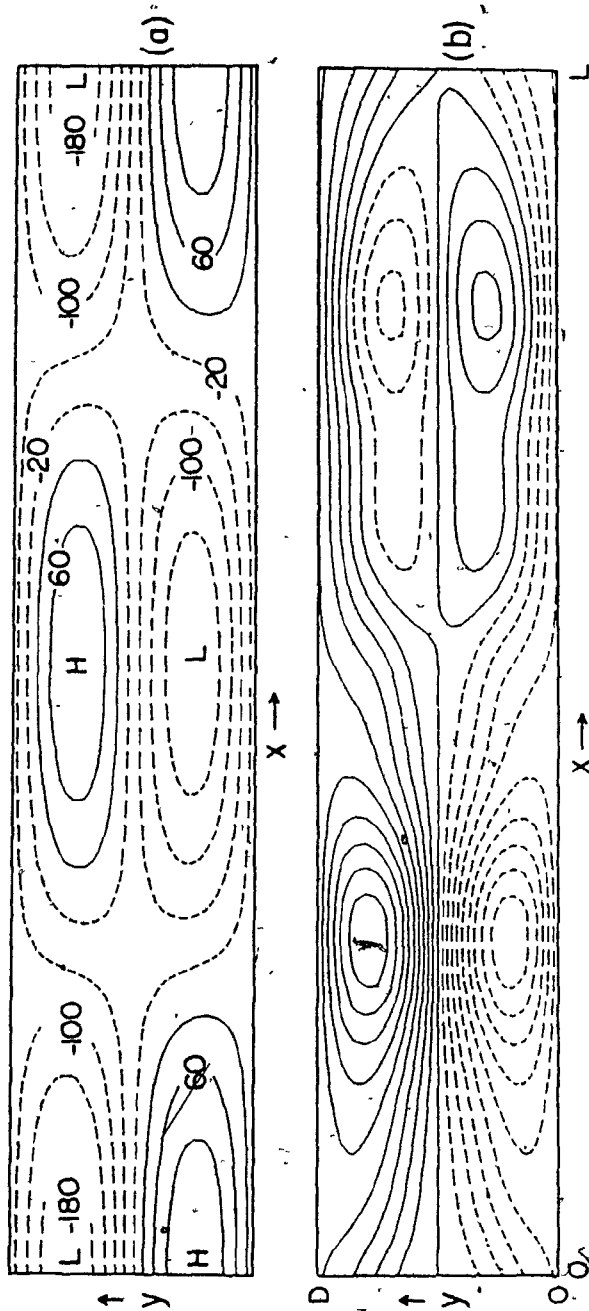


Figure 21 Topographic instability ($TR = [10, 10]$).

(a) Basic flow: $u_s = 13$ m/s, $h_0 = 1$ km;
 (b) slowest-growing perturbation: $\hat{\omega}_i \approx 2.33$, $\hat{\omega}_r = 0$.

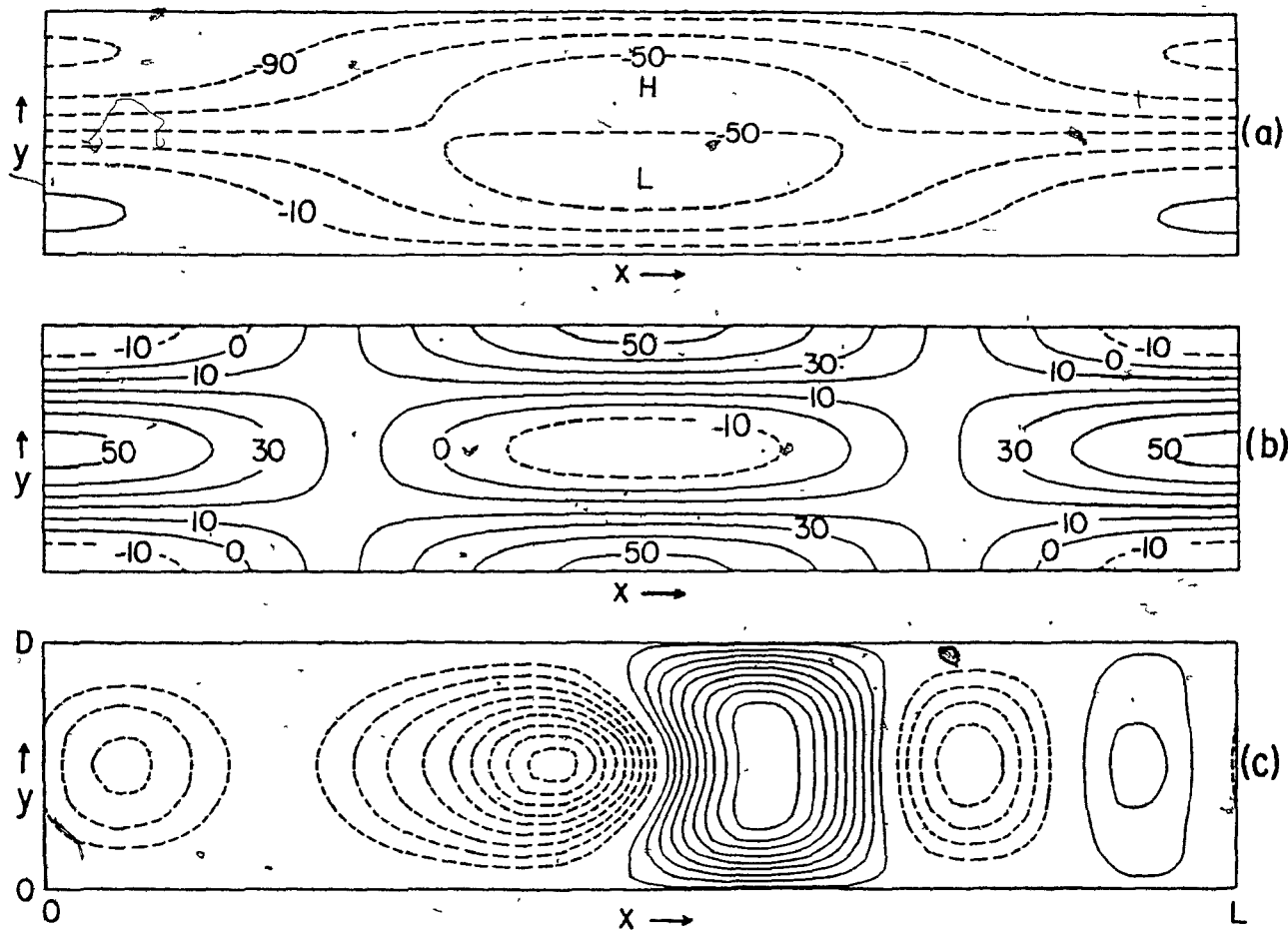


Figure 22 Non-topographic instability ($TR = [10, 10]$).

- (a) Basic flow: $U_0 = 17$ m/s, $h_0 = 1$ km;
- (b) basic flow zonal component, \bar{u} (in units of m s^{-1});
- (c) fastest-growing perturbation: $\hat{\omega}_i \approx 3.61$, $\hat{\omega}_r = 0$.

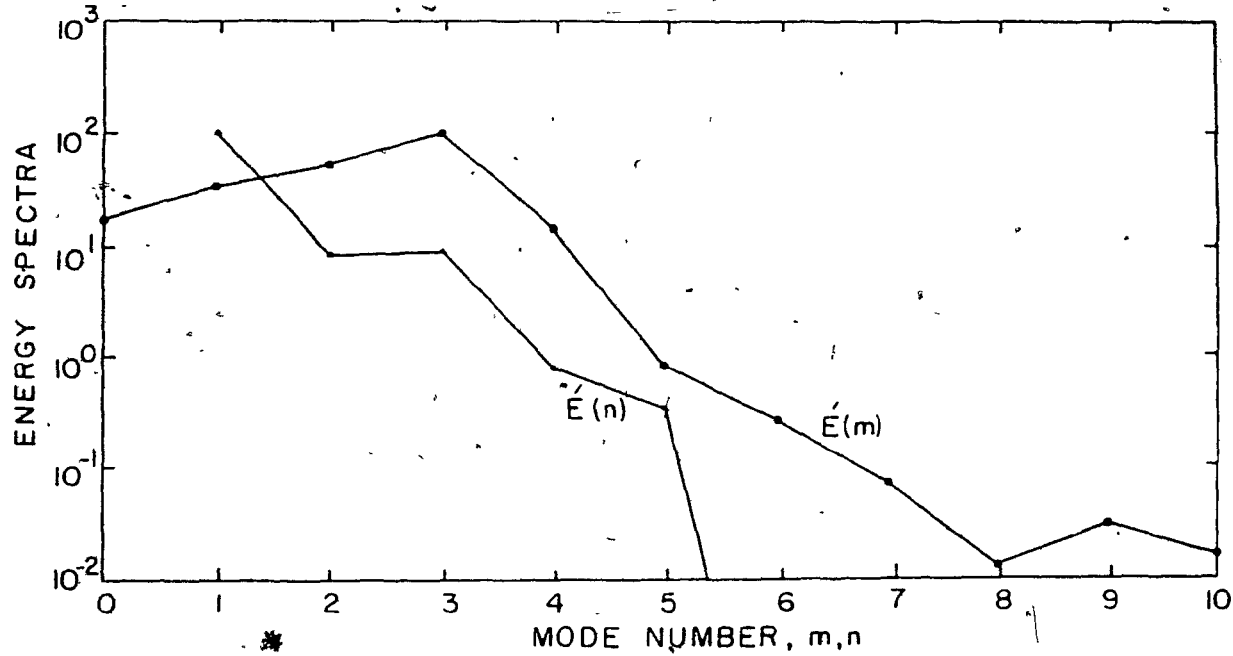


Figure 23 Zonal and meridional energy spectra, $E'(m)$ and $E'(n)$, respectively, corresponding to the mode in Figure 22c.

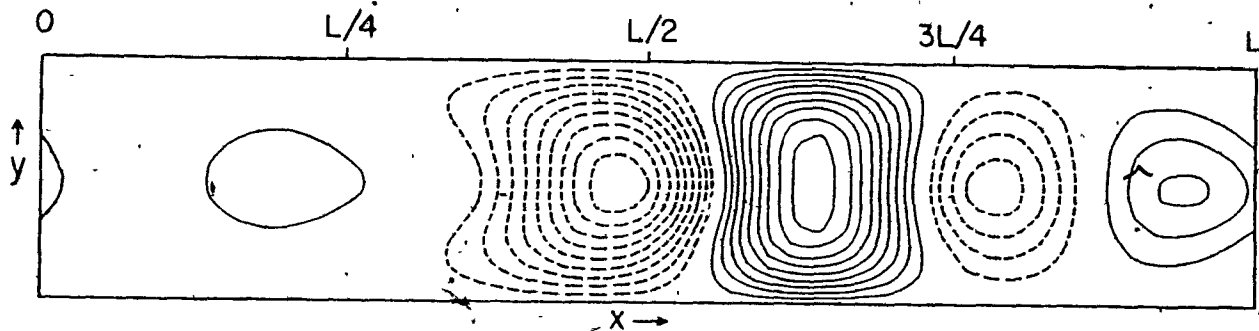


Figure 24 Fastest-growing mode to basic flow of Figure 22a when
 $TR = [5, 3]$. Structure at $t = 0$: $\hat{\omega}_i \approx 2.78$, $\hat{\omega}_r \approx 0.82$.

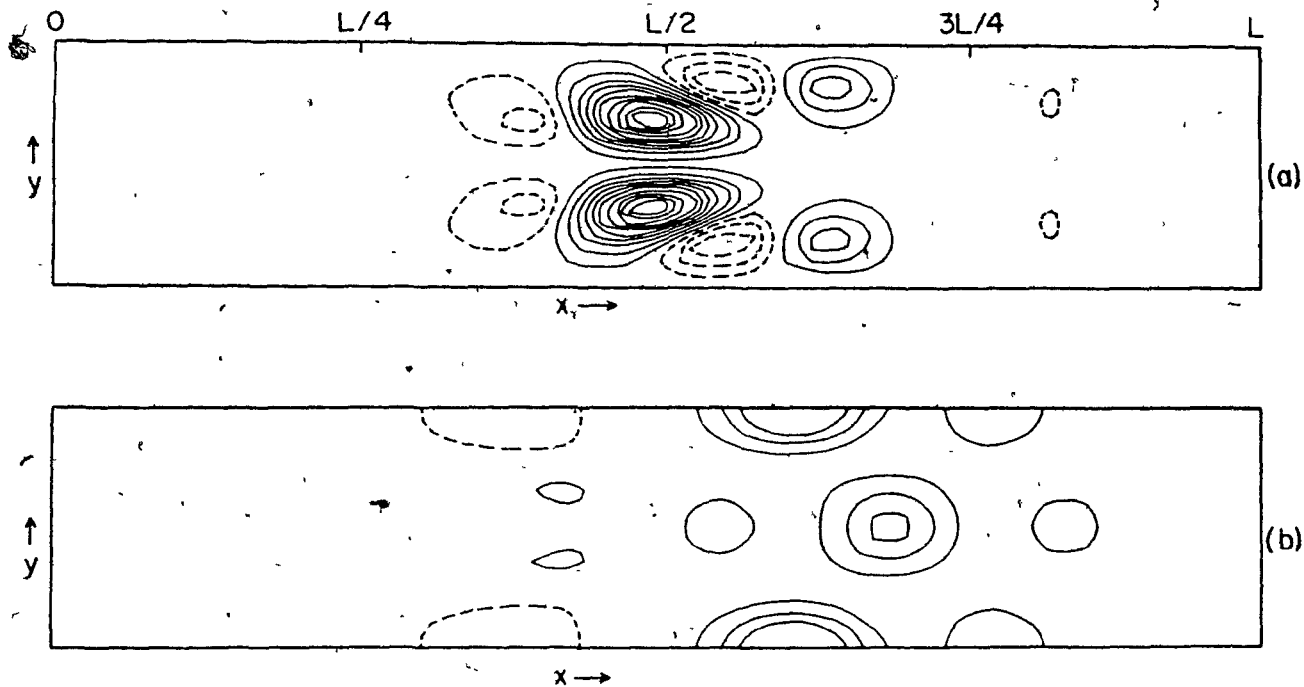


Figure 25 Local energy contributions from the fastest-growing mode.

- (a) Local contribution to $C_x + C_y$ energy conversion.
- (b) Local contribution to C_{xy} energy conversion.

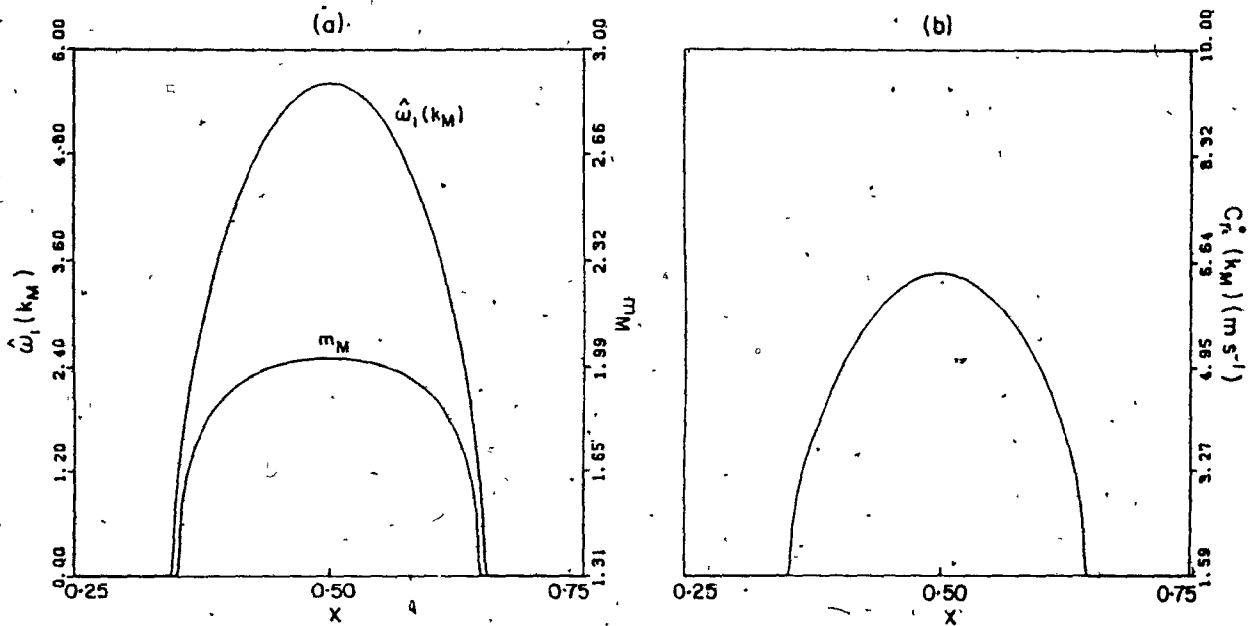


Figure 26 Stability curves obtained using the two-term system.

- (a) Most-unstable zonal wavenumber, $m_M = (2\pi\delta)^{-1} \cdot k_M$,
and growth rate, $\hat{\omega}_i$;
(b) phase speeds evaluated at m_M .

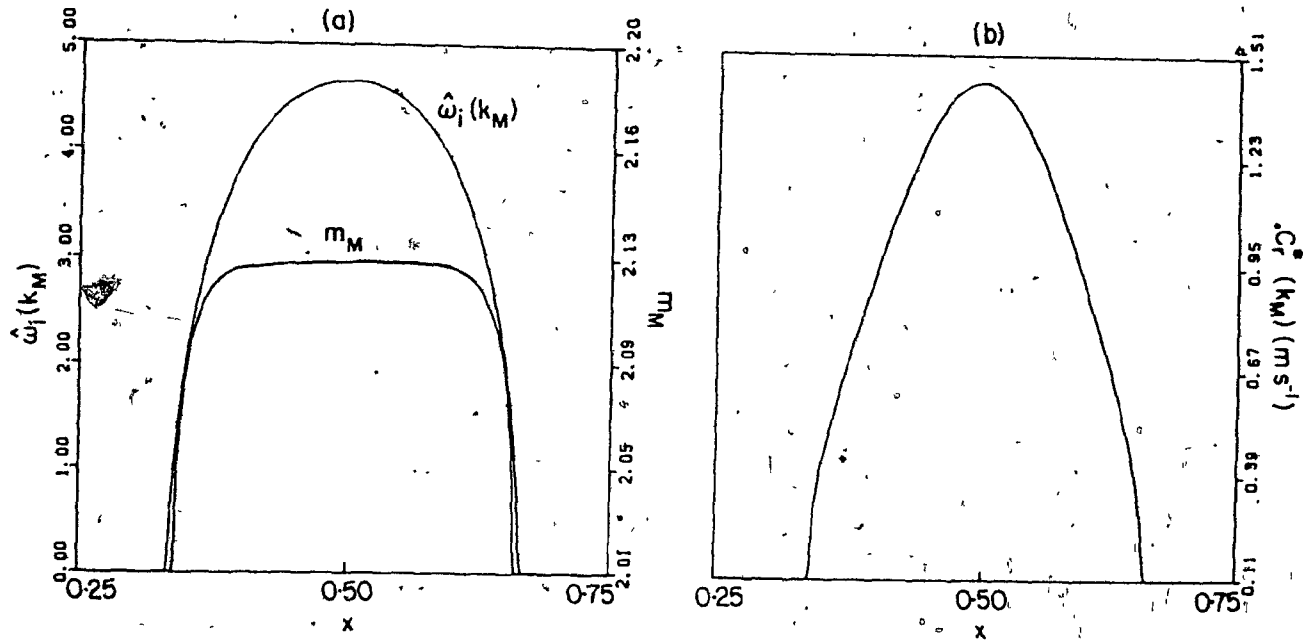


Figure 27. As in Figure 26 but for the three-term system.

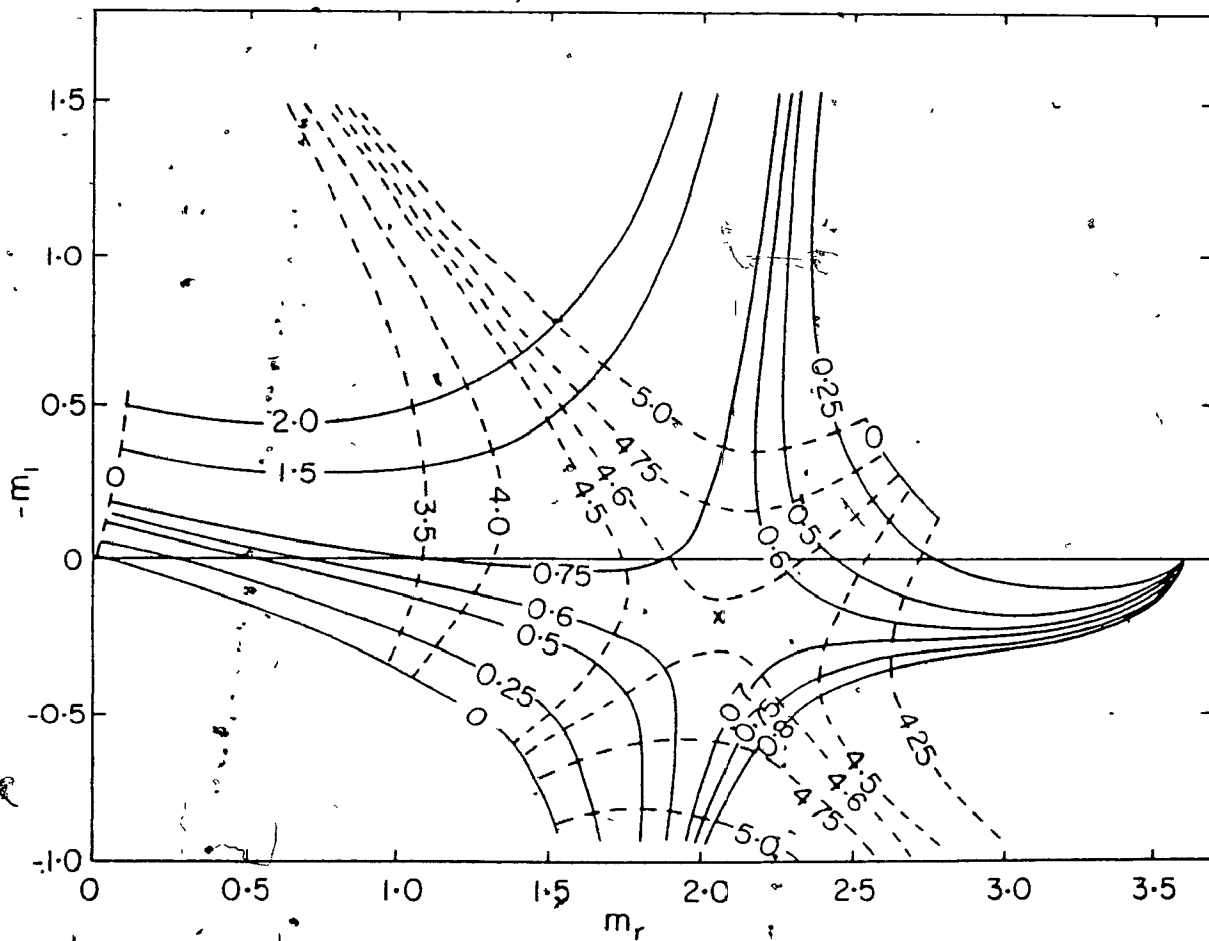


Figure 28 Mapping of $\omega(k)$ in the complex $m = (2\pi\delta)^{-1} k$ plane. Full lines correspond to constant $\hat{\omega}_r$ lines. Dashed lines correspond to constant $\hat{\omega}_i$ lines.

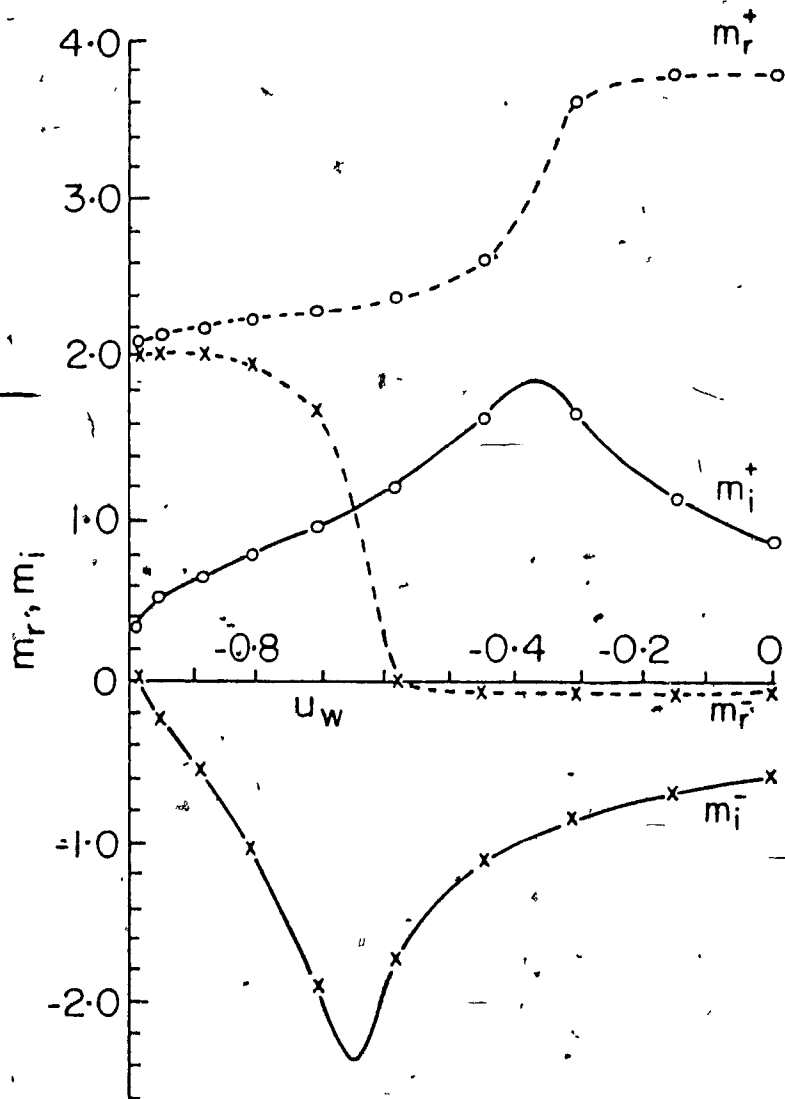


Figure 29 Complex wavenumber, m , versus zonal flow, $u_w(X)$, for two branches of the dispersion relationship. The two branches are denoted m^+ and m^- . Dashed line with circles, m_r^+ ; solid line with circles, m_i^+ ; dashed line with crosses, m_r^- ; solid line with crosses, m_i^- .

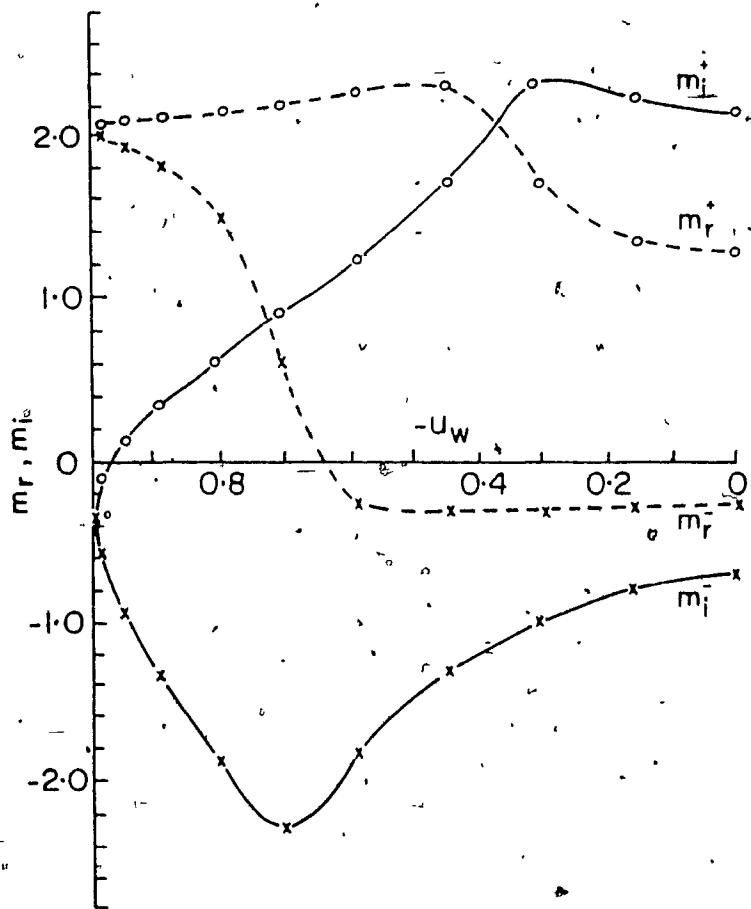


Figure 30 As in Figure 29 but for the two-term system.

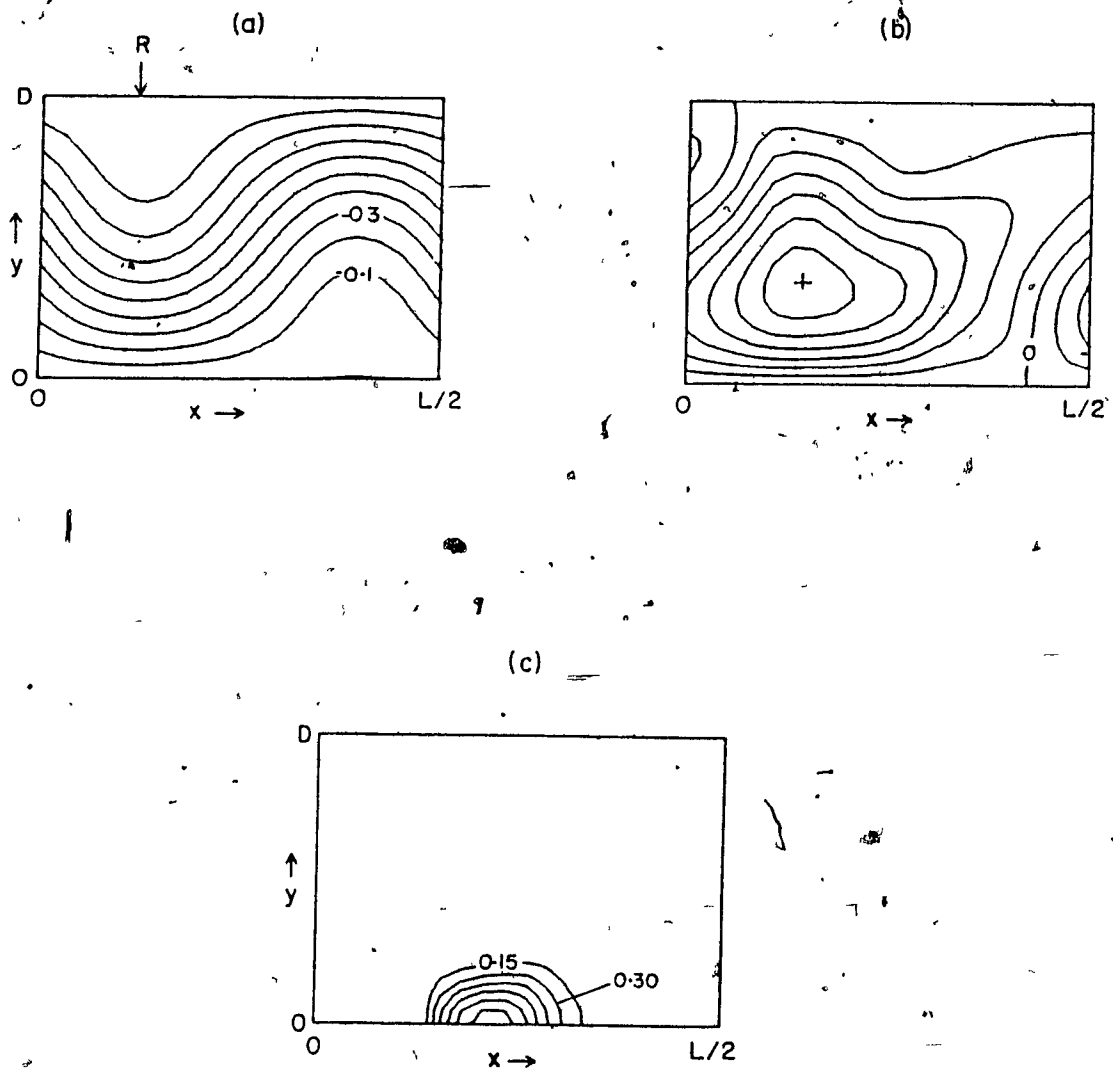


Figure 31 Experiment 1: Steady flow and disturbance.
(CINT = contour interval)

- (a) Steady flow streamfunction (CINT = 0.1);
- (b) FGLD structure at $t = 0$;
- (c) positive contours of $-(u'^2 - v'^2)\partial_x \bar{u}$. (CINT = 0.15).

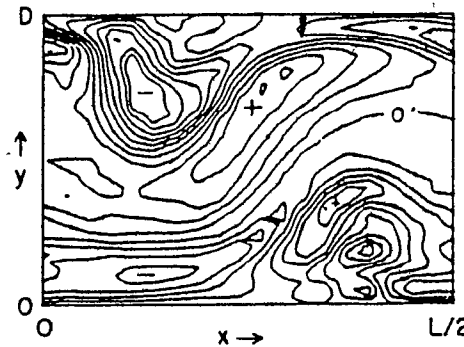
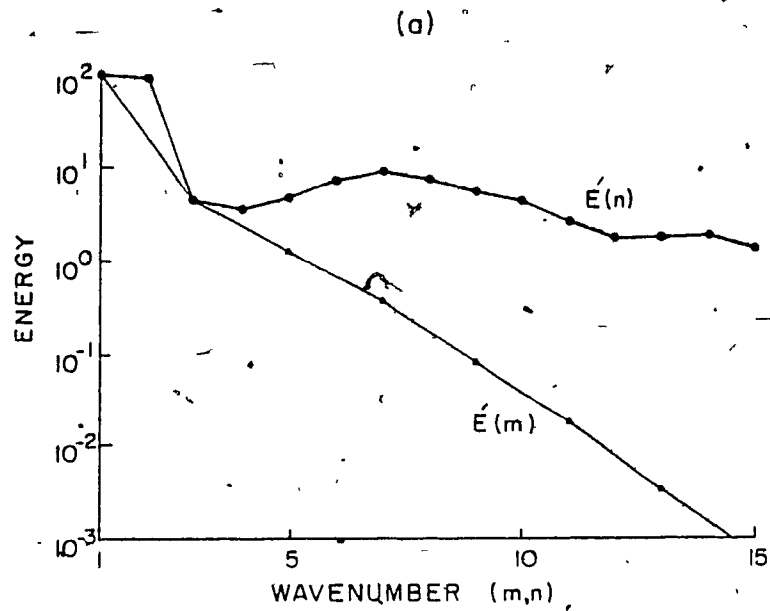


Figure 32 Experiment 1: Small scale structure in the FGLD.

- (a) Zonal and meridional energy spectra, $E'(m)$ and $E'(n)$, respectively;
- (b) disturbance vorticity, $\Delta\Psi_r$ (β and ϵ waves excluded).

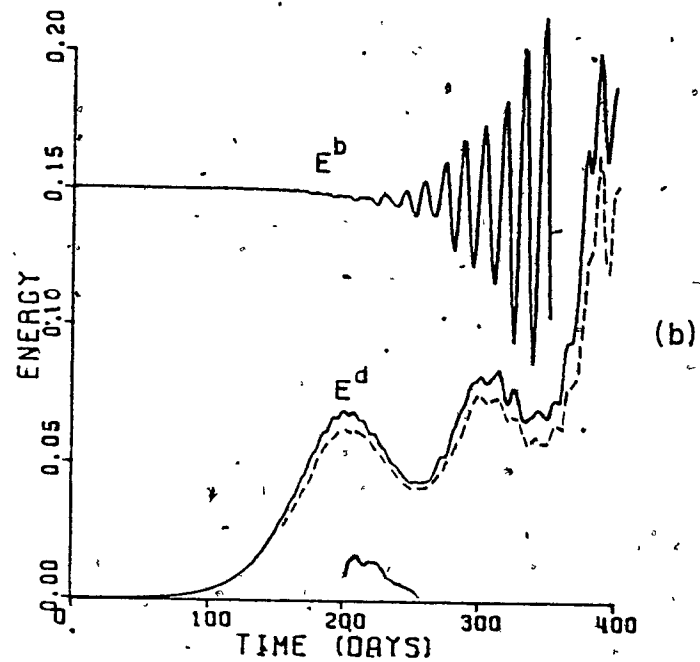
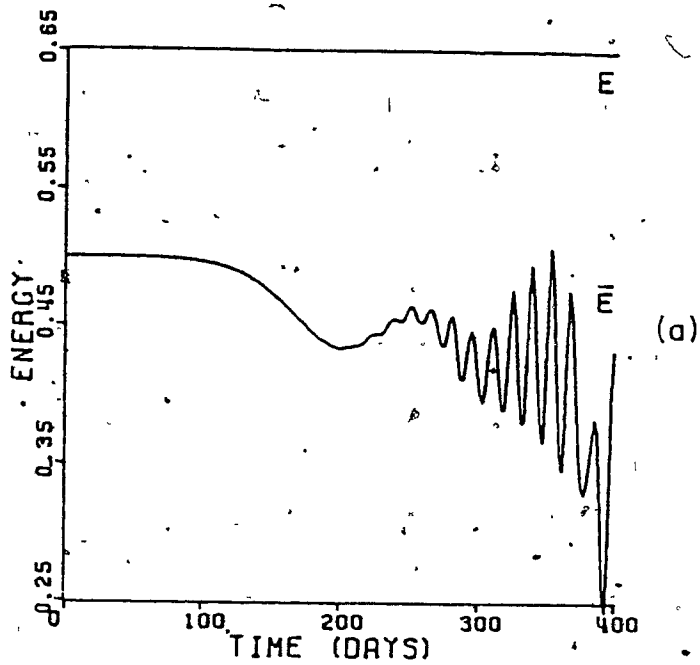


Figure 33. Experiment 1: Energy terms.

- (a) Total and mean zonal energy, E and \bar{E} , respectively;
 (b) basic wave and disturbance energy, E^b and E^d , respectively. (Note that the plot of E^b has been terminated early so that it would not obscure E^d). The dashed curve is the contribution to E^d from the β and ξ waves alone.

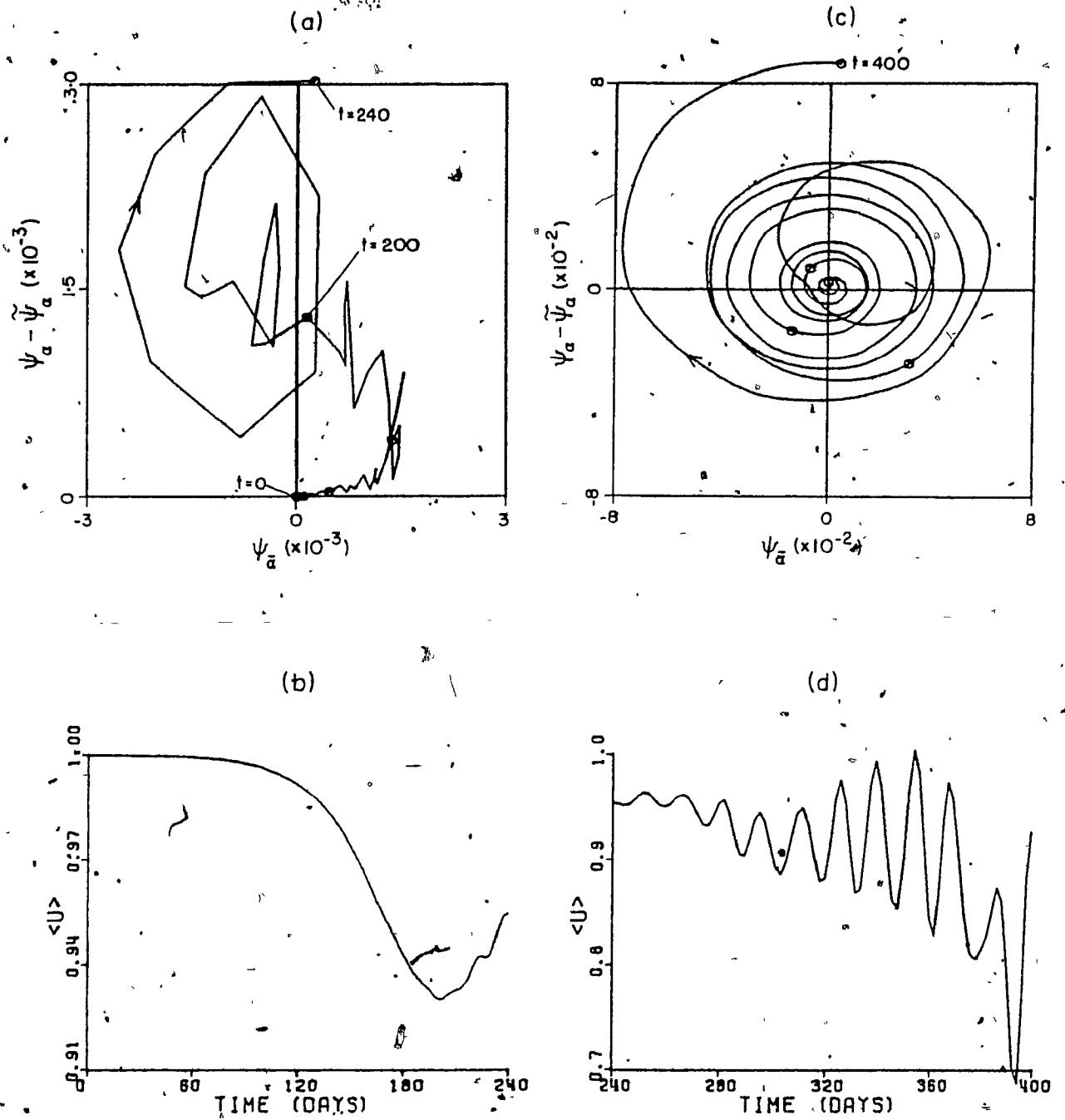


Figure 34. Experiment 1: Basic wave trajectory and the channel averaged flow.

- (a) ψ^b for $0 \leq t \leq 240$ days (dots at every 40 days);
- (b) $\langle u \rangle$ for $0 \leq t \leq 240$ days;
- (c) ψ^b for $240 \leq t \leq 400$ days;
- (d) $\langle u \rangle$ for $240 \leq t \leq 400$ days;

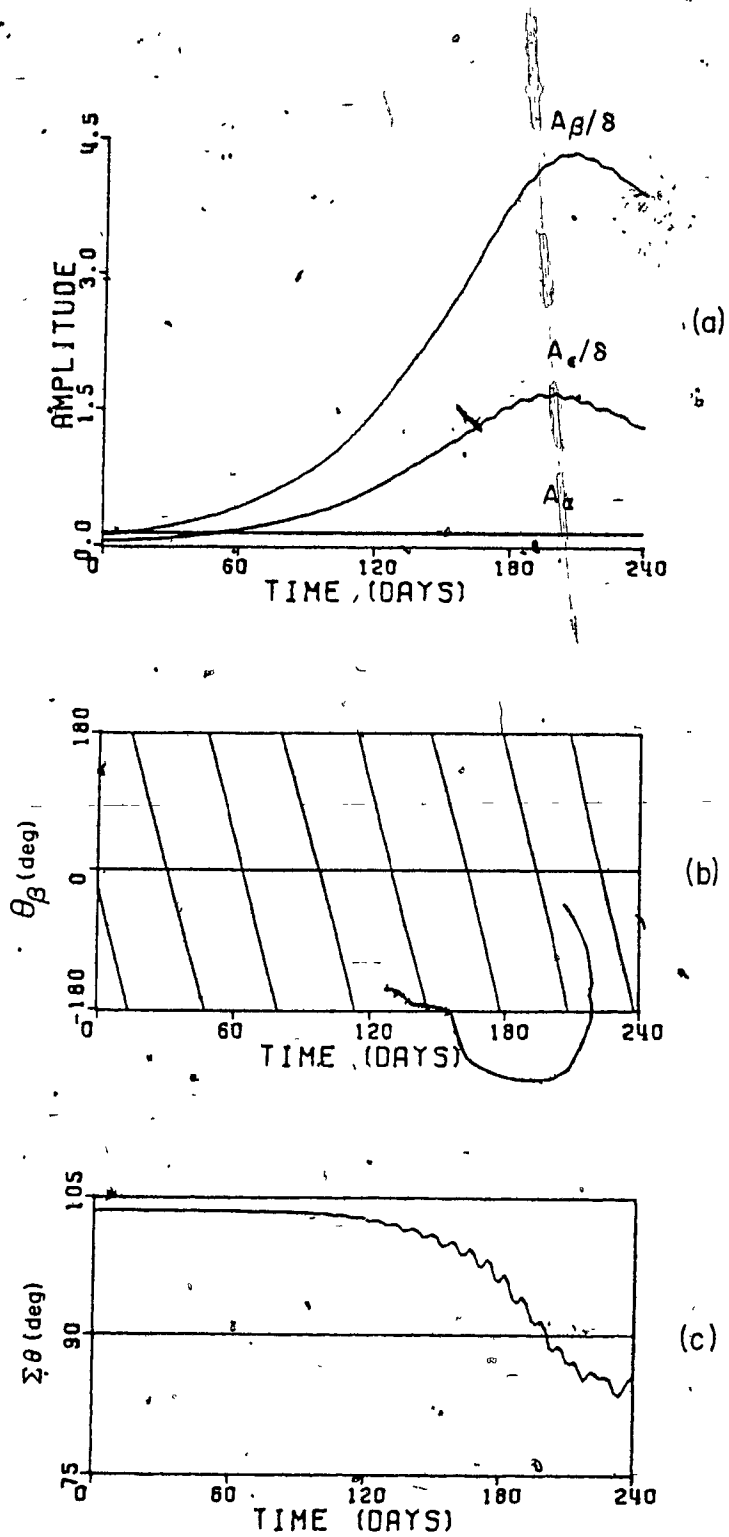


Figure 35 Experiment 1: Behaviour of the primary disturbance waves.

- (a) Amplitude of the primary waves and the basic wave: A_{β} , A_{ϵ} and A_{α} , respectively. ($\delta = 0.02$);
- (b) phase of the β -wave: $\theta_{\beta} = \tan^{-1}(\psi_{\beta}/\psi_{\beta})$;
- (c) phase sum: $\Sigma\theta = \theta_{\beta} + \theta_{\epsilon} + \theta_{\alpha}$.

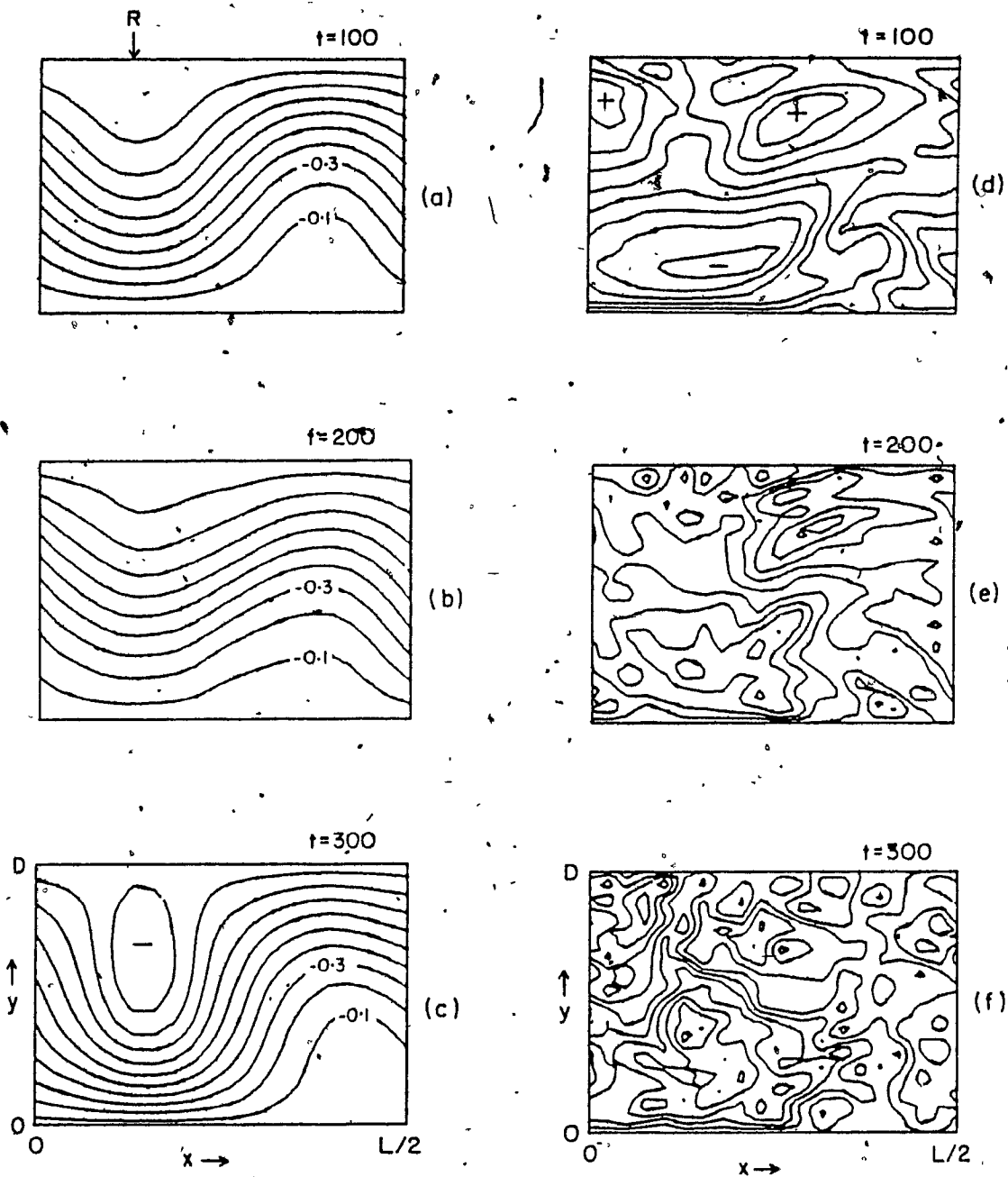


Figure 36 Experiment 1: Streamfunction of the total flow, ψ , and the disturbance vorticity, ζ^d , at specified times.

- (a) ψ ($t = 100$); (b) ψ ($t = 200$); (c) ψ ($t = 300$ days);
 (d) ζ^d ($t = 100$); (e) ζ^d ($t = 200$); (f) ζ^d ($t = 300$ days).
 [In (a), (b) and (c) CINT = 0.1; in (d) CINT = 0.2;
 in (e) and (f) CINT = 1.]

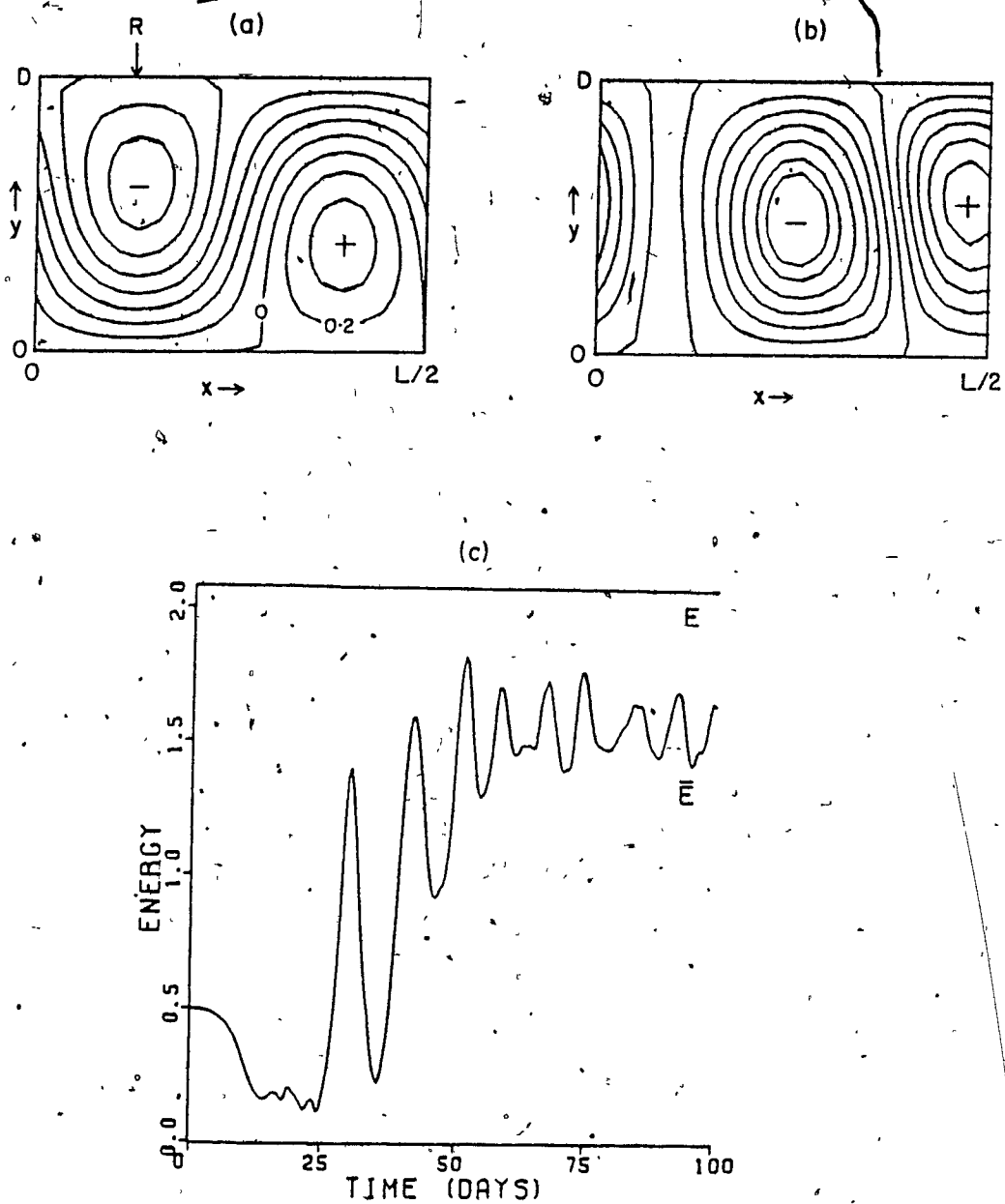


Figure 37 Experiment 2.

- (a) Steady flow streamfunction (CINT = 0.2);
- (b) FGLD structure at $t = 0$;
- (c) total, E , and mean zonal energy, \bar{E} . $\delta = \sqrt{0.02}$.

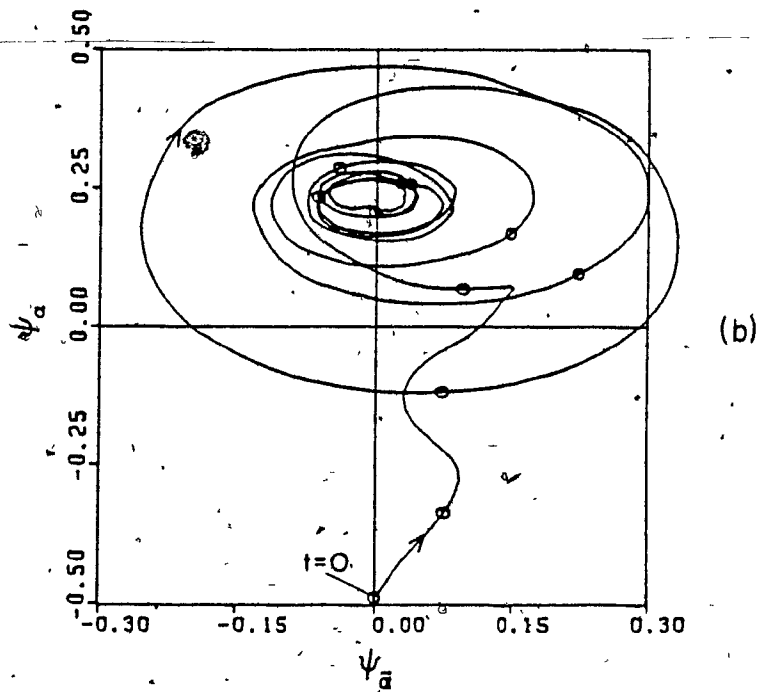
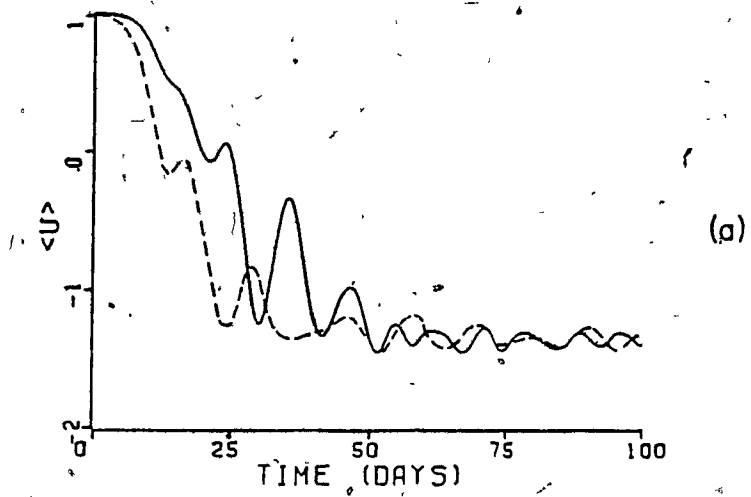


Figure 38 Experiment 2.

- (a) Channel-averaged flow, $\langle u \rangle$. $\delta = \sqrt{0.02}$. The dashed line corresponds to the $\delta = 2/\sqrt{0.02}$ simulation;
- (b) basic wave trajectory. Dots at every 10 days.

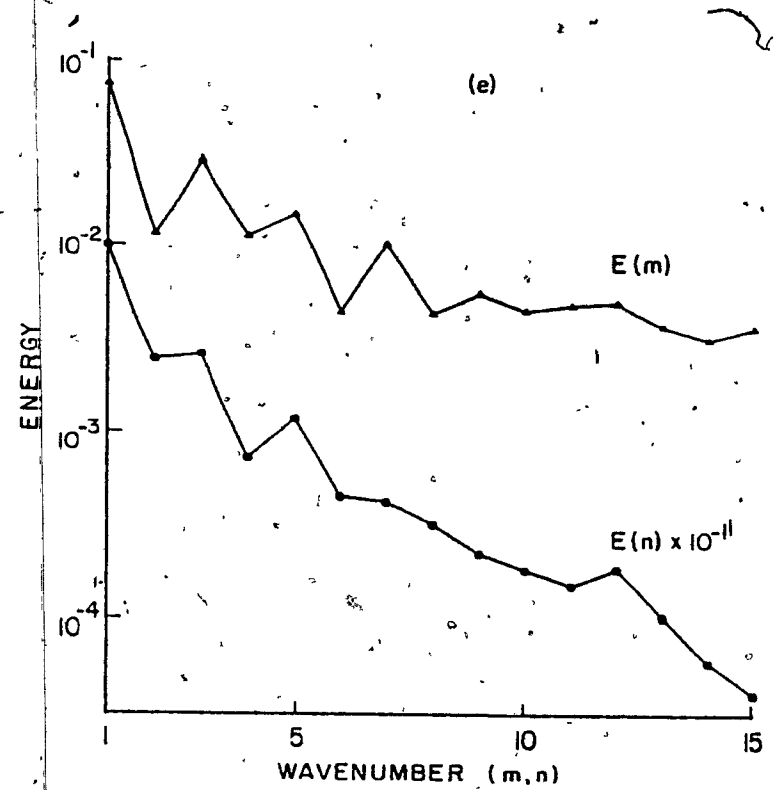
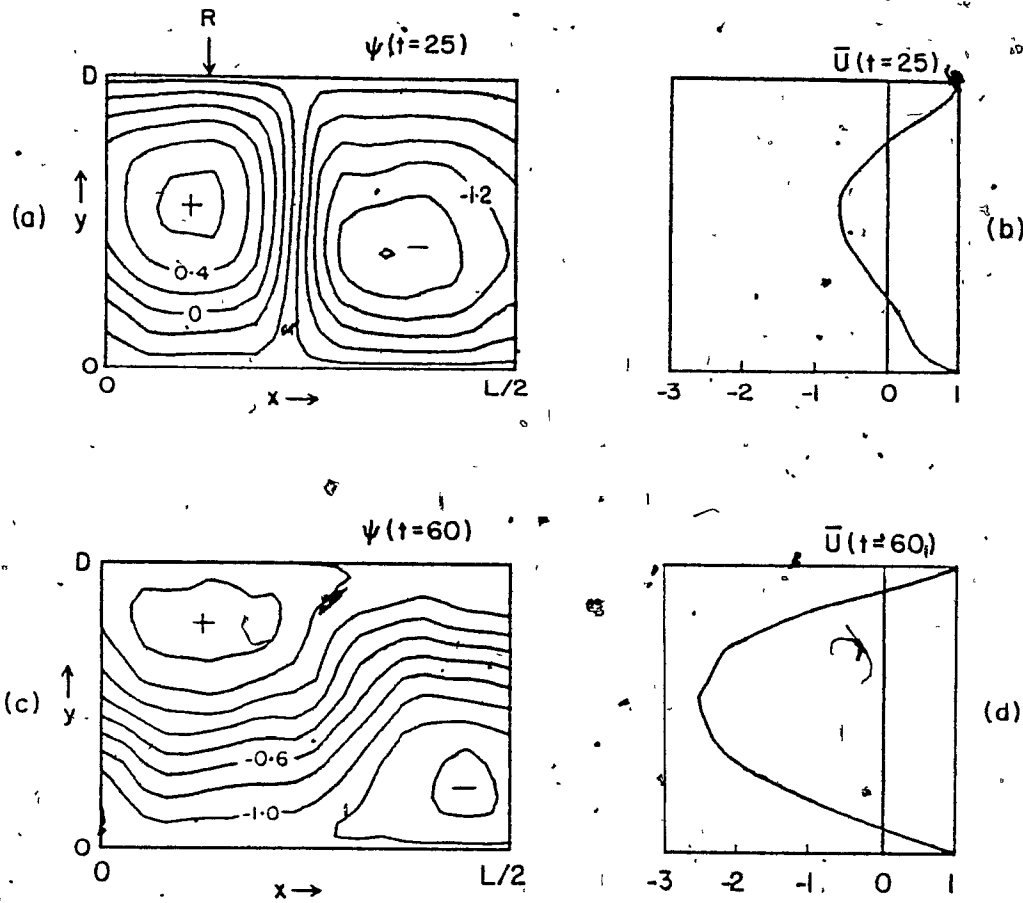


Figure 39 Experiment 2. ($\delta = \sqrt{0.02}$).

- (a) Total streamfunction, ψ , at $t = 25$ days, (CINT = 0.2);
- (b) mean zonal flow, $\bar{u}(y,t)$, at $t = 25$ days;
- (c) total streamfunction, ψ , at $t = 60$ days (CINT = 0.2);
- (d) mean zonal flow, $\bar{u}(y,t)$ at $t = 60$ days;
- (e) energy spectra at $t = 60$ days. Basic wave excluded.

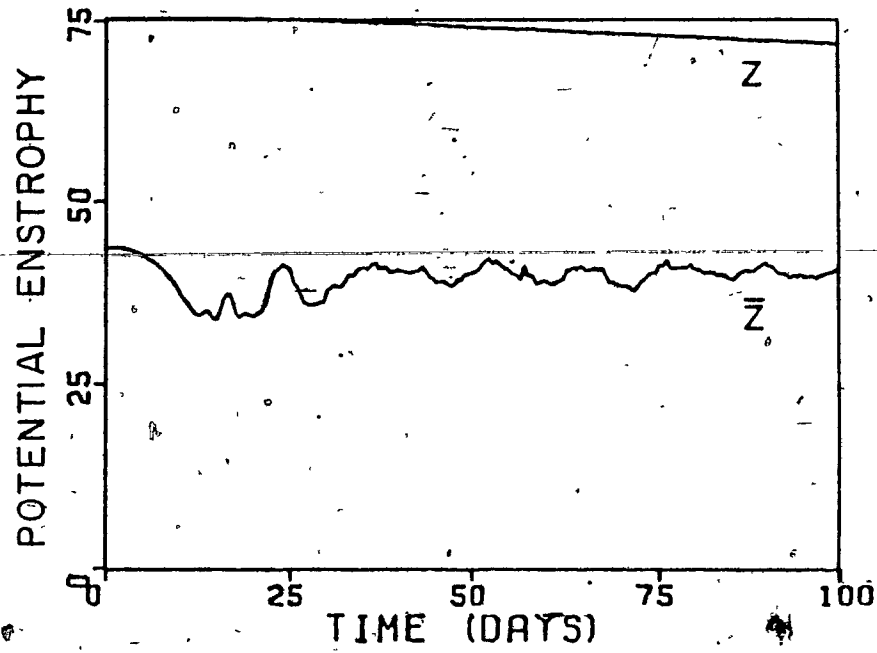


Figure 40 Experiment 2: Total, Z , and mean zonal potential enstrophy, \bar{Z} . $\delta = 2/0.02$.

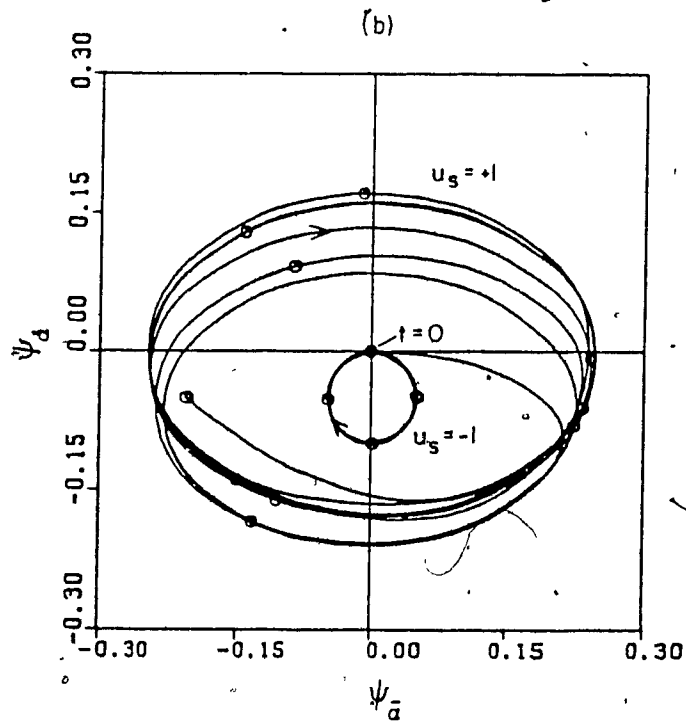
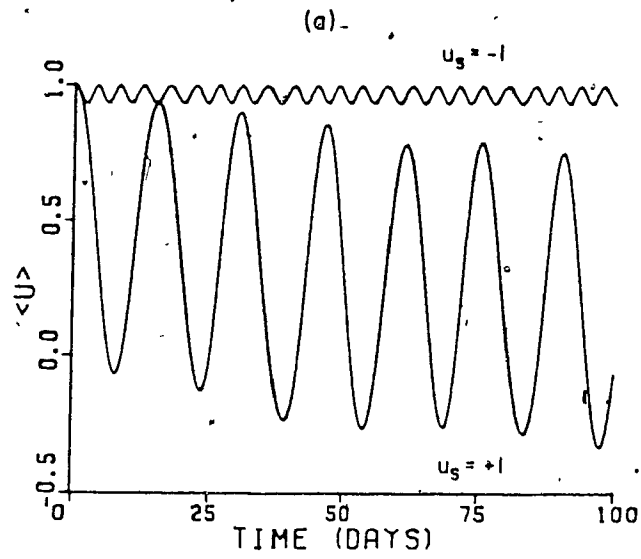


Figure 41 Behaviour of initial easterly and westerly zonal flow.

(a) $\langle u \rangle$; (b) ψ^b . $u_s = \mp 16$ m/s in dimensional units

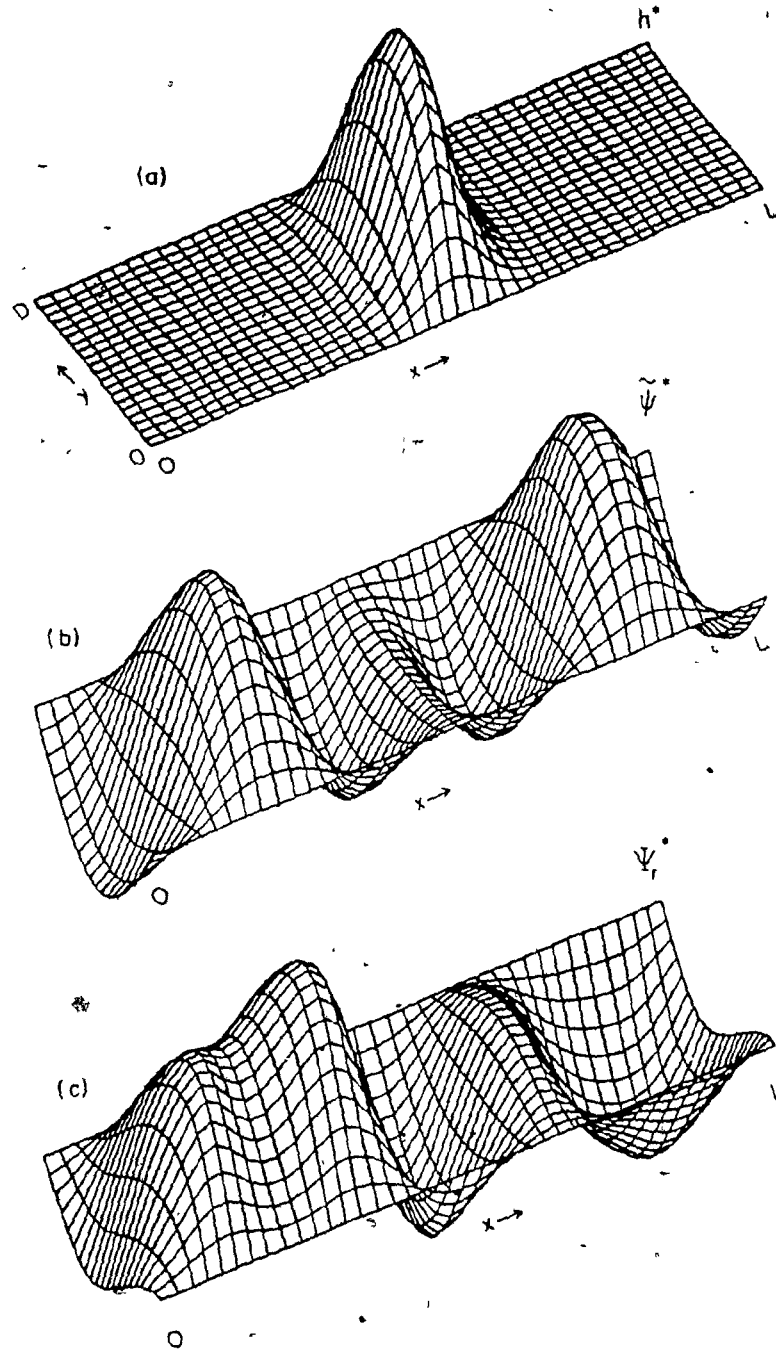


Figure 42 Experiment 3: Localized topography

- (a) Topography: $r = Dy^2$ and $h_0/H = 0.1^2$;
- (b) steady flow eddy streamfunction;
- (c) FGLD at $t = 0$ days. ()^{*} indicates that the mean zonal component has been removed.

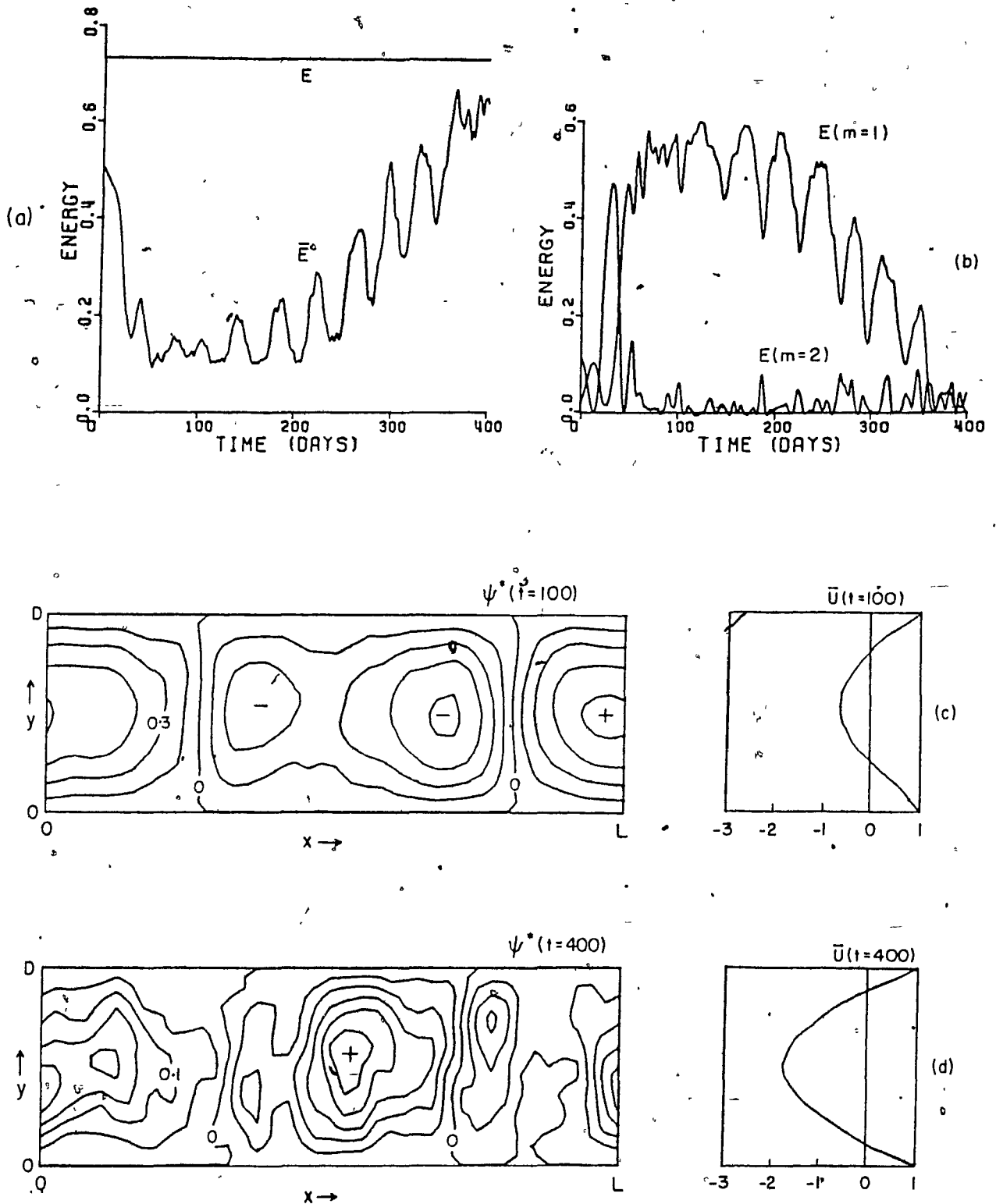


Figure 43 Experiment 3: $\delta = 2/0.02$.

- (a) Total and mean zonal energy, E and \bar{E} , respectively;
 - (b) zonal wavenumber one, $E(m=1)$, and two energy, $E(m=2)$;
 - (c) eddy streamfunction and mean zonal flow: $t = 100$ days;
 - (d) eddy streamfunction and mean zonal flow: $t = 400$ days.
- In (c), $CINT = 0.15$ and in (d), $CINT = 0.05$.

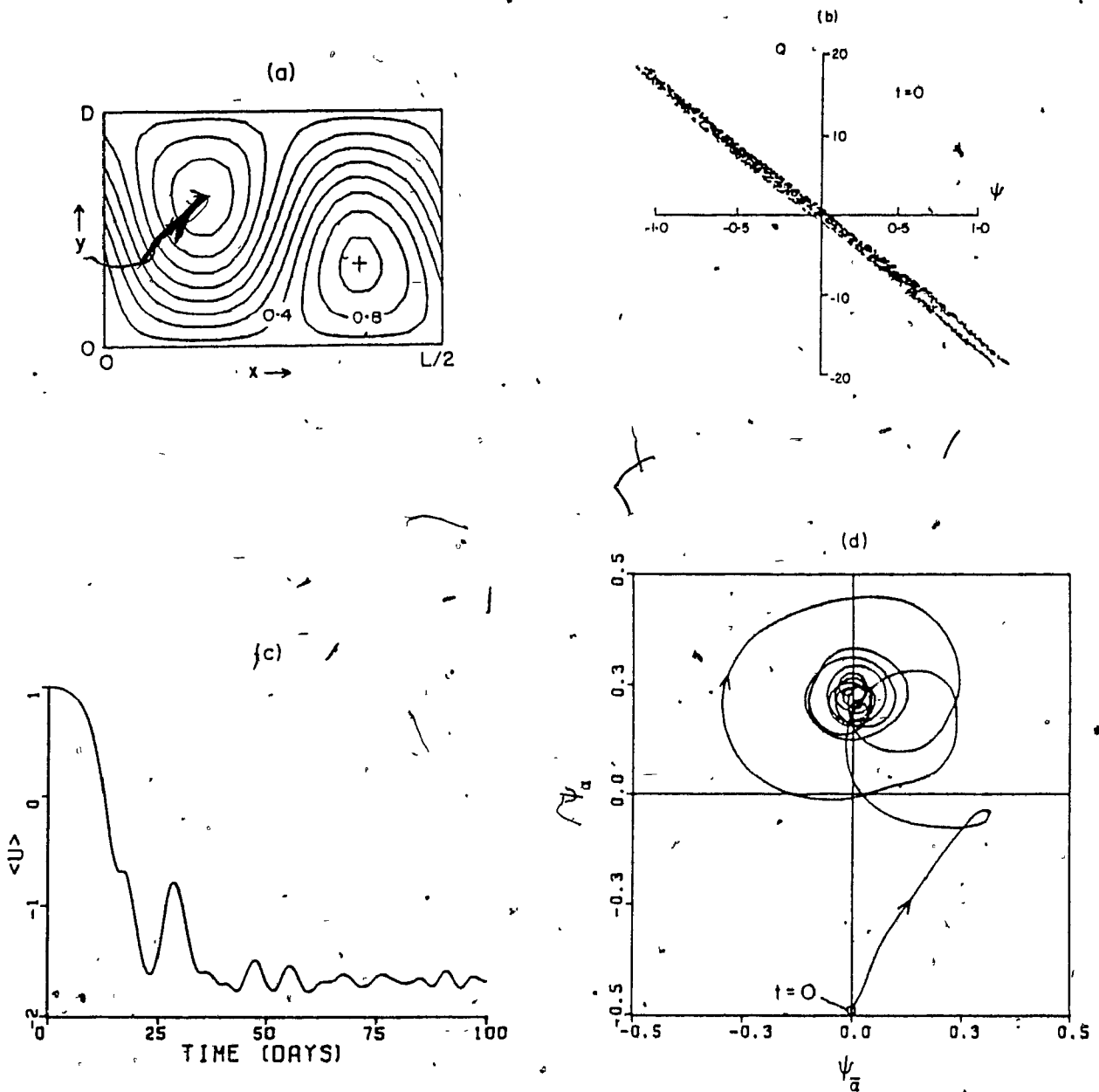


Figure 44 Experiment 4; $\delta = 2/0.02$.

- (a) Total streamfunction at $t = 0$ days (CINT = 0.2);
- (b) potential vorticity versus streamfunction at $t = 0$ days;
- (c) $\langle u \rangle$; (d) ψ^b

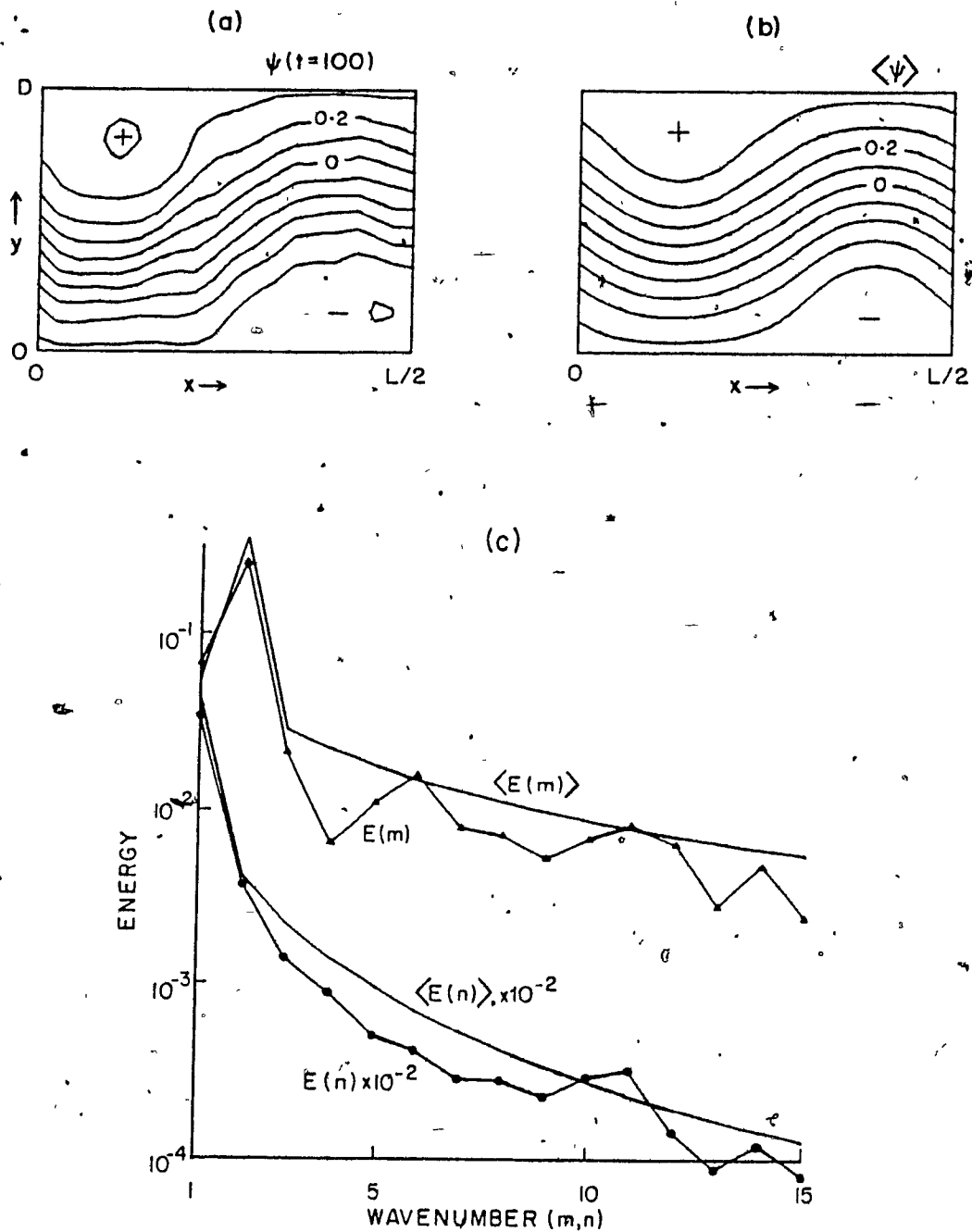


Figure 45 Simulation at $t = 100$ days versus statistical equilibrium.

- (a) Simulation streamfunction (CINT = 0.1);
- (b) equilibrium streamfunction (CINT = 0.1);
- (c) energy spectra for the simulation and the statistical equilibrium (the latter are shown as continuous curves).

| M | NL | $\hat{\omega}_i$ |
|-----|------|------------------|
| 10 | 210 | 2.33 |
| 12 | 300 | 2.13 |
| 14 | 406 | 1.56 |
| 16 | 528 | 2.15 |
| 18 | 666 | 1.06 |
| 20 | 820 | 1.60 |
| 22 | 990 | 1.51 |

Table 1 Growth rate of the topographic mode as a function of truncation: $M^2 = N$ and NL is the total number of degrees of freedom.

| M | N | NL | $\hat{\omega}_i$ | $\hat{\omega}_r$ |
|-----|-----|------|------------------|------------------|
| 10 | 10 | 210 | 3.61 | 0.0 |
| 10 | 5 | 105 | 3.61 | 0.0 |
| 5 | 5 | 55 | 3.54 | 0.0 |
| 3 | 5 | 35 | 3.44 | 0.0 |
| 10 | 3 | 63 | 2.78 | 0.97 |
| 5 | 3 | 33 | 2.78 | 0.82 |
| 3 | 3 | 21 | 2.50 | 1.10 |

Table 2 Growth rate and frequency of the fastest-growing mode corresponding to Figure 22 as a function of truncation.

| M | Experiment 1 | | Experiment 2 | |
|----|---------------|----------|---------------|----------|
| | τ (days) | T (days) | τ (days) | T (days) |
| 2 | — | — | 2.54 | 36.66 |
| 3 | 27.06 | 32.97 | — | — |
| 9 | 56.50 | 33.90 | 4.91 | 28.94 |
| 11 | 57.56 | 32.87 | 4.78 | 28.27 |
| 13 | 49.28 | 32.83 | 5.07 | 28.86 |
| 15 | 46.85 | 33.04 | 4.70 | 28.41 |
| 17 | 47.02 | 33.29 | 4.75 | 28.15 |
| 19 | 48.13 | 33.46 | 4.72 | 28.37 |

Table 3 Experiments 1 and 2: Effect of resolution on e-folding time, τ , and period, T, for the fastest-growing linear disturbance $M = N$, where M and N are the number of zonal and meridional wavenumbers, respectively.

| Δt (mins) | M | \bar{E} | E^* | E^b | $\langle u \rangle$ |
|-------------------|----|-----------|-------|-------|---------------------|
| 15 | 15 | 1.499 | 0.570 | 0.378 | - 1.336 |
| 15 | 13 | 1.490 | 0.577 | 0.398 | - 1.340 |
| 5 | 15 | 1.541 | 0.531 | 0.347 | - 1.358 |

$$\bar{E}_0 = 0.500 \quad E_0^* \approx 1.578 \quad E_0^b \approx 1.555 \quad \langle u \rangle_0 = 1.000$$

Table 4 Experiment 2: Simulation sensitivity to resolution, M, and timestep, Δt , at $t = 60$ days. $\delta = \sqrt{0.02}$

| | Simulation ($t=100$) | Statistical Equilibrium | |
|---------------------|--------------------------|--------------------------|------------------------|
| | $\delta = 2/\sqrt{0.02}$ | $\delta = 2/\sqrt{0.02}$ | $\delta = \sqrt{0.02}$ |
| $\langle u \rangle$ | - 1.685 (1.000) | - 1.655 | - 1.631 |
| \bar{E} | 1.777 (0.631) | 1.700 | 1.652 |
| E^* | 0.477 (1.631) | 0.564 | 0.555 |
| E^b | 0.273 (1.555) | 0.342 | 0.336 |
| α_0 | _____ | - 15.634 | - 15.688 |
| β_0 | _____ | 2.613 | 2.646 |

Table 5 Experiment 4: Simulation at $t = 100$ days versus statistical equilibrium. The values in parenthesis are for $t = 0$ days. Note that values for equilibrium at $\delta = \sqrt{0.02}$ are also provided.

BIBLIOGRAPHY

- Arnol'd, V. I., 1966: On an a priori estimate in the theory of hydrodynamical stability. Izv. Vyssh. Uchebn. Zaved. Matematika, 54, no. 5, 3-5 (English trans.: Amer. Math. Soc. Transl., Series 2, 79, 267-269 (1969).)
- Asselin, R., 1972: Frequency filter for time integrations Mon. Wea. Rev., 100, 487-490.
- Baines, P. G., 1976: The stability of planetary waves on a sphere. J. Fluid Mech., 73, 193-213.
- Blackmon, M. L., 1976: A climatological spectral study of the 500 mb geopotential height of the Northern Hemisphere. J. Atmos. Sci., 33, 1607-1623.
- , J. M. Wallace, N. Lau and S. L. Mullen, 1977: An observational study of the Northern Hemisphere circulation. J. Atmos. Sci., 34, 1040-1053.
- , R. A. Madden, J. M. Wallace and D. S. Gutzler, 1979: Geographical variations in the vertical structure of geopotential height fluctuations. J. Atmos. Sci., 36, 2450-2466.
- Boville, B. A., 1981: Amplitude vacillation on a β -plane. J. Atmos. Sci., 38, 609-618.
- Buzzi, A., A. Trevisan and A. Speranza, 1984: Instabilities of a baroclinic flow related to topographic forcing. J. Atmos. Sci., 41, 637-650.
- Charney, J. G. and A. Eliassen, 1949: A numerical method for predicting the perturbations of the middle latitude westerlies. Tellus, 1, 38-54.
- and J. G. DeVore, 1979: Multiple flow equilibria in the atmosphere and blocking. J. Atmos. Sci., 36, 1205-1216.
- and G. R. Flierl, 1981: Oceanic analogues of large-scale atmospheric motions. Evolution of Physical oceanography, M.I.T. Press, 504-548.
- Coaker, S. A., 1977: The stability of a Rossby wave. Geophys. Astrophys. Fluid Dyn., 9, 1-17.
- Derome, J. and A. Wiin-Nielsen, 1971: The response of a middle latitude model atmosphere to forcing by topography and stationary heat sources. Mon. Wea. Rev., 99, 964-976.
- , 1984: On quasi-geostrophic, finite amplitude disturbances forced by topography and diabatic heating. Tellus, 36, 313-319.

- and J. Fyfe, 1985: On finite-amplitude forced disturbances. Proceedings of the (Fifteenth) Stanstead Seminar, McGill University, 144 pp. [Available as rep. 128, Dept of Meteor., McGill University.]
- Deininger, R. C., 1981: Topographically forced wave instability at finite amplitude. J. Atmos. Sci., 38, 2619-2625.
- , 1982: Free Rossby wave instability at finite amplitude. J. Atmos. Sci., 39, 563-572.
- Edelmann, W., 1972: Numerical experiments with a barotropic current across mountains. Beitr. Phys. Atm., 45, 196-229.
- Egger, J. and W. Metz, 1981: On the mountain torque in barotropic planetary flow. Quart. J. R. Met. Soc., 107, 229-312.
- Fischer, G., 1980: The effect of a planetary scale mountain on a barotropic flow treated in a simple low-order system. Beitr. Phys. Atm., 53, 295-309.
- Fjortoft, R., 1953. On the changes in the spectral distribution of kinetic energy for two dimensional, nondivergent flow. Tellus, 5, 225-230.
- Frederiksen, 1979a: The effects of long planetary waves on the regions of cyclogenesis: linear theory. J. Atmos. Sci., 36, 195-204.
- , 1979b: Baroclinic instability of zonal flows and planetary waves in multi-level models on a sphere. J. Atmos. Sci., 36, 2320-2335.
- , 1980: Zonal and meridional variations of eddy fluxes induced by long planetary waves. Quart. J. Roy Meteor. Soc., 106, 63-84.
- , 1982: A unified three-dimensional instability theory of the onset of blocking and cyclogenesis. J. Atmos. Sci., 39, 969-982.
- , 1983: Disturbances and eddy fluxes in Northern Hemispheric flows: Instability of three-dimensional January and July flows. J. Atmos. Sci., 40, 836-855.
- , and G. F. Carnevale, 1986: Stability properties of exact nonzonal Arnol'd solutions for flow over topography. Geophys. Astrophys. Fluid Dyn., 35, 173-207.
- Fyfe, J. and J. Derome, 1986: A barotropic stability study of free and forced planetary waves. J. Atmos. Sci., 43, 2162-2182
- and —, 1987a: Some effects of truncation on topographic instability. Atmos. and Oceans, 25, 159-176.
- and —, 1987b: The stability of a two-dimensional steady-state flow: Local growth of perturbations. Geophys. Astrophys. Fluid Dyn. In press.

- Garbow, B. S., 1974: EISPACK - a package of matrix eigensystem routines. Computer Physics Comm., 7, 179-184.
- Gill, A. E., 1974: The stability of planetary waves on the infinite beta-plane. Geophys. Fluid Dyn., 6, 29-47.
- Grotjahn, R., 1984: Baroclinic instability in a long wave environment. Part I: Review. Quart. J. Roy. Meteor. Soc., 110, 663-668.
- Hart, J. E., 1977: A note on quasi-geostrophic flow over topography in bounded basin. J. Fluid Mech., 79, 657-668.
- , 1979: Barotropic quasi-geostrophic flow over anisotropic mountains. J. Atmos. Sci., 36, 1736-1746.
- Holopainen, E. O., 1978: On the dynamic forcing of the long-term mean flow by the large-scale Reynold's stresses in the atmosphere. J. Atmos. Sci., 35, 1596-1604.
- Holton, J. R., 1979: *An Introduction to Dynamic Meteorology*, A. L. Hales, Ed., Academic Press.
- Kasahara, A., 1966: The dynamical influence of orography on the large-scale motion of the atmosphere. J. Atmos. Sci., 23, 259-270.
- Kuo, H. L., 1973: Dynamics of quasi-geostrophic flows and instability theory. In Advances in Applied Mechanics, 13, 247-330.
- Lindzen, R. S., B. Farrell and D. Jacqmin, 1982: Vacillations due to wave interference: applications to the atmosphere and to annulus experiments. J. Atmos. Sci., 39, 14-23.
- Lau, N. H., 1978: On the three-dimensional structure of the observed transient eddy statistics of the northern hemisphere winter circulation. J. Atmos. Sci., 35, 1900-1923.
- Loesch, A. Z., 1978: Finite-amplitude stability of Rossby wave flow. J. Atmos. Sci., 35, 929-939.
- Lorenz, E. N., 1963: The mechanics of vacillation. J. Atmos. Sci., 20, 448-464.
- , 1972: Barotropic instability of Rossby wave motion. J. Atmos. Sci., 29, 258-269.
- McIntyre, M.E. and T.G. Shepherd, 1986: An exact conservation theorem for the finite-amplitude disturbances to nonparallel shear flows, with remarks on Hamiltonian structure and on Arnol'd's stability theorems. J. Fluid Mech., to appear.
- Merkine, L., 1977: Convective and absolute instability of baroclinic eddies. Geophys. Astrophys. Fluid Dyn., 9, 129-157.

- , 1982: A critical layer dominated by non-parallel effects in a rotating barotropic flow. Proc. R. Soc. Lond. A, 388, 293-310.
- Merkine, L. and R. B. Balgovind, 1983: Barotropic instability of weakly non-parallel zonal flows. Geophys. Astrophys. Fluid Dyn., 25, 157-190.
- Mied, R. P., 1978: The instabilities of finite-amplitude barotropic waves. J. Fluid. Mech., 86, 225-246.
- Mitchell, H. L., 1982: Resonance of stationary waves in a model atmosphere. Ph.D. Thesis, McGill University, 220 pp. [Available as Rep. 125, Dept. of Meteor., McGill University.]
- Mitchell, H. L. and J. Derome, 1983: Blocking-like solutions of the potential vorticity equation: their stability at equilibrium and growth at resonance J. Atmos. Sci., 40, 2522-2536.
- Mukougawa, H. and I. Hirota, 1986a: Nonlinear evolution of forced Rossby waves in a barotropic atmosphere, Part I: Stability properties of forced Rossby waves. J. Meteor. Soc. Jap., 64, 197-211.
- , 1986b: Nonlinear evolution of forced Rossby waves in a barotropic atmosphere, Part II: Initial value problems. J. Meteor. Soc. Japan, 64, 213-225.
- Nathan, T. R., A. Z. Loesch, 1987: Finite-amplitude stability of a topographically forced wave with Ekman dissipation. Tellus, 39a, 95-109.
- Niehaus, M. C., 1980: Instability of non-zonal baroclinic flows. J. Atmos. Sci., 37, 1447-1463.
- , 1981: Instability of non-zonal baroclinic flows: Multiple-scales analysis. J. Atmos. Sci., 38, 974-987.
- ^ Pedlosky, J., 1981: Resonant topographic waves in barotropic and baroclinic flows. J. Atmos. Sci., 38, 2626-2641
- Pfeffer, R. L., G. Buzyna and R. Kung, 1980a. Relationships among eddy fluxes of heat, eddy temperature variances and basic-state temperature parameters in thermally driven rotating fluid. J. Atmos. Sci., 37, 2577-2599.
- , ——, W. W. Fowles and R. Kung, 1980b: Time-dependent modes of behaviour of a thermally driven rotating fluid. J. Atmos. Sci., 37, 2129-2149.
- Pierrehumbert, R. T., 1984: Local and global baroclinic instability of zonally varying flow. J. Atmos. Sci., 41, 2141-2162.
- Plumb, R. A., 1977: The stability of small amplitude Rossby waves in a channel. J. Fluid Mech., 80, 705-720.

- Rambaldi, S., G. Salustri and C. Pellacani, 1985: Form-drag instability in a barotropic and baroclinic atmosphere. Pageoph, 123, 141-153.
- Revell, M. J. and B. J. Hoskins, 1984: Orographically induced Rossby wave instabilities. J. Atmos. Sci., 41, 51-67.
- Robert, A. J., 1963: The integration of a low order form of the primitive meteorological equations, Mon. Wea. Rev., 100, 329-335.
- Rossby, C. G., et al., 1939: Relation between variations in the intensity of the zonal circulation of the atmosphere and the displacements of the semi-permanent centers of action. J. Marine Res., 2, 38-55.
- Salmon, R. G., G. Holloway and M. C. Hendershott, 1976: The equilibrium statistical mechanics of simple quasi-geostrophic models. J. Fluid Mech., 76, 691-703.
- Sarić, W. S. and A. H. Nayfeh, 1975: Nonparallel stability of boundary-layer flows. The Physics of Fluids, 18, 945-950.
- Sawford, B. L. and J. S. Frederiksen, 1983: Mountain torque and angular momentum in barotropic planetary flows: Equilibrium solutions. Q. J. R. Meteorol. Soc., 109, 309-324.
- Simmons, A. J., J. M. Wallace and G. W. Branstator, 1983: Barotropic wave propagation and instability, and atmospheric teleconnection patterns. J. Atmos. Sci., 40, 1363-1392.
- Smagorinsky, J., 1953: The dynamical influence of large-scale heat sources and sinks on the quasi-stationary mean motions of the atmosphere. Q. J. R. Meteorol. Soc., 79, 342-366.
- Smith, R. B., 1979: The influence of mountains on the atmosphere. Advances in Geophysics, Vol. 21, Academic Press, 87-230.
- Tupaz, J. B., R. T. Williams and C.-P. Chang, 1978: A numerical study of barotropic instability in a zonally varying easterly jet. J. Atmos. Sci., 35, 1265-1280.
- Vallis, G. K., 1985: Instability and flow over topography. Geophys. Astrophys. Fluid Dyn., 34, 1-38.
- Wallace, J. M., 1983: The climatological mean stationary waves: Observational evidence. In *Large-scale dynamical processes in the atmosphere*. B. Hoskins and R. Pearce, eds. Academic Press, 27-53.
- Winston, J. S., and A. Krueger, 1961: Some aspects of a cycle of available potential energy. Mon. Wea. Rev., 89, 307-318.
- Yoden, S., 1987: A new class of stratospheric vacillations in a highly-truncated model due to wave interference. J. Atmos. Sci., 44, 1723-1733.